

Exploration of candidate fusion reactor regimes by real time control of tokamak plasma shape

THÈSE N° 7714 (2017)

PRÉSENTÉE LE 28 JUILLET 2017
À LA FACULTÉ SCIENCES DE BASE
SPC - PHYSIQUE DU TOKAMAK TCV
PROGRAMME DOCTORAL EN PHYSIQUE

ÉCOLE POLYTECHNIQUE FÉDÉRALE DE LAUSANNE

POUR L'OBTENTION DU GRADE DE DOCTEUR ÈS SCIENCES

PAR

Himank ANAND

acceptée sur proposition du jury:

Prof. V. Savona, président du jury
Dr S. Coda, directeur de thèse
Prof. . E. Schuster, rapporteur
Dr M. Lennholm, rapporteur
Dr O. Sauter, rapporteur



ÉCOLE POLYTECHNIQUE
FÉDÉRALE DE LAUSANNE

Suisse
2017

Abstract

The potential of nuclear fusion to provide a practically inexhaustible source of energy has motivated scientists to work towards developing nuclear fusion tokamak power plants. Stable operation of a tokamak at high performance requires simultaneous treatment of several plasma control problems. Moreover, the complex physics which governs the tokamak plasma evolution must be studied and understood to make correct choices in controller design. This mutual inter-dependence has informed this thesis, using control solutions as an experimental tool for physics studies, and using physics knowledge for developing new advanced control solutions.

The TCV tokamak at SPC-EPFL is ideally placed to explore issues at the interface between plasma physics and plasma control, by combining a state-of-the-art digital real time control system with a flexible and diverse set of actuators including a full set of independently powered shaping coils. The recent deployment of the real time version of the Grad-Shafranov equilibrium reconstruction code LIUQE, with a sub-ms cycle time in the digital control system, has facilitated the design of a new generalised plasma position and shape controller, based on the information on poloidal flux and magnetic field provided by the real-time Grad-Shafranov solver.

The first issue addressed in the thesis is the development and experimental testing of a new real time control strategy to construct a generalised control algorithm for not only controlling the position of the plasma but also to aid in the precise control of higher order shape moments, X-points and strike points, particularly in advanced plasma configurations such as negative-triangularity plasmas, snowflake and super-X divertors, and doublets. A controller formulation ensuring flexibility through an ordering of controlled variables from the most easily to the least easily controlled, while respecting the hardware limits on the poloidal field coil currents, is developed. The individual control parameters (proportional and integral gains) have been identified experimentally, providing good control of the plasma position without exciting instabilities, particularly the vertical instability. The successful experimental implementation of the control algorithm has been demonstrated for both fixed and time varying plasma position and shape for limiter and divertor plasma discharges. In addition, the controller has provided satisfactory performance with respect to plasma scenarios involving complex changes in the plasma shape and position. The control design exhibits an improved performance with respect to the control of the plasma position and shape in comparison to

the legacy TCV hybrid controller.

The second issue addressed in the thesis is the application of the generalised plasma position and shape controller to a snowflake plasma configuration. An experimental identification of the number of actively controlled variables and individual weights with respect to meaningful plasma quantities was performed providing reliable control of snowflake equilibria with closely spaced X-points (i.e., the ‘exact’ snowflake). A comparison of the geometrical snowflake parameters σ and θ from the real equilibrium reconstruction with the programmed references shows a finite error in σ at steady state and an oscillatory behaviour in θ . A comparison between the optimised generalised plasma position and shape controller with the performance of the TCV hybrid controller for a given reference snowflake plasma discharge showed a marked improvement in various geometrical properties of the snowflake plasma configuration, such as the σ parameter, the connection length and the flux expansion in the vicinity of the null point. However, strong control of the poloidal magnetic field at the two X-points resulted in a tradeoff on the upper part of the plasma boundary, where the overall precision was comparable to that of the legacy controller. In the experimental time available, the snowflake shots developed exhibited a boundary that was too close to the inner wall of the vessel, modifying the edge plasma behaviour (studied with infrared cameras and Langmuir probes) and making it difficult to study the physics properties of the exact snowflake. However, further optimisation should well be possible.

The generalised plasma position and shape controller, with its unique flexibility and ability to limit the controlled variables to the set that is most easily controlled, while respecting the hardware limits on the poloidal field coil currents, promises to play a crucial role in the development of advanced plasma configurations on the TCV tokamak. The property of providing simultaneous control not only of the plasma position and shape but also of the strike points, flux expansion and X-points for advanced plasma configurations is expected to be instrumental in achieving high plasma performance in future TCV campaigns.

Key words: Plasma physics, nuclear fusion, tokamak, TCV, plasma control, digital control system, plasma shape control, snowflake divertor, real time equilibrium reconstruction.

Résumé

La perspective grâce à la fusion nucléaire d'une source d'énergie pratiquement inépuisable a poussé les scientifiques à développer des centrales de fusion nucléaire appelées tokamaks. L'opération stable et à haute performance d'un tokamak nécessite la résolution simultanée de plusieurs problèmes liés au contrôle du plasma. De plus, l'évolution du plasma est gouvernée par une physique complexe qui doit être étudiée afin de faire les bons choix au moment de la conception des contrôleurs. Cette inter-dépendance a motivé cette thèse où les techniques de contrôle sont utilisées lors d'expériences pour des études de physique et où les connaissances des processus physiques est utilisée pour l'élaboration de techniques de contrôle nouvelles et avancées.

Le Tokamak à Configuration Variable (TCV) au SPC de l'EPFL est l'endroit idéal pour réaliser des études à l'interface entre physique des plasmas et contrôle du plasma puisqu'il combine un système de contrôle digital en temps réel dernier cri avec un ensemble d'actuateurs divers incluant une alimentation indépendante pour chacune des bobines poloïdales qui donnent sa forme au plasma. La mise en service récente de la version temps réel du code de reconstruction d'équilibre de Grad-Shafranov LIUQE, qui atteint un temps d'exécution sous la milliseconde dans le système de contrôle digital, a permis la conception d'un nouveau contrôleur généralisé pour la position et la forme du plasma, qui utilise le flux poloïdal et le champ magnétique fournis par le solveur de Grad-Shafranov en temps réel.

La première question traitée dans cette thèse est celle du développement et du test lors d'expériences d'une stratégie nouvelle pour la mise en place d'un algorithme de contrôle généralisé qui permette non seulement le contrôle de la position du plasma mais également un contrôle précis des moments d'ordres supérieurs de la forme du plasma, des points X et des points de contacts, en particulier pour des configurations avancées telle que des plasmas à triangularité négative, avec divergeur "snowflake" (flocon de neige) ou super-X, ainsi que des doublets. Une formulation du contrôleur est développée assurant la flexibilité grâce à un ordering des variables contrôlées selon la simplicité de leur contrôle tout en respectant les limites matérielles imposées en termes de courants dans les bobines poloïdales. Les paramètres de contrôle ont pu être déterminés expérimentalement et fournissent un bon contrôle de la position du plasma tout en évitant les instabilités telle que l'instabilité verticale. La mise en œuvre de l'algorithme de contrôle a été démontrée avec succès lors d'expériences où la position et la forme du plasma étaient fixes ou variaient au cours du temps et pour des

plasmas en configuration limitée ou divergée. De plus le contrôleur a montré des performances satisfaisantes lorsque les scénarios comportaient des changements complexes pour la forme et la position. Cette performance était supérieure au contrôleur standard utilisé dans le système de contrôle hybride de TCV.

La seconde question traitée est celle de l'application du contrôleur généralisé de la position et de la forme du plasma à une configuration avec un divergeur "snowflake". La détermination expérimentale des paramètres du contrôleur a été réalisée permettant un contrôle fiable d'équilibres snowflake où les points X sont très proches (i.e. le snowflake "exact"). Une comparaison des paramètres géométriques σ et θ , qui caractérisent les équilibres snowflake, entre l'équilibre reconstruit après l'expérience et celui programmé comme référence montre une erreur non-nulle à l'équilibre pour σ et une oscillation de θ . Une comparaison des performances respectives du contrôleur généralisé de la position et de la forme après optimisation et du contrôleur hybride de TCV, pour une même configuration de référence avec un divergeur snowflake, a montré une amélioration significative pour plusieurs paramètres typiques des configurations avec snowflake, tel que le paramètre σ , la longueur de connection et l'expansion de flux au voisinage du point nul. Cependant un contrôle renforcé du champ magnétique poloïdal aux deux points X a provoqué une dégradation du contrôle de la partie supérieure de la frontière du plasma où la précision était comparable à celle du contrôleur original. Compte tenu du temps expérimental disponible, la frontière du plasma pour les tirs snowflake obtenus était trop proche du mur intérieur de la chambre, modifiant le comportement du plasma de bord (étudié grâce aux caméras infra-rouge et aux sondes de Langmuir) et rendant plus difficile l'étude des propriétés physiques du snowflake exact. Cependant une optimisation ultérieure peut être envisagée.

Le contrôleur généralisé de la position et de la forme du plasma, avec sa flexibilité unique en son genre et sa capacité à restreindre les quantités contrôlées aux plus facilement contrôlables tout en respectant les limites matérielles en courant pour les bobines magnétiques du champ poloïdal, pourra jouer un rôle important dans le développement de scénarios utilisant des configurations plasma avancées sur TCV. Le fait de fournir un contrôle simultané non seulement de la position et de la forme du plasma mais également des points de contact, de l'expansion de flux et des points X pour les configurations plasma avancées sera une pièce maîtresse pour obtenir des décharges à haute performance lors des futures campagnes de TCV.

Mots clefs : Physique des plasmas, fusion nucléaire, tokamak, TCV, contrôle du plasma, système de contrôle digital, forme du plasma, divergeur snowflake, reconstruction de l'équilibre en temps réel.

Contents

Abstract (English/Français)	i
List of figures	vii
List of tables	xiii
1 Introduction	1
1.1 Thermonuclear fusion plasmas	1
1.1.1 The fourth state of matter	1
1.1.2 Conditions for fusion reactions and plasma confinement	2
1.2 The tokamak device	3
1.2.1 Magnetic field and coil systems	3
1.2.2 Auxiliary heating and current drive systems	4
1.3 Control problems in tokamaks	5
1.3.1 Control of bulk plasma quantities	6
1.3.2 Plasma shape and strike point control	7
1.3.3 MHD instability control	8
1.3.4 Plasma profile control	9
1.3.5 Disruption prediction and avoidance	9
1.4 Motivation for the thesis	10
1.5 Outline of this dissertation	11
2 The TCV tokamak	13
2.1 Overview	13
2.2 TCV diagnostics	17
2.2.1 Electron diagnostics	17
2.2.2 Ion diagnostics	18
2.2.3 Visible and near-visible radiation	18
2.2.4 Edge diagnostics	19
2.2.5 Magnetic diagnostics	19
2.3 Real-time control systems	20
2.3.1 The ‘Hybrid’ plasma control system	20
2.3.2 The ‘SCD’ digital plasma control system	21
2.4 Real-time equilibrium reconstruction solver	24

Contents

3	Generalised plasma position and shape controller design	27
3.1	Introduction	27
3.2	Plasma position and shape controller design.	29
3.2.1	Time invariant controller design	30
3.2.2	Time varying controller design	33
3.2.3	Anti windup and bumpless transfer	34
3.2.4	Implementation with the TCV hybrid controller	36
3.3	Plasma Modelling	38
3.4	Experimental results	42
3.4.1	Limiter plasma configuration	42
3.4.2	Divertor plasma configuration	45
3.5	Summary and conclusions	48
4	Real time control of snowflake plasma configuration	53
4.1	Introduction	53
4.1.1	Geometrical properties of snowflake plasma configuration	56
4.2	Controller optimisation of snowflake plasma configuration	59
4.2.1	Optimisation of the weight matrix	60
4.2.2	Optimisation of the actively controlled variables	63
4.3	Comparison of the controller performance with respect to the TCV hybrid controller and implications for snowflake physics	65
4.4	Summary and conclusions	70
5	Conclusions	73
5.1	Generalised plasma position and shape controller	73
5.2	Real time control of snowflake plasma configuration	74
A	RZIP and Sign-bit controller	75
A.1	RZIP	75
A.2	Sign-bit Controller	75
	Bibliography	86
	Acknowledgements	87
	Curriculum Vitae	89

List of Figures

1.1	Magnetic confinement of the charged particles by magnetic field.	2
1.2	Illustration of the tokamak concept.	4
2.1	Cutout view of TCV showing poloidal and toroidal field coils, ohmic coils, vacuum vessel and nested plasma flux surfaces with magnetic field lines.	14
2.2	Poloidal view of TCV tokamak showing the poloidal field coil system and magnetic diagnostics. Ohmic coils labeled A-D, PF coils labeled E-F. Internal field coils G (3 turn each, shown separately). Positions of magnetic field probes (rectangles) and flux loops (\times) are also shown.	15
2.3	Poloidal view of the TCV tokamak showing the PF coils and the toroidal field coil, as well as low-field-side launched X2 and top-launched X3 ECRH/ECCD systems. The steering ranges in the poloidal plane are also shown. In addition to the movement in the poloidal plane, the X2 launchers can be rotated toroidally to allow ECCD.	16
2.4	Schematic view of TCV and neutral beam injector.	16
2.5	Diagram of the original TCV control system and its connections to diagnostics and actuators.	21
2.6	Diagram of the SCD control system nodes and their respective connections to diagnostic signals and actuators.	22
3.1	Simplified block diagram representation of plasma shape and position control algorithm.	29
3.2	Schematic block diagram for the generalised plant.	31
3.3	Schematic block diagram for the generalised plasma position and shape controller. 33	
3.4	Block diagram of the controller showing the modification to avoid anti windup. 34	
3.5	Block diagram of the controller showing the bumpless transfer implementation. 34	
3.6	Block diagram showing the implementation of the generalised plasma position and shape controller with the TCV hybrid controller.	36
3.7	Isoflux surfaces generated by the poloidal field coils $E1 - E8$ and $F1 - F8$ for a limiter plasma configuration for controlling the (a) first and (b) second controlled variable. The plasma boundary is denoted by the magenta circles.	37

List of Figures

3.8	Linearised plasma modelling simulation results for the TCV tokamak. (a) Step response of the vertical estimator for the TCV hybrid controller and (b) step response of the first controlled variable and its effect on the higher order controlled variables for the generalised plasma position and shape controller. (c) Step response of the controlled variables controlling the plasma position and shape.	41
3.9	Investigation of the effect of proportional and integral gains on the performance of the generalised plasma position and shape controller. (a) Proportional gain scan without integral gain and (b) integral gain scan with a fixed proportional gain for a limiter plasma configuration with fixed plasma shape and position. (c) and (d) Time evolution of the norm of the error on the first controlled variable related to the plasma vertical position. (e) and (f) Reference and the measurement of the vertical position of the plasma magnetic axis obtained from RTLIUQE. δ and κ represents the reference of the plasma triangularity and elongation from FBTE.	43
3.10	Investigation of optimum number of actively controlled variables for plasma position and shape control for a limiter plasma configuration with a fixed set of controller gains ($K_{sp} = 0.55, \tau_{si} = 0.2s$). (a) Poloidal flux map (black lines) ψ_x and (b) last closed flux surface (blue line) obtained from RTLIUQE before and after the controller activation with an optimum number of active controlled variables (8). (c) Norm of the normalised poloidal field coil currents requested by the controller at steady state and (d) norm of the error of all the controlled variables with time as a function of the actively controlled variables. The pre-programmed control points are given by the magenta circles. δ and κ represents the reference of the plasma triangularity and elongation from FBTE.	44
3.11	Evolution of the magnitude of the singular values with respect to each controlled variable for the limiter plasma configuration.	45
3.12	Performance of the generalised plasma position and shape controller for limiter plasma configuration involving a scan of plasma vertical position and elongation with 8 actively controlled variables and fixed controller gains for position ($K_{sp} = 0.55$ and $\tau_{si} = 0.1s$) and shape control ($K_{sp} = 0.3$ and $\tau_{si} = 0.01s$). (a) Poloidal flux contour ψ_x (black lines) and (b) the last closed flux surface (green line) at different time instants of the controller operation obtained from RTLIUQE. (c) Time evolution of norm of the errors of the actively controlled variables. Reference and measurement of the plasma vertical position (d), elongation (e) and triangularity (f) obtained from FBTE and LIUQE. The pre-programmed plasma boundary is given by control points in magenta circles.	46
3.13	Last closed flux surface (red line) and vertical position Z_a of the plasma magnetic axis (blue circle) obtained from RTLIUQE for the plasma discharge 55141, at various time instances. κ and δ represent the plasma elongation and triangularity obtained from LIUQE. The pre-programmed plasma boundary is denoted by magenta circles.	47

<p>3.14 Performance of the generalised plasma position and shape controller for a limiter plasma configuration involving a scan of the plasma triangularity with 8 actively controlled variables and fixed controller gains for position ($K_{sp} = 0.55$ and $\tau_{si} = 0.1s$) and shape control ($K_{sp} = 0.3$ and $\tau_{si} = 0.01s$). (a) Poloidal flux contour ψ_x (black lines) and (b) last closed flux surface (green line) at different time instants of the controller operation, obtained from RTLIUQE. (c) Time evolution of norm of the errors of the actively controlled variables. Reference and measurement of the plasma vertical position (d), elongation (e) and triangularity (f) obtained from FBTE and LIUQE. The pre-programmed plasma boundary is given by control points in magenta circles.</p>	<p>48</p>
<p>3.15 Last closed flux surface (red line) and vertical position Z_a of the plasma magnetic axis (blue circle) obtained from RTLIUQE for the plasma discharge 55144, at various time instances. κ and δ represent the plasma elongation and triangularity obtained from LIUQE. The pre-programmed plasma boundary is denoted by magenta circles.</p>	<p>49</p>
<p>3.16 Performance of the generalised plasma position and shape controller for controlling a time invariant divertor plasma configuration with optimised actively controlled variables (8) and controller gains for position ($K_{sp} = 0.55$ and $\tau_{si} = 0.1s$) and shape control ($K_{sp} = 0.85$ and $\tau_{si} = 0.05s$). (a) Poloidal flux contour ψ_x (black lines) and (b) last closed flux surface (green line) at different time instants of the controller operation, obtained from RTLIUQE. (c) Time evolution of norm of the errors of the actively controlled variables. Reference and measurement of the plasma vertical position (d), elongation (e) and triangularity (f) obtained from FBTE and LIUQE. The pre-programmed plasma boundary is given by control points in magenta circles.</p>	<p>50</p>
<p>3.17 Performance of the generalised plasma position and shape controller for controlling time varying divertor plasma configuration with optimised actively controlled variables (8) and controller gains for position ($K_{sp} = 0.55$ and $\tau_{si} = 0.1s$) and shape control ($K_{sp} = 0.3$ and $\tau_{si} = 0.01s$). (a) Poloidal flux contour ψ_x (black lines) and (b) last closed flux surface (green line) at different time instants of the controller operation, obtained from RTLIUQE. (c) Time evolution of norm of the errors of the actively controlled variables. Reference and measurement of the plasma vertical position (d), elongation (e) and triangularity (f) obtained from FBTE and LIUQE. The pre-programmed plasma boundary is given by control points in magenta circles.</p>	<p>51</p>
<p>3.18 Separatrix (red line) and vertical position Z_a of the plasma magnetic axis (blue circle) obtained from RTLIUQE for the plasma discharge 55725, at various time instances. κ and δ represent the plasma elongation and triangularity obtained from LIUQE. The pre-programmed plasma boundary is denoted by magenta circles.</p>	<p>52</p>

List of Figures

4.1	Schematic representations of a (a) conventional single-null and (b) a snowflake divertor.	54
4.2	Schematic of different SF configurations: (a) An exact SF, (b) a snowflake plus and (c) a snowflake minus configuration. The blue and red crosses represent the primary and secondary X-points, respectively, and the black circles represent the plasma magnetic axis and representative divertor coils.	55
4.3	Representation of the θ parameter for a snowflake plasma configuration.	56
4.4	Schematic drawing showing the distance $d\rho$ between two flux surfaces along the SOL.	57
4.5	Schematic showing the (a) trajectory along the magnetic field lines and (b) its projection into the poloidal plane.	58
4.6	References for (a) σ and (b) θ for a snowflake plasma configuration obtained from FBTE. The pre-programmed plasma boundary (magenta circles) and the location of the strike points (magenta diamonds) and the X-points (magenta crosses) in MGAMS. (c) Poloidal flux map (blue curves) and separatrix (red curves) and location of the magnetic axis (black cross) obtained from the free boundary equilibrium code (FBTE) at a given time instance.	59
4.7	Comparison of controller performance on a SF plasma configuration with (55740) and without (55823) preferential weighting for controlling the poloidal magnetic field at the X-points for an equal number of actively controller variables (8). (a) Time evolution of the norm of the errors on the actively controlled variables; error on the (b) first and the (c) second controlled variable related to the control of the plasma position; time dependence of the norm of the errors on variables closely related to, respectively (based on an inspection of the respective field maps), (d) plasma shape, (e) divertor leg estimator, (f) radial and (g) vertical magnetic field at the two X-points. The controller activation time is denoted by the red line.	61
4.8	Comparison of geometrical parameters, poloidal flux map contours (thin blue lines) and separatrix (thick blue line) for SF plasma discharges obtained from RTLIUQE (a) with (55740) and (b) without (55823) preferential weighting for controlling the poloidal magnetic field at the X-points at $T = 1.29$ s. The pre-programmed plasma boundary (magenta circles), the positions of the strike points (magenta diamonds) and the positions of the X-point (magenta crosses) are given by MGAMS.	62

4.9	Comparison of controller performance on a SF plasma configuration with 8 (55740) and 4 (55843) actively controlled variables with a fixed weighting for controlling the poloidal magnetic field at the X-points. (a) Time evolution of the norm of the errors on the actively controlled variables; error on the (b) first and the (c) second controlled variable related to the control of the plasma position; time dependence of the norm of the errors on variables closely related to, respectively (based on an inspection of the respective field maps), (d) plasma shape, (e) divertor leg estimator, (f) radial and (g) vertical magnetic field at the two X-points. The controller activation time is denoted by the red line.	63
4.10	Evolution of the magnitude of the singular values with respect to each controlled variable for the snowflake plasma configuration.	64
4.11	Controller performance on a SF plasma configuration with 8 actively controlled variables and fixed preferential weighting for controlling the poloidal magnetic field at the X-points. (a) Time evolution of the norm of the actively controlled variable errors. (b) σ and (c) θ parameters obtained from FBTE and RTLIUQE. (d) Comparison between the separatrix obtained from FBTE and RTLIUQE at $T = 1.29$ s. The pre-programmed plasma boundary (magenta circles), the locations of the two X-points (magenta crosses) and the positions of the strike points (magenta diamonds) are given by MGAMS.	65
4.12	Comparison of the performance of the TCV hybrid controller and the optimised generalised plasma position and shape controller on a SF plasma configuration. Time evolution of the geometrical parameters (a) σ and (b) θ ; (c) connection length $L_{ }$ as a function of the upstream distance of the flux surface from the LCFS at given time $T = 1.29$ s. (d) Difference between the separatrix obtained for the two plasma discharges from RTLIUQE at $T = 1.29$ s. On the right-hand side are shown the pre-programmed plasma boundary (magenta circles) and the locations of the two X-points (magenta crosses) and of the strike points (magenta diamonds) given by MGAMS.	66
4.13	Difference between the separatrix obtained from RTLIUQE for the two plasma discharges at various time instances during the discharge. The red separatrix denotes discharge 55740, while the black one represents 55463. The pre-programmed plasma boundary, strike points and X-points are denoted by magenta circles, magenta diamonds and magenta crosses, respectively.	67
4.14	Comparison of SF physics parameters between discharges controlled by the TCV hybrid controller and the optimised generalised plasma position and shape controller, respectively. (a) $B_{\theta, npt}$, poloidal field and (b) $f_{x, npt}$, flux expansion, in the vicinity of the null point, and (c) variation of ρ_{npt} , minimum distance of the field line to the X-point, as functions of upstream distance of the flux surface from the LCFS.	68

List of Figures

4.15 Comparison of diagnostic data in SF configurations controlled with the TCV hybrid controller and the optimised generalised plasma position and shape controller, respectively. (a) Reference and measurement of the σ parameter obtained from FBTE and RTLIUQE for the plasma discharges. (b) Time evolution of the total deposited power and (c) peak value of heat flux deposited on SP1 and SP2, obtained from the infrared diagnostic. Time dependence of the peak value of the ion flux at the SP1 and SP2 (d), SP4 (e) and SP3 (f). 69

4.16 Comparison of SF discharges controlled by the TCV hybrid controller and the advanced shape controller, respectively, at fixed time T=1.29 s, with respect to heat flux profile on SP1 and SP2 obtained from the infrared camera, and ion flux profile on (b) SP1 and SP2, (c) SP3 and (d) SP4 obtained from the Langmuir probes. The plasma shapes are shown in (d). 70

4.17 Equilibrium reconstructions and images from the tangential visible CCD camera for the plasma discharges 55740 and 55463 at various time instances. 71

List of Tables

2.1 TCV tokamak parameters	17
--------------------------------------	----

1 Introduction

Nuclear fusion is the most basic energy production mechanism in the universe. This fundamental process holds the key for meeting the growing needs of humanity. A safe, non-polluting and abundant source of energy would propel mankind beyond the fossil-fuelled spark of the industrial revolution and provide perspective for human development thousands or millions of years into the future.

Initially, accomplishing controlled nuclear fusion was believed to be within the grasp. However, the early estimates were overly propitious, and with the subsequent discovery of new instabilities and transport mechanisms limiting the fusion performance of experimental devices, a definitive solution has not been found to this date. Arguably, the most promising approach today is represented by the tokamak, a magnetic confinement configuration which so far retains the world record in fusion power production.

1.1 Thermonuclear fusion plasmas

1.1.1 The fourth state of matter

Plasmas are known as the fourth state of matter. In the other three states, solid, liquid, and gaseous, each atom is electrically neutral, with a positively charged nucleus surrounded by negatively charged electrons. The first requirement for nuclear fusion reactions to occur is that the nuclei must be free to encounter other nuclei, thus they must be stripped of their electrons. This occurs naturally when a 'gas' temperature is raised beyond the limit where ionisation takes place: atomic collisions can then cause electrons to become detached from the nuclei, and these free electrons then cause an avalanche, ionizing the majority of atoms. This transition generally occurs within a small temperature range (around 10,000 K for many gases), and can therefore be approximately described as a phase transition into the plasma state. In this state, ions come sufficiently close to each other that they tunnel through the Coulomb potential barrier into the region where the strong nuclear force dominates, and two ions fuse. The probability that fusion reactions occur depends on the ion temperature and is

Chapter 1. Introduction

only significant in excess of 1 keV, or approximately 10 million degrees Kelvin. Moreover, it is also necessary to confine the plasma for a long enough time that more energy is released through fusion reactions than is used for heating. Due to the charged nature of the particles in the plasma, they are influenced by the external electromagnetic fields. The dynamics of the charged particles is governed by the Lorentz force, $\mathbf{F} = q(\mathbf{E} + \mathbf{v} \times \mathbf{B})$ where q is the particle's charge, \mathbf{v} is the particle's velocity and \mathbf{E} , \mathbf{B} are the electric and magnetic fields, respectively. As a result of the Lorentz force, charged particles tend to follow orbits around magnetic field lines, as illustrated in Figure 1.1.

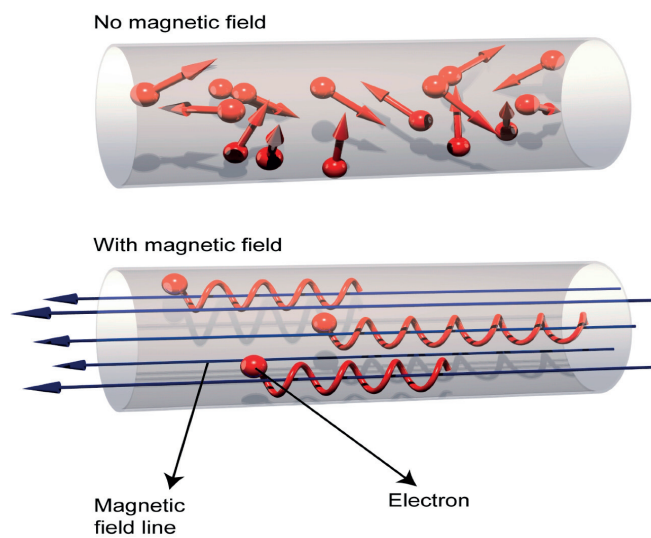


Figure 1.1 – Magnetic confinement of the charged particles by magnetic field.

1.1.2 Conditions for fusion reactions and plasma confinement

The aim of a fusion reactor device is net energy production; in other words a useful reactor must produce more power from the reaction than the power required for heating the plasma and operating the machine. A plasma must simultaneously be sufficiently dense and at the optimum temperature where the fusion probability, or cross-section, between the fusion reactants is maximal. The reaction between Deuterium (${}^2_1\text{D}$) and Tritium (${}^3_1\text{T}$), two isotopes of Hydrogen with one proton and 1 and 2 neutrons, respectively, has the largest cross-section:



For net positive energy generation, a large fusion reaction rate alone is not a sufficient condition: the energy must be confined for a sufficiently long time that the power required to maintain the plasma at the required temperature remains less than the fusion power. This

is expressed by the energy confinement time (τ_E) defined as the ratio between plasma total energy and power losses. The ignition condition is the extreme limit, where no input power is needed because a recycled fraction of the fusion power is sufficient to maintain the plasma in the burning regime; this is defined by the Lawson criterion:

$$nT\tau_E \geq 3 \times 10^{21} \text{ m}^{-3}\text{keVs}. \quad (1.2)$$

where n is the density and T is the temperature of the plasma. For D-T fusion reactions, $T = 25 \text{ keV}$ reciprocates to a minimum required $n\tau_E > 1.7 \times 10^{20} \text{ m}^{-3}\text{s}$. Therefore, efforts have focused on obtaining a value as high as possible for this product.

Two alternative approaches have been developed in mainstream fusion research. The first seeks an extremely large density (of the order of 10^{31} m^{-3}) with a very short energy confinement time (between 10 and 100 ps), and is referred to as inertial confinement. The other aims for smaller densities (of the order of 10^{20} m^{-3} , much lower than air density) and longer energy confinement time (of the order of 1 s) and is called magnetic confinement.

1.2 The tokamak device

1.2.1 Magnetic field and coil systems

The tokamak concept invented in the Soviet Union in the late 1950s is now the major and most promising magnetic confinement approach being pursued around the world. Tokamak is an acronym developed from the Russian words TOroidalnaya KAmera ee MAgnitaya Katushka which means “toroidal chamber with magnetic coils”. As the name suggests, it is a magnetic confinement device with toroidal geometry. Figure 1.2 shows the schematic of the magnetic field and the current configuration in the tokamak. The main magnetic field in a tokamak is produced in the toroidal direction (around the torus) and is generated by a set of toroidal field coils (placed in the poloidal plane, i.e. plane perpendicular to the toroidal direction). A toroidal field in itself is insufficient to confine the plasma, as it leads to drifts caused by the magnetic field gradients and curvature in opposite directions for the oppositely charged species, leading to charge separation and ultimately loss of the plasma. An additional poloidal magnetic field, typically 10 times weaker than the toroidal one, must be generated by a toroidal current flowing inside the plasma itself. The combined field generates twisted magnetic field lines around the tokamak to form a helical structure. In addition to the poloidal magnetic field generated by the plasma, an additional component of poloidal magnetic field is generated by the poloidal magnetic field coils. The resultant of the poloidal magnetic field is used to control the plasma vertical and horizontal position in the poloidal plane, as well as to define the shape of the plasma.

The plasma current is driven inductively using the Ohmic coil (also referred to as the primary transformer coil, or Central Solenoid (CS), Figure 1.2). The plasma acts as the secondary circuit of a transformer and the Ohmic coil as primary, and the plasma current is directly

proportional to the Ohmic coil current ramp rate. However, the Ohmic coil current cannot be ramped indefinitely, hence the time during which plasma current can be inductively sustained is limited by the flux swing, i.e., the integral of inductive voltage over time provided by the Ohmic coil. To achieve or approach steady state operation, the plasma current must be driven by non-inductive alternatives. Bootstrap current generated by the plasma current itself provides a part of the non inductive current and the rest is supplied by the auxiliary current drive injection system.

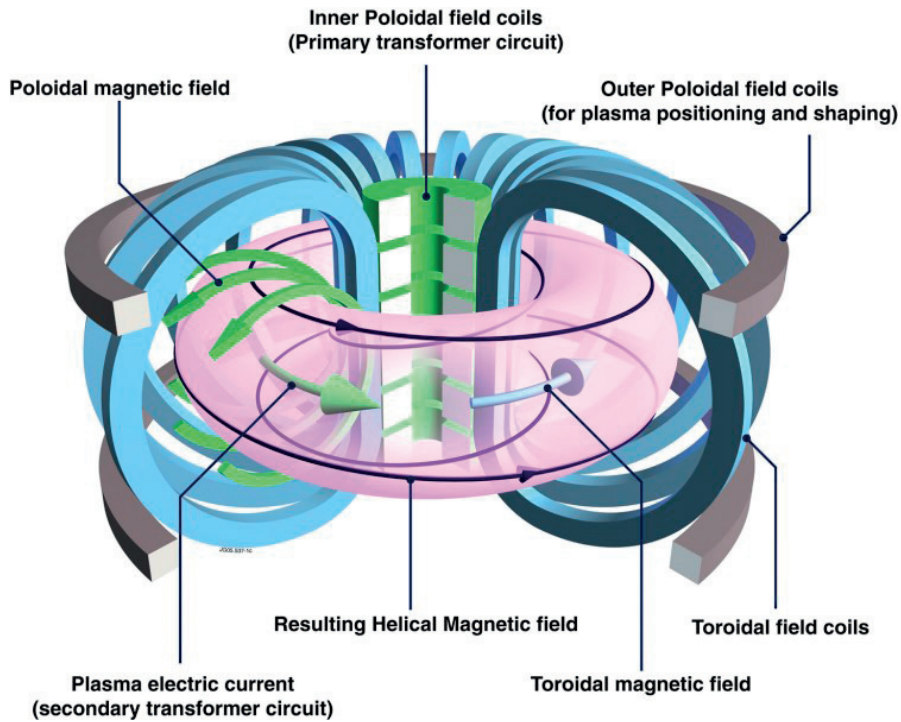


Figure 1.2 – Illustration of the tokamak concept.

1.2.2 Auxiliary heating and current drive systems

The resistivity of the plasma scales as $\eta \approx T_e^{-3/2}$, where T_e is the electron temperature. This implies that plasmas become less resistive as their temperature is increased, and as a result for temperatures above ≈ 1 keV Ohmic power becomes highly ineffective. Auxiliary heating systems have therefore been developed to heat plasmas beyond this limit, as well as to inject additional current.

- Neutral Beam Injectors (NBI) inject neutral atoms into the plasma, which are unaffected by the magnetic field, until they are ionized due to collisions with plasma particles, whereby they impart their kinetic energy to the plasma. One of their main disadvantages is the size and complexity of the injectors, as well as the difficulty to control the location in which the heat and current are deposited. NBIs also inject angular momentum, causing the plasma to rotate macroscopically which can have important physical

consequences.

- Ion Cyclotron Heating and Current Drive (ICRH/ICCD) utilises a high-intensity beam of electromagnetic radiation with a frequency of 20 to 80MHz. A generator, transmission lines and an antenna are necessary for ion cyclotron heating. A generator produces high-power radio frequency waves that are carried along a transmission line to an antenna located in the vacuum vessel, sending the waves into the plasma.
- Lower Hybrid heating and Current Drive (LHCD) is a method of plasma heating, relying on resonant coupling to a wave in the plasma. The wave is in the microwave range and imparts toroidal momentum directly to the electrons, driving the plasma current.
- Electron Cyclotron Heating and Current Drive (ECRH/ECCD) utilises RF waves of frequencies in the 100GHz range that resonate with the electron cyclotron motion around the field lines, heating the electrons and driving bulk current. Furthermore, due to its short wavelength, steering/focusing mirrors can be used to precisely direct the location of absorption and driven current in the desired location inside the plasma. This allows great operational flexibility, which has motivated the installation of ECRH systems on many tokamaks around the world.

1.3 Control problems in tokamaks

Experimental fusion technology has reached a point where experimental devices are able to produce about as much energy as is spent in heating the plasma. The immediate next step in this roadmap is the construction and operation of the International Thermonuclear Experimental Reactor (ITER). The ITER tokamak, an international 10 billion euros project that includes the European Union(+ Switzerland), the People's Republic of China, the Republic of Korea, the Russian Federation, Japan, India and the United States, will demonstrate the physics understanding and several key technologies necessary to maintain burning plasmas.

The planned ITER device will be capable of exploring advanced tokamak (AT) modes of operation, among others, characterised by high plasma pressure, long confinement times, and low levels of inductively driven plasma current, which allows long-pulse operation. These advanced modes rely heavily on active control strategies to develop and maintain high performance plasmas with sufficient density, temperature, and confinement to sustain a self-sustaining fusion reaction for long durations. Tokamaks are high order, distributed parameter, nonlinear systems with a large number of instabilities, so there are many extremely challenging mathematical modelling and control problems that need to be solved; this is especially true for a fusion power reactor. Virtually all existing tokamaks feature active control over the plasma position, current and, density (Ariola and Pironti, 2008). They define macroscopic characteristics of the plasma, each of which must lie within given ranges in order for the plasma to exist at all. The tokamak control problems can be separated into two major classes:

- Electromagnetic control refers to controlling the magnetic and electric fields, which

maintain or change the plasma position, shape and current.

- Plasma kinetic control refers to controlling particle feed rates and heating to modify the plasma density, temperature, pressure, and current density.

1.3.1 Control of bulk plasma quantities

Vertical control poses the most stringent requirements on the coil characteristics in terms of dynamic response and maximum current. Additionally, the vertical position is unstable for plasmas that are vertically elongated, and without active feedback control (Lazarus et al., 1990b) an elongated plasma would be lost vertically. In general, radial and vertical position control is achieved by a linear combination of poloidal field coils generating a magnetic field which creates a net force on the plasma in the required direction to maintain the plasma at a given reference location. The plasma current is proportional to the Ohmic coil ramp rate which governs the inductive voltage. It is controlled by a feedback loop which adjusts the Ohmic current ramp rate based on the error between the measured plasma current and its reference value. The plasma density is controlled by adjusting the aperture of gas valves or the timing of pellet injection system. All the above control problems are considered solved and constitute a basic requirement for tokamak operation. They are typically implemented as PID (Proportional, Integral, Derivative) controllers where the actuator command is a linear combination of the error signal, its integral and its derivative.

A circuit model is used in (Jardin and Larrabee, 1982) to analyse a feedback system consisting of a single passive coil and an active feedback coil. It is proved that proportional feedback of the plasma vertical position can stabilize the system, provided that the shielding effect of the passive coil, measured by the mutual inductance, is sufficiently small. However, this result is not quantitatively extendable to a massive structure of passive conductors.

The circuit model has also been used to design sophisticated controllers for plasma vertical stabilization. In (Moriyama et al., 1985) a modified linear-quadratic (LQ) approach, which accounts for the time delay of the power supply, enlarges the stability region with respect to the standard PD controllers. In (Al-Husari et al., 1991) an H_∞ approach is used to design a vertical controller with low sensitivity to changes in the operating point. A low-order controller is also designed in (Al-Husari et al., 1991) using a reduced-order plant model obtained from balanced truncation. In (Gossner et al., 1999), a predictive control algorithm is implemented on the COMPASS-D tokamak. This algorithm stabilizes the plasma using only flux sensors external to the vacuum vessel, as opposed to a standard PD controller, which uses mode estimates based at least partially on magnetic field sensors internal to the vacuum system. In (Lennholm et al., 1998) a derivative controller is used to stabilize the plasma vertical velocity. The derivative gain is adaptively changed with the growth time of the unstable mode: the variations of the growth time are detected by measuring the frequency of the plasma vertical oscillations around the equilibrium.

In (Albanese et al., 1989) a linearised, non-rigid model of the plasma vertical displacements is presented. The resulting numerical model, which is more accurate than the filament models, can be used for open-loop analysis and for designing stabilizing controllers. Furthermore, this model addresses the problem of optimal sensor location for designing active stabilization systems for highly elongated plasmas (Ward and Hofmann, 1994). A modification of the linearisation procedure illustrated in (Ward and Hofmann, 1994) is proposed in (Humphreys and Hutchinson, 1993) to include the effect of the vessel on plasma stability. This model is obtained by approximating the plasma response to currents in the vacuum vessel in terms of equivalent poloidal field coil currents. The linearised perturbed equilibrium plasma response model is used for designing a vertical stabilization controller based on full-state-feedback pole placement combined with an observer that uses flux and field measurements and their calculated time derivatives.

To simplify plasma motion control, early tokamaks used sets of poloidal field coils symmetrically placed with respect to the tokamak equatorial plane to guarantee mutually independent vertical and horizontal movement of the plasma. The problem is then separated into two orthogonal parts:

- horizontal position and current control by means of up–down symmetric currents;
- vertical position control by means of up–down anti-symmetric currents.

Initially, research efforts concentrated on the radial position control of circular, vertically stable tokamak plasmas.

Coupling between the plasma radial position and current control systems depends on the active poloidal coil system. In traditional tokamak designs, a decoupled system of poloidal windings is used. This system consists of an ohmic heating (OH) winding, the central solenoid, that controls the ohmic magnetic flux and thus the plasma current, as well as a vertical field (VF) circuit that controls the plasma major radius. For these tokamaks, the simplest controller structure consists of two separate SISO controllers. For more complex systems, or when high performance is required, MIMO decoupling controllers are needed. An LQ optimal controller for plasma radial position and current in the Tokamak Fusion Test Reactor of the Princeton Plasma Physics Laboratory during the flat-top phase is proposed. This controller computes the voltages of the OH and vertical field coils as a linear combination of eight measurements, namely, plasma radius and current, active coil currents, and their derivatives. In (Firestone, 1982) this approach is extended to include the start-up phase in which the plasma shape expands and the plasma current increases so that the resulting model is time varying.

1.3.2 Plasma shape and strike point control

Although the plasma facing components are designed to withstand high heat fluxes, contact with the plasma is always a major concern in tokamak operation and, therefore, adequate

plasma-wall clearance must be guaranteed. Thus, besides the mandatory feedback control of the bulk quantities, it is also desirable to control the position of the Last Closed Flux Surface (LCFS), i.e. the location of the plasma boundary in the poloidal plane. Moreover, controlling the shape also provides efficient coupling with auxiliary heating system antennas close to the plasma (ICRF/LH). The shape of the plasma also has an effect on the confinement of energy and particles and can be optimised to achieve better performance (Moret et al., 1997). Finally, to avoid power deposition in locations where they can do damage, the strike points in diverted plasmas should be controlled to be at the correct location with respect to the divertor target plates.

In the next-generation tokamak, the plasma-wall distance must be carefully controlled during the main part of the experiment with an accuracy of a few centimetres. When high performance is required, the strong output coupling calls for a model-based MIMO approach to obtain adequate closed-loop performance. There are few examples of multivariable controllers used for shape control. In (Walker et al., 1999) normalized coprime factorization is used to control the shape of the DIII-D plasma. In (Ambrosino et al., 1998; Ariola et al., 1999) the authors propose a controller designed using the H_∞ technique, which has been used during normal tokamak operation to control simultaneously the plasma current, vertical position and some geometrical parameters.

In (Ariola and Pironti, 2005) the authors describe the features of the new controller proposed for the JET tokamak, which has been called eXtreme Shape Controller (XSC). This new controller is the first example of a multivariable tokamak controller that allows one to control with high accuracy the overall plasma boundary, specified in terms of a certain number of gaps. The XSC, which has recently been implemented at JET, is able to operate with extremely shaped plasmas, i.e., plasmas with high elongation.

Strike point sweeping is the movement of the plasma strike points, in the lower region of the vessel, at a prescribed frequency, with the aim of avoiding excessive heat in that region. During sweeping, the plasma boundary should ideally be maintained fixed and therefore the movement should occur only in the strike point region. In (Ambrosino et al., 2008) the control schemes that have been proposed for the JET tokamak to perform sweeping are described and some experimental results are presented.

1.3.3 MHD instability control

In order to optimise the plasma performance, MHD modes described by the Magneto-hydrodynamic equations (Goedbloed and Poedts, 2004), (Freidberg, 1987) have to be controlled. The MHD modes relevant in tokamaks are as follows:

- Resistive wall Modes (RWM) appear as a helical deformation in high- β plasmas, peaked near the edge, due to resistive MHD and wall effects, and limit the maximum achievable pressure in high - β_N plasmas. Active non-axisymmetric coils close to the LCFS have

been used to control the RWM (Chu and Okabayashi, 2010).

- Edge localised modes (ELMs) are an exclusive feature of H-mode plasmas wherein the edge pressure gradients suddenly collapse causing a loss of part of the plasma energy and its deposition on the plasma facing components. Progress has been obtained in accessing ELM-free H-mode regimes, where the ELMs are entirely suppressed and replaced by more continuous channels for energy flow through the LCFS (Evans et al., 2005), (Suttrop et al., 2011).
- Neoclassical tearing modes (NTMs) cause the nested flux surfaces to reconnect and form regions of magnetic islands. They may also cause a global plasma disruption in which the entire plasma current drops to zero in a short time, resulting in high thermal and mechanical stresses on machine components. NTMs can be reduced in size and even completely suppressed by sufficient amounts of localised ECCD (Sauter et al., 1997).
- Sawtooth oscillations are periodic, sudden relaxations ('crashes') of the core plasma pressure, and serve as destabilizing trigger for NTMs which in turn degrade confinement. If they cannot be avoided, they must be controlled to avoid their coupling to NTMs, either by reducing the magnitude of the crash event or by taking appropriate action to prevent a large crash from triggering a tearing mode (Sauter et al., 2002).

1.3.4 Plasma profile control

The plasma current and density profile control problem can be split into the problem of defining the trajectory which the profiles should follow during their transient evolution towards/from their stationary state, and the question of how to maintain the desired profiles over time during the flat-top. An essential quantities governing the plasma stability and transport is the rotational transform i (or its reciprocal, the safety factor transform q).

$$i = \frac{1}{q} = \frac{d\psi}{d\phi} \quad (1.3)$$

where, ψ is the poloidal magnetic flux, and ϕ the toroidal magnetic flux. Profile control plays a fundamental role especially in so called advanced tokamak scenarios, where the q profile is actively tailored to a desired shape that has a positive influence on the plasma confinement.

1.3.5 Disruption prediction and avoidance

Disruptions must be avoided as they can cause thermal and mechanical stresses on tokamak components. Though multiple reasons for disruptions can be identified (de Vries et al., 2011), most of them are attributed to the plasma approaching a fundamental physical limit, beyond which some instability grows in an uncontrolled way. Monitoring the plasma state for proximity to known physical limits can provide early warning of approaching disruptions.

1.4 Motivation for the thesis

In the context of magnetic confinement fusion, the term pedestal refers to a global increase of a profile (such as the pressure), caused by the formation of a relatively narrow edge plasma region with significantly enhanced profile gradients, associated with an edge transport barrier, characteristic of the H-mode. [1] When transiting from the L-mode to the H-mode, the appearance of the pedestal often leaves the profile gradients in the core region intact (due to profile consistency) whereas the edge gradients increase sharply. Thus, it appears as if the core profiles are merely shifted upward (as if put upon a pedestal), hence the terminology.

Physically, the edge region is complex as it is bounded by the separatrix signalling the transition from the confined plasma with closed field lines to the Scrape-Off Layer (SOL) with open field lines; transport fluxes are large there; and the interaction with the wall (atomic and molecular physics) is important. As a consequence, the understanding of this region, and therefore of the pedestal, is still imperfect. Many attempts have been made to derive scaling laws of phenomenological pedestal parameters (such as its width and height), with limited success. [2] [3]

The thesis aims to combine physics and control in its application to tokamaks. The shape of a plasma in a tokamak device depends on the geometry of the vacuum vessel (VV) and of the external poloidal magnetic field produced by the poloidal field (PF) coils. The performance of a reactor depends strongly on the plasma shape. For example, the maximum value of β , the ratio between the kinetic and magnetic pressures, depends on the plasma elongation (Troyon et al., 1984) (ratio between the height and the width of the plasma). The value of β is an indicator of the efficiency of the magnetic confinement technique. The plasma shape also strongly influences the plasma confinement (Moret et al., 1997). In high confinement (H-mode) plasmas, variation of the plasma shape can increase profiles (such as the pressure), caused by the formation of a relatively narrow edge plasma region with significantly enhanced profile gradients, associated with an edge transport barrier (pedestal) (Leonard et al., 2008) and relating plasma shaping directly to the confinement time and the pedestal stability. Hence, the performance and stability of tokamak plasma configurations depend strongly on the shape of the plasma cross-section in the poloidal plane. It plays a particularly important role in the stability of global magnetohydrodynamic (MHD) modes and in heat and particle transport (Lao et al., 2001; Camenen et al., 2007). The required plasma boundary shape can generally be obtained with reasonable accuracy by preprogramming the appropriate currents in the poloidal field coils. However, departures of the plasma parameters from the model values used in the precalculation, most notably in the plasma current profile, can result in unwanted shape changes. Real-time control thus becomes necessary when better accuracy is required.

The Tokamak à Configuration Variable (TCV) (Hofmann et al., 1994) was designed to allow extreme shaping versatility, which has given rise to such configurations as negative triangularity, elongation > 2.4 , snowflake divertors and doublets. It provides great flexibility in available actuators, thanks to 16 independently powered PF coils and 7 independently steerable ECH/ECCD

launchers, with multiple diagnostics having high spatial and temporal resolution. Exploring unconventional shapes and topologies, in view of possible alternative concepts for a reactor beyond ITER, remains part of the TCV mission. This diversity has recently been further extended to high order null points with more than two divertor legs such as in the so called 'snowflake' divertor (Piras et al., 2009).

The problem of control of plasma shape in tokamaks can be split into two main parts. Firstly, the shape must be determined in real time (Hofmann and Tonetti, 1988b); secondly, coil currents must be adjusted to obtain the required shape (Ferron, 2001). The most complete evaluation of the plasma shape comes from solving the Grad-Shafranov equation, which describes the force balance of tokamak equilibrium using magnetic and other measurements as the boundary conditions. This full reconstruction of the equilibrium has generally been performed offline using a computationally intensive fitting algorithm (Lao et al., 1985). A recently developed real time version of an equilibrium reconstruction code (Moret et al., 2015) provides an approximate solution to the Grad-Shafranov equilibrium which best fits the diagnostic measurements so that an equilibrium solution consistent with force balance, expressed in terms of spatial distributions of the toroidal current density and poloidal flux, is available in real time for accurate evaluation of the discharge parameters. Hence, flux at the desired boundary location can be calculated and compared with a reference flux value, and this flux error is used as a basic feedback quantity for current control loop for the coils used for shape control. This capability has moved the field of plasma boundary control from feedforward to feedback control mode. Realistic solutions to the plasma force balance can now be used as inputs to feedback loops.

The TCV tokamak possesses a new digital real-time control system (Paley et al., 2010) which provides the opportunity to implement a large number of new control algorithms, with applications both to enhanced physics studies and to the development of general tokamak control solutions. The successful implementation of a real-time Grad-Shafranov solver on the digital control system, the extensive digital real-time control system itself, and the flexibility in actuators and diagnostics marks TCV as an ideal platform for the development of a generalised plasma position and shape controller. In addition to the control of basic plasma quantities such as the plasma position, the new system can provide a more precise control of cross-sectional shape, X-points and strike points for advanced plasma configurations.

1.5 Outline of this dissertation

Chapter 1 has provided an introduction to nuclear fusion, plasma physics and the tokamak concept, and highlighted some of the main control problems which must simultaneously be solved during a tokamak discharge.

Chapter 2 will describe the TCV tokamak where all the experimental work reported in this thesis was carried out. The magnetic coil system, and the main diagnostics and heating systems will be described, and particular attention will be devoted to the TCV real-time

Chapter 1. Introduction

control systems, including the new digital control system which has been extensively used to obtain the experimental results. A necessity for the real-time control of the equilibrium, the real-time version of the Grad-Shafranov solver with a sub-ms cycle time will also be discussed.

Chapter 3 presents the controller design for the generalised plasma position and shape controller and the implementation for advanced plasma configurations as well its implementation with the legacy TCV PID controller. The chapter also reports on the formulation of the linearised plasma model of TCV tokamak which is used to verify the controller performance and determine the control parameters. The experimental implementation of the control algorithm on various TCV plasma discharge types is discussed in detail.

Chapter 4 addresses the application of the generalised plasma position and shape controller to the snowflake plasma configuration. The investigation of the optimised control parameters for the controller design for providing control of the poloidal magnetic field at the X-points for a given reference plasma discharge is discussed. The chapter reports on the comparison of the performance of the generalised plasma position and shape controller with the legacy TCV hybrid PID controller on the basis of the main geometrical properties for the snowflake plasma configuration.

Chapter 5 summarizes the main results and conclusion of this work.

2 The TCV tokamak

This chapter describes the TCV tokamak at SPC/EPFL in Lausanne, Switzerland. All the experimental work presented in this thesis was done on this device. Special attention will be devoted to the control systems used, as well as providing an overview of the most relevant diagnostics and actuators.

2.1 Overview

The Tokamak à Configuration Variable (TCV), commissioned in 1992, is an experimental tokamak characterised by a high degree of operational flexibility (Hofmann et al., 1994). It is a compact, highly elongated tokamak, capable of producing limited or diverted plasmas with currents up to 1 MA. The main aim of TCV is to investigate the effects of plasma shape on tokamak physics and performance. Figure 2.1 shows a cutout view of the magnetic coil system, consisting of 16 PF coils, 7 coils forming the Ohmic transformer primary, 16 TF coils as well as two internal (fast) coils placed inside the vessel.

Figure 2.2 represents the TCV poloidal cross-section. The toroidal electric field inside the vacuum vessel is generated by the two OH coil circuits. One circuit powers the coil A1 and the other powers the coils B, C and D connected in series. 16 independently powered poloidal field coils (E-F) provide the extreme plasma shaping flexibility in TCV. The toroidal field in TCV is created by 16 toroidal field coils connected in series. Each coil is connected through a bus, modelled with the two poloidal field coils T1 and T2. T3 represents the return loop of the connection. All toroidal and poloidal power supplies on TCV are based on thyristor semiconductors. The rectifiers are powered by a motor generator with a nominal power of 220 MVA nominal voltage of 10 kV and electric frequency of $96 \div 120$ Hz.

The rectifiers can be controlled in three different ways:

- Current feedback: The current is controlled by the internal controller. This mode is used for the control of the toroidal field coil current.
- Open loop voltage mode: This is the usual method of driving the poloidal field coils.

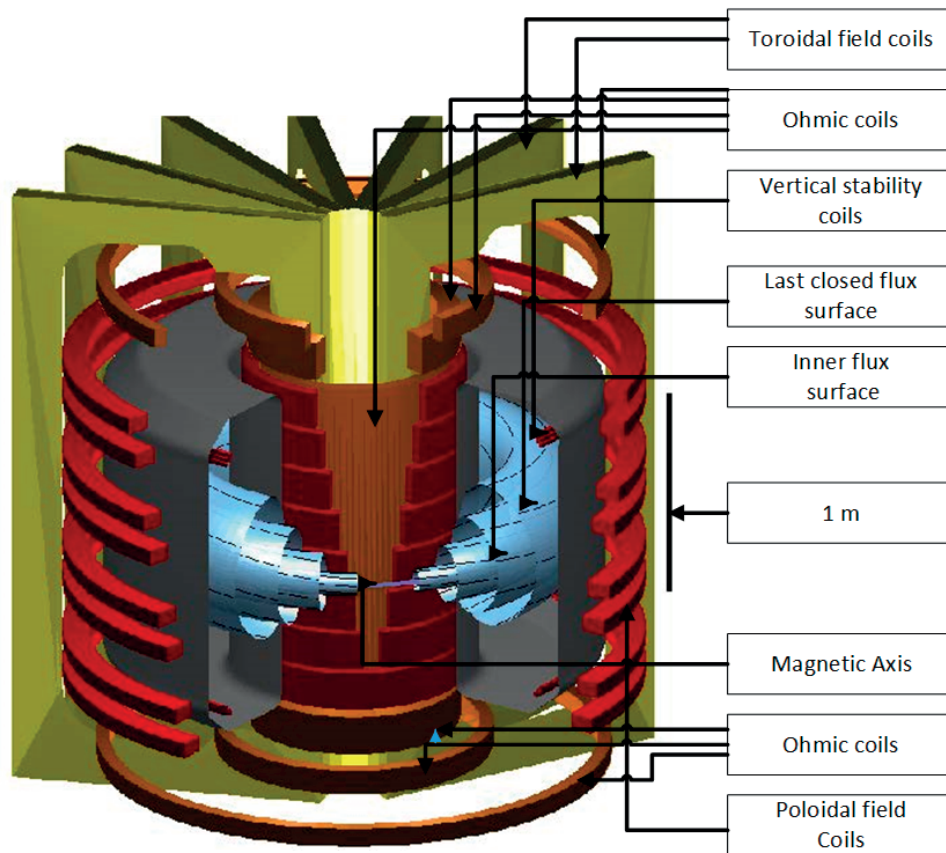


Figure 2.1 – Cutout view of TCV showing poloidal and toroidal field coils, ohmic coils, vacuum vessel and nested plasma flux surfaces with magnetic field lines.

The plasma control system provides the voltage reference signal for each power supply.

- Hybrid mode: The current is controlled by the internal controller through a current reference signal but to minimize the controller work a feedforward voltage is also provided.

Due to the relatively slow switching time of the thyristors and the shielding effect of the vacuum vessel, vertical stabilisation of elongated TCV plasmas is not feasible with the poloidal field coils. Consequently, a fast power supply is used to energize two fast internal coils (G coils) with a switching frequency of 10 kHz.

TCV also hosts a flexible Electron Cyclotron Resonance Heating system (ECH) with high power current drive capabilities. A total power of 4.5 MW can be injected in the plasma from 9 (now 8) gyrotrons. 6 (now 5) gyrotrons operate at a frequency of 82.7 GHz (ECH-X2), matching the second electron cyclotron harmonic frequency on the plasma axis, while the other 3 gyrotrons operate at the third electron cyclotron harmonic frequency 118 GHz (ECH-X3). Figure 2.3 shows the 7 launchers located at the top and on the low field side (LFS) of the vacuum vessel (VV), steerable in real time in both toroidal and poloidal directions. This permits one to heat the plasmas in different poloidal locations during a discharge. Moreover, current drive by the

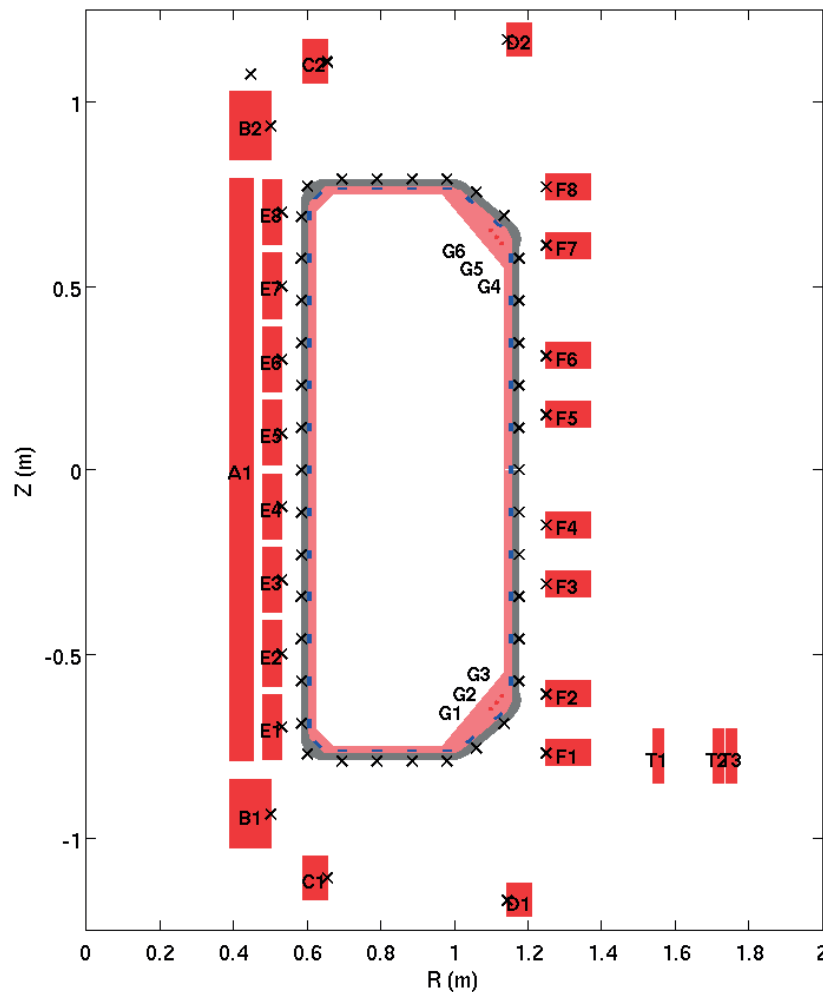


Figure 2.2 – Poloidal view of TCV tokamak showing the poloidal field coil system and magnetic diagnostics. Ohmic coils labeled A-D, PF coils labeled E-F. Internal field coils G (3 turn each, shown separately). Positions of magnetic field probes (rectangles) and flux loops (×) are also shown.

ECH-X2 can be changed in real time, due to the flexibility of changing the toroidal direction of the launchers.

Figure 2.4 shows the schematics of the newly installed neutral beam injector on the TCV tokamak with the capability of injecting 1 MW of neutral beam power for 2 sec. The neutral beam injection (NBI) will provide the capability of heating plasmas at relatively high density and β and to vary the T_i/T_e ratio over a wide domain in supplement to the existing electron heating. The availability of neutral beam heating enables the pursuit of physics investigations in several areas of MHD modes, heat transport and momentum transport.

The TCV vacuum vessel is covered by graphite tiles, thus the main impurity in TCV plasmas is carbon. Every time the TCV vacuum vessel is exposed to air, a baking procedure is executed

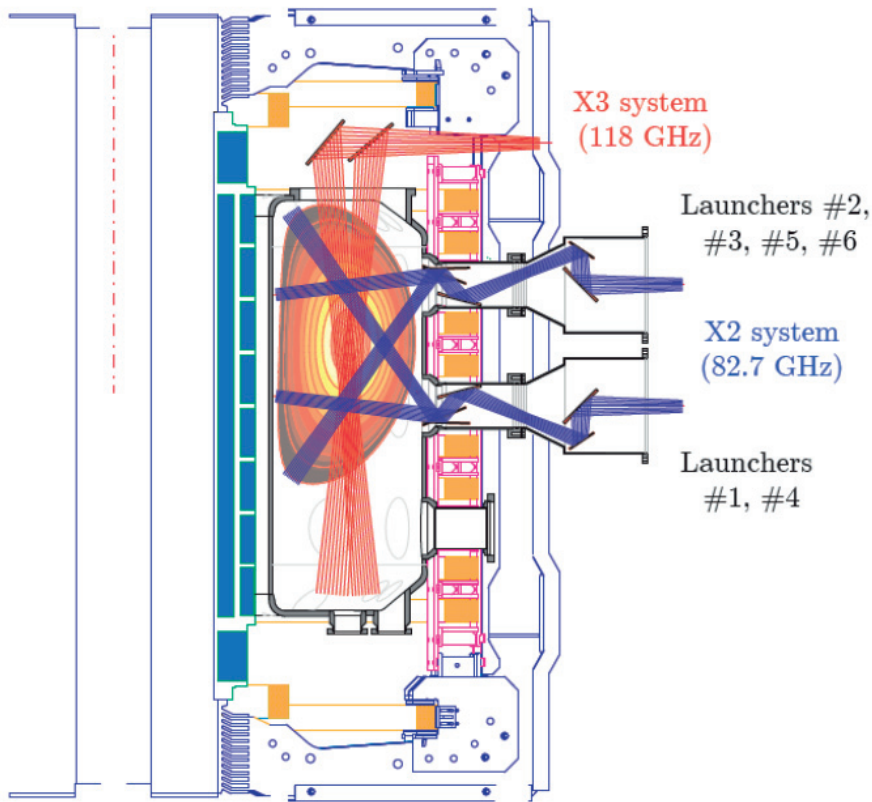


Figure 2.3 – Poloidal view of the TCV tokamak showing the PF coils and the toroidal field coil, as well as low-field-side launched X2 and top-launched X3 ECRH/ECCD systems. The steering ranges in the poloidal plane are also shown. In addition to the movement in the poloidal plane, the X2 launchers can be rotated toroidally to allow ECCD.

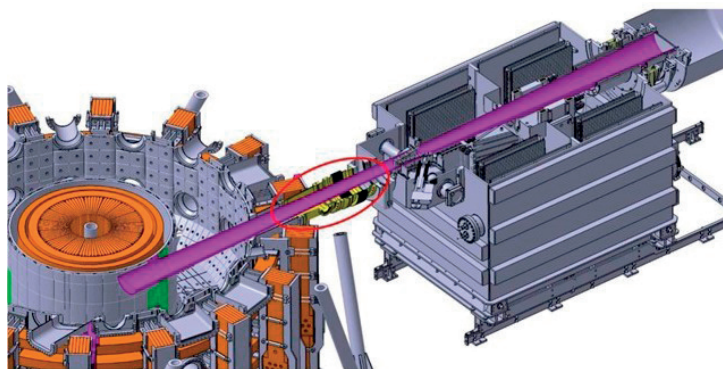


Figure 2.4 – Schematic view of TCV and neutral beam injector.

to remove impurities (e.g. O_2 , N_2 , Ar) accumulated in the wall, followed by boronisation. Between plasma shots, the first wall is cleaned by a Helium glow discharge. The main TCV

plasma parameters are listed respectively in Table 2.1

Parameter	Value
Major Radius	0.88 m
Minor radius	0.25 m
Maximum plasma height	1.45 m
Maximum toroidal field	1.54 T
Plasma current achieved	$I_p \leq 1$ MA
Elongation achieved	$0.9 \leq \kappa \leq 2.8$
Triangularity achieved	$-0.8 \leq \delta \leq 1$
Typical/ Max shot duration	2s/4s
Inter shot delay	> 400s
Energy confinement time	< 50ms for H-modes
Current redistribution time	≈ 150 ms for heated plasmas
Central electron temperature	$T_{e0} < 15$ keV (EC heated)
Central ion temperature	$T_{i0} < 1$ keV
Density range	$0.5E+19 \leq \kappa \leq 20E+19$
PF coils	8+8, copper, water cooled
TF coils	16, copper, water cooled
Ohmic flux swing	3.4 Vs
Installed power	220 MVA
Electron cyclotron	4.5 MW: 6×500 kW @ 82.7 GHz (ECH-X2)
Heating/current drive system	3×500 kW @ 118 GHz (ECH-X3)

Table 2.1 – TCV tokamak parameters

2.2 TCV diagnostics

Many diagnostics are installed on TCV to measure the main plasma parameters. A brief description of the diagnostics is presented in the following section:

2.2.1 Electron diagnostics

- DMPX: The Duplex-Multiwire Proportional X-ray counter (DMPX) is a 64 channel soft X-ray detector. Soft X-ray emission with energy range between 3 and 30 keV are sensitive to the detector. The DMPX has high time and space resolution: the acquisition is performed at 200 kHz. The wire chambers operate in the proportional regime; the measured signal, integrated along the line of sight, is proportional to the mean incident soft X-ray power flux.
- ECE: The ECE radiometer system has 24 channels which analyse the Electron Cyclotron Emission (ECE) generated by the plasma. It provides the radial electron temperature profile on both the high field side (HFS) and LFS of TCV. The frequency bandwidth accessed by the ECE radiometers corresponds to $78 \div 114$ GHz for the HFS and $65 \div 100$

GHz for the LFS systems.

- FIR: The line-integrated density along parallel chords in the vertical direction is measured by a 14-channel Mach-Zehnder type interferometer. The system comprises a FIR (Far Infra Red) laser, pumped by a CO_2 laser and emitting a continuous wave at $214 \mu\text{m}$, and a multi-element detector unit (InSb hot-electron bolometer). The measurement along the central chord is used for real time control of the plasma density.
- TS: The spatial profiles of the electron temperature and density on TCV is measured by the Thomson Scattering (TS) system. The profiles are measured along the line of sight of a laser beam passing through the plasma in the vertical direction at $R = 0.9 \text{ m}$ (mid-radius of the TCV VV). Wide-angle camera lenses collect the scattered light from the observation volumes in the plasma and focus it onto sets of fiber bundles. At present, there are 35 observation positions covering the region from $z = -17 \text{ cm}$ to $z = +66 \text{ cm}$ with a spatial integration length that depends on the channel location. Special channels with higher spatial resolution (integration length 12 mm) are positioned near the top (TS-edge) for observation of the pedestal in H-mode plasmas.
- XTOMO: The TCV soft X-ray tomographic system (XTOMO) consists of 10 pinhole cameras, each with 47 micron thick Be filter, allowing the detection of photons with energies between 1 keV and 10 keV, covering the thermal spectrum of most TCV plasmas. Each camera is equipped with a linear array of 20 p-n junction silicon photodiodes resulting in 200 lines of sight covering the whole plasma cross section.

2.2.2 Ion diagnostics

- CXRS: Local measurements of ion temperature and impurity density are provided by the Charge eXchange Recombination Spectroscopy (CXRS) diagnostic. It also provides information on toroidal and poloidal rotation, through the analysis of spectral moments of impurity line radiation, typically CVI-529.1 nm.

2.2.3 Visible and near-visible radiation

- AXUV: The AXUV (Absolute eXtreme UltraViolet bolometer cameras) diagnostic consists of two sets of 7 (currently 6) pinhole cameras. Each camera has 20 lines-of-sight, so that 2×140 channels are available in all. The two camera sets have identical geometries, i.e. the corresponding channels in each camera view essentially the same plasma volume. The distribution of the lines-of-sight in a single poloidal cross section is such that tomographic reconstruction of the 2D emission profile is possible.
- BOLO: The foil bolometer (BOLO) system consists of 8 pinhole cameras (one top, one bottom and six lateral) each with 8 channels - gold foils which heat up due to the impact of plasma radiation and neutral particles. 2D tomographic reconstruction of the total radiated power is possible.
- FastCam: The plasma radiation in the visible spectrum is detected by a Fast Visible Camera (FastCam) installed on a TCV equatorial port. The camera has a very high

temporal resolution (up to 250000 fps for a 128×16 pixel array).

- MultiCam: MultiCam is a multi-camera system composed of four PCO Pixelfly visible cameras. The light coming from the plasma through relay optics is distributed to the cameras by a series of beam splitters. A filter can be placed in front of each camera. This way each camera observes a specific part of the visible spectrum in the very same volume of the plasma. The imaging frequency of these cameras is 50 fps at full (640×480) resolution.
- PD: A set of 15 photodiodes (PDs) are installed on TCV. The signals are amplified onboard to improve the robustness of the transmission. A set of filters is installed in front of the diodes to acquire different lines of the spectrum. 6 PDs have an H_α filter and are installed on the lateral ports and another 9 PDs are installed on the top of TCV and they can detect all plasma radiation.

2.2.4 Edge diagnostics

- LP: The TCV Langmuir probes are machined in graphite and are of the domed design with a diameter of 4 mm. The probe head protrudes nominally by only 1 mm beyond the tile surface. A total of 72 Langmuir probes (LP) have been installed on TCV. The system is robust and precise in terms of the stability of the probes to vibrations during operation and has a spatial resolution of 11 mm on the bottom of the chamber and 14 mm on the central column.
- TC: 15 Thermocouples (TCs) are installed in the vessel floor and 4 in the central column. The temperature rise on each thermocouple only starts to be visible several seconds after the shot(s), hence the information gathered from them is mostly related to the cooling-down of the tile's graphite material.
- IR: TCV is equipped with two infrared thermography (IR) systems, namely the Vertical IR camera (VIR) and the Horizontal IR camera (HIR), used to measure the temperature of the graphite tiles covering the floor of the vessel and the central column at a fast time scale (25 kHz), respectively. In this thesis, only the HIR camera has been utilised for obtaining the heat deposition on the central column. HIR is based on a IRCam EQUUS 81k M fast framing camera. Its detector is composed by 320×256 CdHgTe pixels, sensitive to mid-wave IR spectrum, nominally to photons with wavelength $3.7 \pm 0.2 \mu m < \lambda < 4.8 \pm 0.2 \mu m$. The photons emitted from the tile surfaces in the short to medium wavelength infrared range are detected by the chip, amplified and subsequently digitised on 14 bits.

2.2.5 Magnetic diagnostics

- The TCV magnetic diagnostic system consists of a set of flux loops, magnetic field probes and saddle coils. The location of flux loops and field probes is shown in Figure 2.2. There are four poloidal arrays of 38 magnetic probes each, placed inside the vessel in 4 toroidal sectors separated by 90° . They measure the time derivative of the magnetic field

tangential to the vessel, and analog integrators are used to obtain an estimate of the magnetic field. A complementary toroidal probe array is used for analyzing the toroidal composition of magnetic perturbations. 61 flux loops placed around the vessel and near each coil are used to measure the poloidal flux. 24 saddle coils placed around the vessel complement the magnetic system by providing estimates of non-axisymmetric error fields. Since no Rogowski coil is installed on TCV, the plasma current is obtained by trapezoidal integration of the discrete magnetic probe measurements. A diamagnetic loop (DML) measures the total magnetic energy and is used as an extra constraint in equilibrium reconstruction. Further details on the magnetic diagnostic system are given in (Moret et al., 1998), (Piras et al., 2010). Magnetic probe signals and flux loops are used for plasma control and MHD analysis and are available in the digital real-time control system as well.

2.3 Real-time control systems

Two types of control systems are installed on TCV. The first is the original control system referred to as the ‘Hybrid’ control system. The second is the new, fully digital, distributed control system named ‘SCD’ (Système de Contrôle Distribué). It is an experimental system which is used for advanced control experiments and is envisaged to replace the old system entirely in the future.

2.3.1 The ‘Hybrid’ plasma control system

The ‘hybrid’ control system forms the backbone of TCV control. It consists of a set of analog matrix multipliers, the coefficients of which are digitally programmable and can be switched during the TCV shot.

The diagnostic signals necessary for real time control are first passed through the A matrix, which has ≈ 120 diagnostic signals inputs, and generates estimates of quantities to be controlled (‘observables’) as linear combinations of the input signals. The set of observables are I_p , the PF coil currents, the difference between the currents in the two sets of Ohmic coils, the vertical position estimator zI_p , the radial position estimator, the elongation estimator and the line-integrated density. These are then subtracted from reference signals coming from a waveform generator (wavegen), yielding 24 error signals. The error signals are fed to P , I and D circuits containing analog implementations of proportional gain, integrator and derivative terms. The outputs of these circuits are then passed to the G_2 , G_1 and G_3 matrices respectively. Not only do these define the Proportional, Integral and Derivative gains, they also assign each error signal to a set of actuators (16 poloidal field coils, 2 Ohmic coils and density control valve). Finally, the actuator command signals are passed through the M matrix whose role is to decouple the mutual inductances and to compensate for resistive voltage of the coils. In other words, it ensures that the response of each individual coil current to a voltage command is that of a pure integrator. Figure 2.5 shows the schematic of the analog TCV control system

and its connection to various diagnostics and actuators (Le et al., 2014).

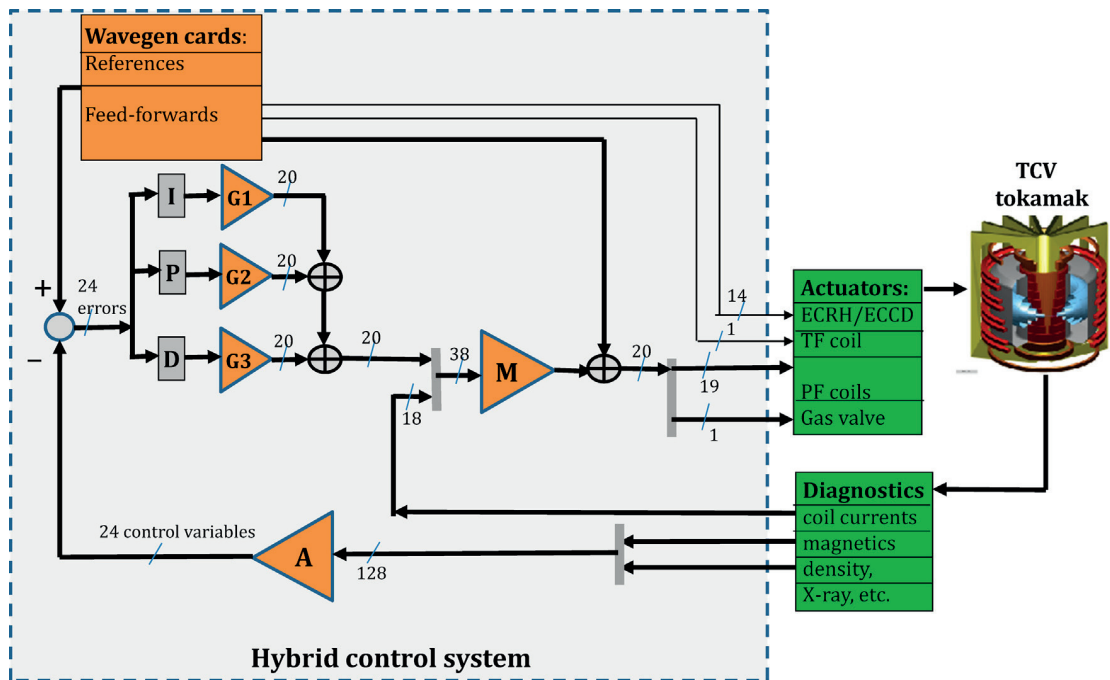


Figure 2.5 – Diagram of the original TCV control system and its connections to diagnostics and actuators.

The hybrid system is limited by the fact that it cannot perform any non-linear operations, other than gain switching. It also has a limited number of output channels, meaning the number of actuators which can be simultaneously controlled is limited: in particular the parameters of the TCV ECH system could not be controlled in real-time and were, for the majority of TCV's operational history, controlled by feedforward reference waveforms. These limitations, coupled to the increasing capabilities of digital platforms, have prompted the development of new TCV control systems based on a fully digital architecture.

2.3.2 The 'SCD' digital plasma control system

A new digital control system named from the French acronym for SCD "Système de Contrôle Distribué" for TCV, featuring massive multichannel capabilities and high flexibility, allowing many more real-time diagnostic signals as inputs for real-time control, and capable of controlling all the available actuators, was installed on TCV in 2008 (Paley et al., 2010). The performance of the legacy control system of TCV has been successfully replicated in the digital control system with the addition of new features for e.g. improved control of the ohmic transformer coil during non-inductive plasmas and improved density control by gain scheduling, which could not be handled by the analog electronics of the original system. Furthermore, the system has been successfully extended to advanced experiments on MHD and plasma profile control, as well as to incorporate real time plasma transport simulation.

Chapter 2. The TCV tokamak

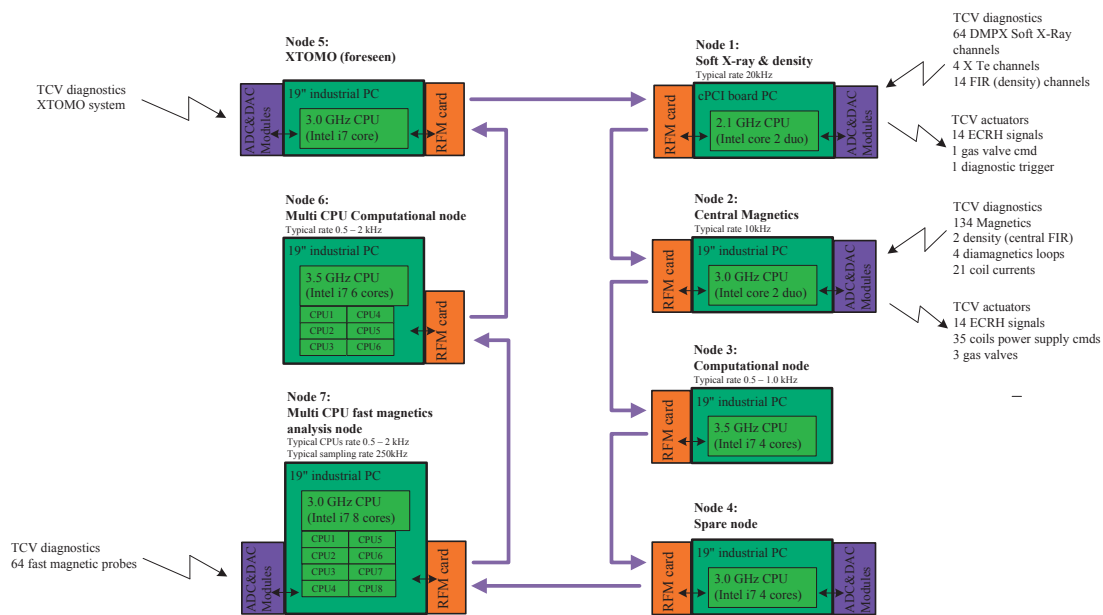


Figure 2.6 – Diagram of the SCD control system nodes and their respective connections to diagnostic signals and actuators.

The SCD hosts diagnostic inputs and actuator outputs and consists of a set of independent nodes linked via shared reflective memory. Each node can have a different cycle time, varying between 50us and 1ms, depending on the needs for acquisition and computational complexity of algorithms. The design of the diagnostic signal processing and control algorithms is performed in Matlab-Simulink, providing a natural framework for modelling and control design. For real-time execution, C code is generated from the Simulink block diagram, compiled, with the Simulink Embedded Coder, into a Linux shared library and distributed to target nodes in the discharge preparation phase. During the TCV discharge, an application on each node is executed that dynamically loads the shared library at runtime. Upon the completion of the discharge, all data stored in RT nodes is copied to the host computer and archived to the TCV database.

Figure 2.6 shows the SCD control system layout with the connectivity to the diagnostics and actuators. The nodes with ADCs and DACs are interfaced to the machine's diagnostics systems and actuators. Node 1 is interfaced to 2 soft-X ray diagnostics (DMPX, or Duplex Multiwire Proportional soft X-ray counter, a pinhole type soft-X camera; and X-Te, a four filter soft-X-ray spectrometer that provides the central electron temperature using the differential filter method). It is also interfaced to the 14 vertical chords of the Far InfraRed (or FIR) interferometer providing the electron density profile information. Node 2 is the central core of the system and acquires all magnetic measurements from the tokamak and is thus responsible for plasma shape and position control; it also acquires the central FIR channel for real-time control of the density. This node is used routinely as the main plasma position and density controller and is almost always the RFM master node. Node 3 is a computational

node that computes the plasma magnetic equilibrium in real-time. Node 4 is a hardware and software clone of node 2, It serves as a replacement node in case of node 2 failure. Node 5 is an acquisition and processing node, presently under commissioning, connected to the 200 channel soft X-ray tomographic (XTOMO) system. Node 6 is a very recently installed multicore computational node that has been used to run multicore complex control codes (a faster real time equilibrium reconstruction replica and real-time modeling based advanced plasma performances controllers). Finally, node 7 is devoted to real-time analysis of fast magnetic perturbations in the plasma.

The link between all RT nodes is provided by reflective memory which features a 128MB memory area that is shared across all the nodes. A fiber optic ring network links the reflective memory network cards in each node. Data written by one node to a memory address within this shared memory area will automatically appear at the same memory address within the rest of the nodes after a very short delay (0.7 ms). The RFM is partitioned in a small control parameter section and large data area. Each node is assigned a separate section within the data area in which to write data, preventing the nodes from overwriting data areas outside their assigned write area (Le et al., 2014).

The SCD code is divided into two main sections:

- Hardware interface code written in C/C++ language by the system developers. This provides the input/output interface to the control algorithm code. Once compiled, the executable is uploaded to real-time computer nodes, where it is considered fixed and unchanging between plasma shots.
- Control algorithm code realised in MathWorks-Simulink block programming language by the control algorithm author, using Simulink templates given by the system developers. It performs signal processing and computational actions to provide output signals consisting of new values for the actuators, the reflective memory and other signals (probe signals) used for post-shot analysis. This algorithm is in user-friendly Simulink block format and is automatically converted into target code that is a dynamically linked shared object library by Math Works Simulink Embedded Coder.

The SCD also provides the flexibility for verifying a new or modified algorithm before implementing it on an actual plasma discharge. The SCD architecture can be activated in background on a plasma discharge controlled by the original hybrid control system (an extensive analog multichannel multiplication system digitally reconfigurable with PID control blocks). This not only facilitates the verification of algorithms running on different nodes but also estimates the algorithm execution time with respect to each node as well. Furthermore, the digital control system can also perform runs on individual nodes in a standalone fashion or on the entire control system offline, from the tokamak. All the algorithms running on individual nodes are executed with noise in the ADC inputs, which provides an estimate of the exact execution time based on the assumption that the computational complexity of the algorithm is independent of the input ADC dataset.

2.4 Real-time equilibrium reconstruction solver

The magnetic lines that guide the particles around the major axis of the torus are helices, i.e. a combination of toroidal and poloidal magnetic fields. It is possible to use the poloidal component of these magnetic lines to define nested toroidal surfaces corresponding to constant values of the poloidal flux function ψ . The plasma boundary is defined as the outermost closed flux surface contained inside the device. It is the shape of this boundary that is generally referred to as plasma shape. Unfortunately, the plasma shape cannot be directly measured, and for control purposes must be estimated in real time using indirect measurements of magnetic flux and field. One of the available methods for plasma boundary estimation is based on equilibrium reconstruction. Equilibrium codes, such as EFIT (Ferron et al., 1998), calculate the distributions of flux and toroidal current density over the plasma and surrounding vacuum region that best fit, in a least square sense, the external magnetic measurements, and that simultaneously satisfy the MHD equilibrium equation (Grad–Shafranov equation). Once the flux distribution is known, it is possible to reconstruct the plasma boundary. Alternatively, the boundary is sometimes calculated making use of reconstruction codes, such as XLOC (Sartori et al., 2003), that are limited to locating the boundary and are not aimed at evaluating parameters describing the plasma internal features.

The deployment of the real-time version of the Grad-Shafranov equilibrium reconstruction code LIUQE (Hofmann and Tonetti, 1988a), with a sub-ms cycle time has fulfilled a necessary requirement for the development of a real time plasma position and shape control algorithm. The successful implementation of RTLIUQE (Moret et al., 2015) on SCD has facilitated the design of a new generalised plasma position and shape controller, based on the information of poloidal flux and magnetic field provided by the real-time Grad-Shafranov solver. In axisymmetric geometry, assuming isotropic pressure and no net fluid velocity, the equations describing ideal magnetohydrodynamic equilibrium,

$$\begin{aligned} j \times B &= \nabla p \\ \nabla \times B &= \mu_0 j \\ \nabla \cdot B &= 0 \end{aligned} \tag{2.1}$$

where p is the plasma pressure, B is the magnetic field and j is the plasma current density. Equations (2.1) be combined, by writing B in cylindrical coordinates r, z, ϕ as

$$B = -\frac{1}{2\pi r} \frac{\partial \psi}{\partial z} \nabla r + \frac{1}{2\pi r} \frac{\partial \psi}{\partial r} \nabla z + T \nabla \phi, \tag{2.2}$$

where $T = r B_\phi$, into a second order differential Poisson like equation:

$$\Delta^* \psi = -2\pi \mu_0 r j_\phi \tag{2.3}$$

with

$$j_\phi = 2\pi \left(r \frac{dp}{d\psi} + \frac{T}{\mu_0 r} \frac{dT}{d\psi} \right) \quad (2.4)$$

and the definition of the elliptical operator

$$\Delta^* = r \left(\frac{\partial}{\partial r} \right) \left(r \frac{\partial}{\partial r} \right) + \frac{\partial^2}{\partial z^2} \quad (2.5)$$

Here p and T are arbitrary functions of the poloidal magnetic flux ψ only. Combining these two equations gives the Grad-Shafranov equation:

$$\Delta^* \psi = -4\pi^2 \mu_0 r \left(r p' + \frac{T T'}{\mu_0 r} \right) \quad (2.6)$$

The goal of the inverse equilibrium problem is to identify the two functions $p'(\psi)$ and $T T'(\psi)$, together with a flux function $\psi(r, z)$, that satisfy (2.6) and that best reproduce the available experimental measurements of parameters related to the physical quantities behind these functions.

In the presence of an external conductor, toroidal current density, j_e , (2.3) is modified as follows:

$$\Delta^* \psi = -2\pi \mu_0 r (j_\phi + j_e) \quad (2.7)$$

$j_\phi = 0$ outside the plasma domain Ω_p , i.e. where flux surfaces field lines are not closed and touch the limiter. Dirichlet boundary conditions must be specified at the boundary of the finite integration domain Ω . For clarity, the contributions from the plasma current ψ_p and the external currents ψ_e are separated and the edge condition is given as $\psi(r, z) = \psi_b(r, z) = \psi_{bp} + \psi_{be}$ on $\partial\Omega$ where

$$\psi_{bp} = \int M(r_b, z_b, r', z') j_\phi(r', z') dr' dz' \quad (2.8)$$

and

$$\psi_{be} = \int M(r_b, z_b, r', z') j_e(r', z') dr' dz' \quad (2.9)$$

Here $M(r, z, r', z')$ is the mutual inductance between coaxial circles located at the plasma boundary (r_b, z_b) and external conductors (r', z') . Except for trivial functions p' and $T T'$, that are inadequate for realistic equilibrium, and especially because the plasma is surrounded by a vacuum region whose boundary depends on the solution itself, (2.6) is intrinsically non linear and calls for dedicated solving methods. The simplest algorithm, the so called Picard

iterations, consists of solving iteratively (2.7):

$$\Delta^* \psi^{(t+1)} = -2\pi\mu_0 r \left(j_\phi^{(t)}(r, \psi^{(t)}) + j_e \right) \quad (2.10)$$

where t labels the iteration number. In the framework of equilibrium reconstruction, the boundary between the plasma volume and the vacuum is updated at each iteration based on $\psi^{(t)}$. The functions $p'^{(t)}(\psi^{(t)})$ and $TT'^{(t)}(\psi^{(t)})$ forming the plasma current density are also adjusted at each iteration to best reproduce available experimental measurements, thus justifying the t index in $j_\phi^{(t)}$ in (2.10). The iterative procedure is seeded with an initial guess for the current density $j_\phi(r, z)^{(0)}$. A real time implementation of the inverse equilibrium reconstruction for TCV imposes stringent constraints on the computation cycle time. The required cycle time is imposed by the characteristic time constant of the vacuum vessel image currents and the corresponding response time of the poloidal field coil power supplies, typically 1 ms. For the real time implementation of LIUQE on TCV, consideration of the efficiency of competing numerical techniques in all steps of the algorithm, together with an efficient, yet user friendly, code generation using the Simulink programming environment, has yielded a sub ms cycle time. An in-depth description of the main features and the real-time implementation of LIUQE can be found in (Moret et al., 2015).

3 Generalised plasma position and shape controller design

The chapter describes the design and the key features of the new generalised plasma position and shape controller. The formulation of the linearised plasma model of TCV that is used to verify the controller performance and determine the control parameters is reported. The experimental implementation of the control algorithm on various TCV plasma discharge types is discussed. A brief overview of the plasma modelling, controller design and experimental results, as well as an outlook for the physics applications of the controller to advanced plasma configurations, is also provided.

3.1 Introduction

The plasma shape requirements in a practical, highly efficient tokamak are very stringent. High performance in tokamaks is achieved by plasmas with elongated poloidal cross section. Since such elongated plasmas are vertically unstable (Lazarus et al., 1990a), active position control is clearly an essential feature of all machines. Additionally, in order to obtain the best performance from a given device, it is necessary to maximise the plasma volume within the available space; hence, the ability to control the shape of the plasma while ensuring adequate clearance between the plasma and the plasma-facing wall components is a crucial asset in modern tokamak operation. In tokamaks, the shape of the plasma cross-section is observed to strongly influence a wide range of plasma properties, such as the plasma pressure and current limits (Hofmann et al., 1998) and the sawtooth stability (Reimerdes et al., 2000; Martynov et al., 2005). Experimental investigations in TCV have revealed that the energy confinement time (the ratio of the energy stored in the plasma to the power used to heat it, a confinement figure of merit) nearly doubles when going from positive to negative triangularity (Pochelon et al., 1999). Accurate shape control can not only take full advantage of such properties, but can also allow detailed comparisons between experiment and modeling and testing of theoretical models of plasma stability and confinement. Plasma shaping is also effective in stabilising MHD modes and preventing disruptions, especially in the current ramp-up, which is of key importance for the ITER high-currents scenarios. Active plasma shaping thus has a direct impact on MHD stability and on heat and particle transport.

Chapter 3. Generalised plasma position and shape controller design

On the TCV tokamak, plasma shaping is especially challenging, as the device features a highly elongated vessel that does not intrinsically constrain the plasma shape and is specifically designed for shape versatility, with a highly flexible poloidal-field coil system. Indeed, TCV accommodates a large variety of plasma shapes, together with various divertor configurations, including single and double null divertor with a broad range of strike point positions and flux expansions. This flexibility has been further extended in recent years to high order null points with more than two strike points such as in the so called ‘snowflake’ divertor (Piras et al., 2009). Even more recently, other advanced configurations such as the super-X, X-divertor, and X-point-target divertor have been explored in TCV (Theiler et al., 2017; Reimerdes et al., 2016).

On TCV, the creation of an extreme variety of plasma shapes and magnetic configuration is accomplished with the help of the Matrix Generation Algorithm and Measurement Simulator (MGAMS) and Free Boundary Tokamak Equilibrium (FBTE) codes (Hofmann, 1988; Hofmann et al., 1995), the suite of software tools used routinely on TCV to determine the feedforward poloidal coil currents as well as the feedback parameters for a given plasma configuration. Until now, the TCV plasma shape has been controlled almost entirely in feedforward mode, with the exception of a linearised elongation controller employing a simplified estimator, used in some discharges (Paley et al., 2007). A real-time control algorithm capable of not only providing control of plasma position but also high order shape moments, X-points and strike points would thus be highly desirable for optimizing performance in future TCV campaigns. Deviations from the assumptions used in calculating the feedforward parameters can and do cause departures from the desired shape in the absence of feedback control. This happens in particular as a result of auxiliary heating and current drive altering the current profile. Feedback control is also clearly superior to pure feedforward control in its ability to deal with disturbances. Success in controlling plasma shapes in feedforward mode in TCV has often been achieved by virtue of tuning over multiple discharges.

Feedback plasma shape control in tokamaks involves basically two steps:

- Identification of the plasma boundary in real time.
- Adjustment of the poloidal field coil currents to bring the real shape as close as possible to the preprogrammed shape.

The deployment of the real-time version of the Grad-Shafranov equilibrium reconstruction code LIUQE (Hofmann and Tonetti, 1988a), i.e., RTLIUQE (Moret et al., 2015), with a sub-ms cycle time (0.4ms), has fulfilled a necessary requirement for the development of a real time plasma position and shape control algorithm, based on the information of poloidal flux and magnetic field provided by the real-time Grad-Shafranov solver. The latter provides an approximate solution to the Grad-Shafranov equilibrium relation that yields the best fit to the diagnostic measurements, with additional assumptions on the plasma kinetic profiles, as the diagnostic data are generally insufficient to constrain the problem towards a unique solution. The solutions are produced at a rate that is amply sufficient for discharge control,

3.2. Plasma position and shape controller design.

with the sole exception of the control of the vertical stability on a sub-ms time scale, which is still entrusted to the legacy analogue control system.

The extensive poloidal-field coil system and the recent successful implementation of RTLIUQE on TCV have paved the way to the design of a new plasma position and shape controller. The Matlab-Simulink environment of the digital control system (Paley et al., 2010) of TCV provides a flexible platform for implementing new algorithms in parallel with the legacy analogue TCV controller. As a minor but important step along this path, a new controller was also developed to actuate the sign switching of the poloidal-field coil currents (the so-called ‘sign-bit controller’), discussed in appendix A.2.

3.2 Plasma position and shape controller design.

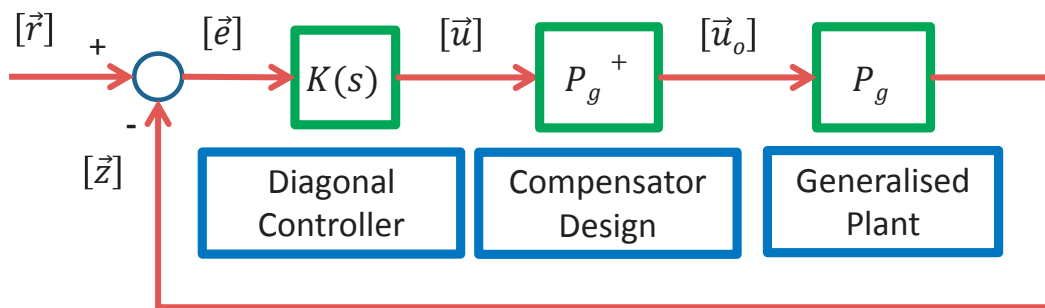


Figure 3.1 – Simplified block diagram representation of plasma shape and position control algorithm.

The generalised plasma position and shape controller is primarily based on the isoflux control scheme. The plasma target shape is defined as a set of control points on the desired plasma boundary, and the poloidal flux at control points is controlled to be equal (Ferron et al., 1998). For a limiter plasma discharge, the flux differences between adjacent control points are controlled. In the case of divertor discharges, the primary X-point is used as the reference point and the flux error differences between it and the other control points on the plasma boundary are controlled. Similarly, the divertor leg is controlled by requiring the poloidal flux on the control points on the leg to be equal to that of the X-point. X-points are obtained by controlling the poloidal magnetic field at the reference X-point position to zero.

The generalised plasma position and shape controller was developed in two stages: a time-invariant version at first, and then a more general time-varying controller.

3.2.1 Time invariant controller design

The architecture of the plant used for the design of the generalised plasma position and shape controller is a MIMO (multiple input and multiple output) system with poloidal field coil currents as inputs and the controlled variables as outputs. A change in one of the inputs will affect all the outputs of the system, that is, there is an interaction between the inputs and the outputs. A specific aim of the design is to convert this to a non-interacting system, where an input only affects its corresponding output. Figure 3.1 shows the simplified block diagram for the plasma position and shape controller algorithm. A non-diagonal generalised plant P_g is defined, where a change in its input would affect all its outputs. Consequently, a compensator design P_g^+ , pseudo-inverse of the static (DC) gain of the generalised plant, is derived, provided that P_g has a full row (output rank), to counteract the interaction of the plant. The pseudo inverse is a generalization of the matrix inverse when the matrix may not be invertible. If P_g is invertible, then the pseudo inverse is equal to the matrix inverse. However, the pseudo inverse is defined even when P_g is not invertible. More formally, the pseudo inverse, P_g^+ , of an m-by-n matrix is defined by the unique n-by-m matrix satisfying the following four criteria (Campbell and Meyer, 1979),

1. $P_g P_g^+ P_g = P_g$
2. $P_g^+ P_g P_g^+ = P_g^+$
3. $(P_g P_g^+)' = (P_g P_g^+)$
4. $(P_g^+ P_g)' = (P_g^+ P_g)$

The result is a ‘newly’ shaped plant, $G_s = P_g P_g^+$, which is nearly diagonal and easier to control than the original plant P_g . A diagonal proportional and integral controller K_s is utilised, with diagonal gain matrices K_{sp} and K_{si} to be designed. They are determined with help of a plasma model described in section 3.3 or are tuned by performing experimental tests. The control law takes the form of (3.1), where \vec{u} is the control signal (the vector of 16 poloidal field coil current references) and $\vec{e} = (\vec{r} - \vec{z})$ is the error defined as the difference between the reference \vec{r} and the controlled variables \vec{z} .

$$\vec{u} = K(s)\vec{e}$$

$$K(s) = K_{sp} \left(1 + \frac{K_{si}}{s} \right) \tag{3.1}$$

Figure 3.2 shows the schematic block diagram for the determination of a generalised plant P_g . A plant P is defined, which accepts poloidal-field coil currents (E and F coils) as inputs and outputs the poloidal flux $\vec{\psi}_b$ and poloidal magnetic field \vec{B}_p at the control points. The definition of P is an approximation as it only includes the DC component of a highly dynamic

3.2. Plasma position and shape controller design.

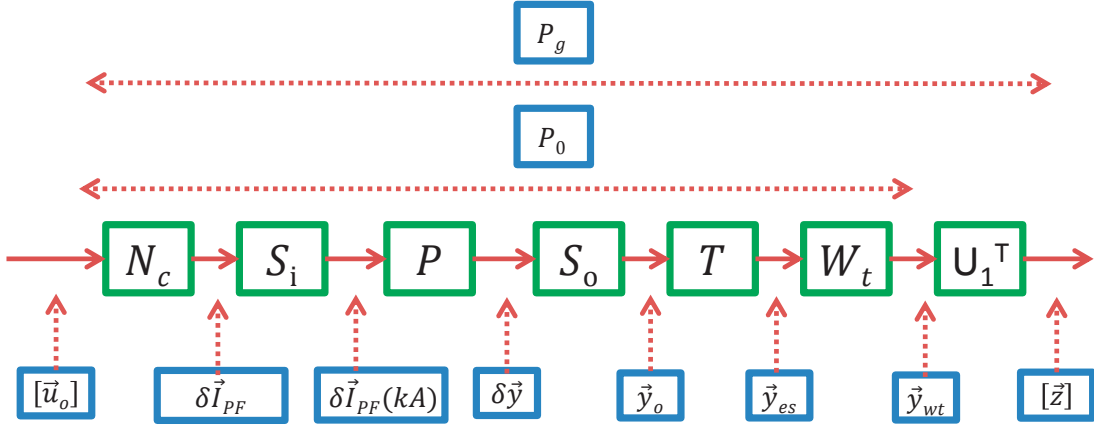


Figure 3.2 – Schematic block diagram for the generalised plant.

system. In particular, the issue of vertical stability, i.e., the growth of the fast axisymmetric mode, is assumed to be entirely decoupled (e.g., separated in frequency space) from the shape-control problem and to be handled by a separate system (namely, the vertical stability control loop in the legacy hybrid control system). This assumption can never be strictly true, so improvements in controller decoupling are under consideration for the future. Hence, neglecting the dynamics and linearising around an equilibrium point, the plant $P \in \mathbb{R}^{n_y \times n_c}$, with $\delta \vec{I}_{PF}$ as inputs and $\delta \vec{y}$ as outputs is given by (3.2), such that $\delta \vec{y} = P \delta \vec{I}_{PF}$, where $n_y = n_b - 1 + n_d - 1 + 2n_x$ with n_b , n_d and n_x the number of control points on the plasma boundary, divertor leg and X-points and n_c number of poloidal field coils. Here, G_b is the matrix such that $\delta \vec{\psi}_b = G_b \delta \vec{I}_{PF}$, where $\delta \vec{\psi}_b$ is the poloidal flux at the control points on the plasma boundary, G_d is the matrix such that $\delta \vec{\psi}_d = G_d \delta \vec{I}_{PF}$, where $\delta \vec{\psi}_d$ the poloidal flux at the control points on the divertor leg, G_{B_p} is the matrix such that $\delta \vec{B}_p = G_{B_p} \delta \vec{I}_{PF}$, where $\delta \vec{B}_p$ is the poloidal magnetic field (R and Z components) at the X-points. M_b is the near-diagonal matrix that transforms absolute poloidal fluxes to flux differences between points and, similarly, M_d is the matrix that transforms absolute fluxes on divertor-leg points to flux differences with respect to the X-point.

$$P = \begin{pmatrix} M_b G_b \\ M_d G_d \\ G_{B_p} \end{pmatrix} \quad (3.2)$$

The control algorithm includes a constraint, which guarantees that the average addition of poloidal flux at the control points defining the plasma boundary is zero, to prevent interference with the plasma current control. To achieve this, a null space basis $N_c \in \mathbb{R}^{n_c \times n_c - 1}$ is determined such that $[\mathbf{1}^T G_b] N_c \vec{u}_o = 0 \forall \vec{u}_o \in \mathbb{R}^{n_c - 1}$, where $\delta \vec{I}_{PF} = N_c \vec{u}_o$. An input scaling matrix $S_i \in \mathbb{R}^{n_c \times n_c}$ ensures common units for the poloidal field coil currents (kA in practice) such that

Chapter 3. Generalised plasma position and shape controller design

$\delta \vec{I}_{PF}(kA) = S_i \delta \vec{I}_{PF}$ and an output scaling matrix $S_o \in \mathbb{R}^{n_y \times n_y}$ scales the plant outputs $\delta \vec{y}$ to dimensionless quantities \vec{y}_o that are roughly comparable in magnitude such that $\vec{y}_o = S_o \delta \vec{y}$.

A crucial element in the design is the matrix $T \in \mathbb{R}^{n_y+2 \times n_y}$, given by (3.3), which converts the dimensionless plant outputs \vec{y}_o to physically meaningful estimators \vec{y}_{es} such that $\vec{y}_{es} = T \vec{y}_o$, for e.g., vertical and radial plasma position estimates, where $\vec{\psi}_Z = M_b \vec{d}\psi / dZ / \|M_b \vec{d}\psi / dZ\|$ and $\vec{\psi}_R = M_b \vec{d}\psi / dR / \|M_b \vec{d}\psi / dR\|$ are the vectors representing the change in the controlled poloidal flux differences due to vertical and radial displacement at the control points on the plasma boundary. A projection of the dimensionless plant outputs onto the vectors corresponding to a vertical and a radial displacement ensures that the first two entries are estimates of the radial/vertical position. The matrix T provides the flexibility of defining additional plasma estimators, such as, e.g., plasma triangularity and elongation.

Finally, the estimators \vec{y}_{es} are weighted with the help of a weight matrix $W_t \in \mathbb{R}^{n_y+2 \times n_y+2}$ to provide weighted meaningful quantities \vec{y}_{wt} such that $\vec{y}_{wt} = W_t \vec{y}_{es}$. W_t gives the means to prioritise the various meaningful plasma estimators based on their level of importance for a given plasma configuration.

$$T = \begin{pmatrix} \vec{\psi}_Z^T & 0 & 0 \\ \vec{\psi}_R^T & 0 & 0 \\ I & 0 & 0 \\ 0 & I & 0 \\ 0 & 0 & I \end{pmatrix}, \quad (3.3)$$

A new plant $P_o = W_t T S_o P S_i N_c$, $P_o \in \mathbb{R}^{n_y+2 \times n_c-1}$ is thus finally defined. The next step is to perform a singular value decomposition (SVD) (Skogestad and Postlethwaite, 2005) of $P_o = U \Sigma V^T$, which provides a matrix V , representing a set of orthogonal vectors in the admissible input coil current space and U , the output directions. This organises the controlled variables into large and small singular values represented by (3.4), and as a result provides the freedom of limiting the control to the n_1 'largest' singular values of Σ_1 , obtained by projecting the weighted errors on the output space of these singular values, U_1 .

$$P_o = \begin{pmatrix} U_1 & U_2 & U_3 \end{pmatrix} \begin{pmatrix} \Sigma_1 & 0 \\ 0 & \Sigma_2 \\ 0 & 0 \end{pmatrix} \begin{pmatrix} V_1^T \\ V_2^T \end{pmatrix} \quad (3.4)$$

The generalised plant P_g is then defined as $P_g = U_1^T P_o$. Due to the presence of a constraint in the controller formulation, a degree of freedom is lost and at most $n_c - 1$ singular values can be controlled, thus $P_g \in \mathbb{R}^{n_c-1 \times n_c-1}$. In order to control different meaningful plasma estimators,

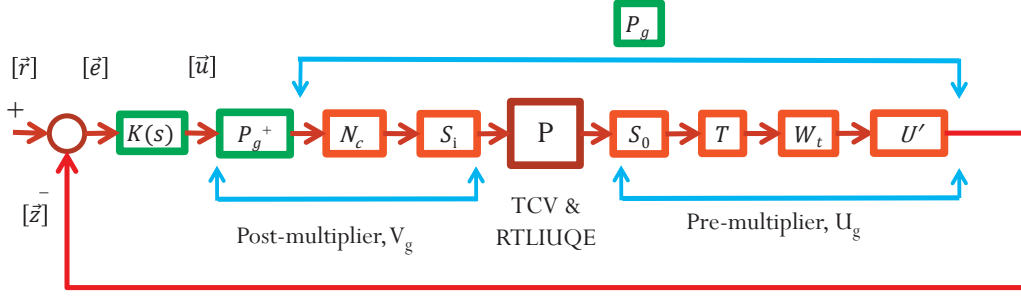


Figure 3.3 – Schematic block diagram for the generalised plasma position and shape controller.

the weighting matrix is determined such that it promotes the plasma estimator in the set of $n_c - 1$ singular values. The controller for the original plant P is thus represented by $C_p(s)$ defined in (3.5), such $\delta \vec{I}_{PF}(kA) = C_p(s)\vec{e}$ with inputs as the errors \vec{e} on the controlled variables and outputs as the poloidal field coil currents $\delta \vec{I}_{PF}$ in kAs. Figure 3.3 shows the schematic block diagram of the generalised plasma position and shape controller. In reality the plant P would represent the TCV tokamak and RTLIUQE and the controller formulation would include a pre multiplier matrix $U_g = U^T W_t T S_o, U_g \in \mathbb{R}^{n_c-1 \times n_y}$ and a post multiplier matrix $V_g = S_i N_c P_g^+, V_g \in \mathbb{R}^{n_c \times n_c-1}$: the latter translates the RTLIUQE outputs to controlled variables, \vec{z} , while the former provides the coil directions for controlling the controlled variables. The reference signals are defined as zeros. The error signals are fed to a proportional and integral controller $K(s)$ defined by (3.1).

$$C_p(s) = S_i N_c P_g^+ K(s) \quad (3.5)$$

3.2.2 Time varying controller design

The controller designed above is only applicable to plasma scenarios involving a plasma shape and position that remain fixed during the discharge. The next step is to tackle time-varying configurations. The chosen approach is to construct individual controllers for the equilibria pre-defined by the shot design sequence. These are, however, sampled at a smaller time step than the original sample times. A linear interpolation in time is performed between the control points defined by various equilibria during the shot design phase. The sample time of the linear interpolation is usually chosen as 10 ms. The individual controllers with respect to each of the interpolated equilibria at smaller time steps are then determined using (3.5). Measures are taken such that the output of the currently active controller $C_p^i(s)$ switches to the output of the subsequent controller $C_p^{i+1}(s)$ smoothly ensuring a continuous transition between the controllers throughout the plasma discharge, where i represents the index of the controller.

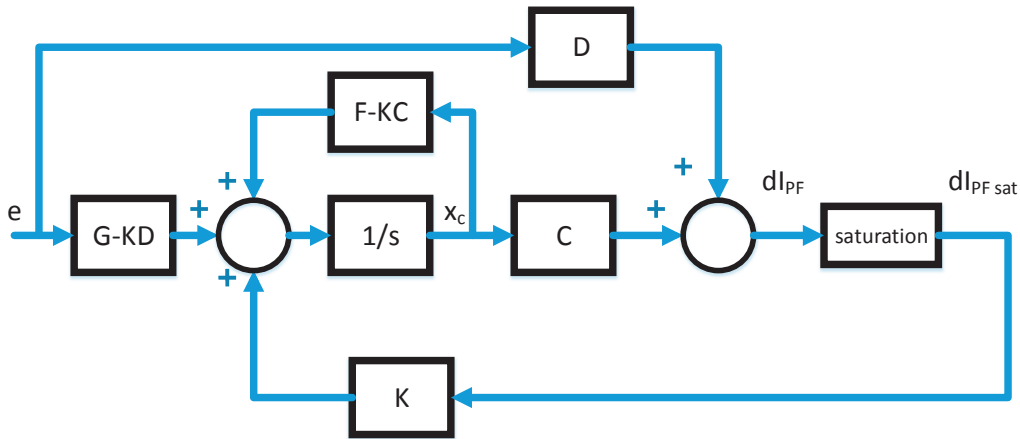


Figure 3.4 – Block diagram of the controller showing the modification to avoid anti windup.

The output of the controller, U_k , at the switching sample k_s is defined as:

$$U_k = u_k^{i+1} + (u_{k_s-1}^i - u_{k_s-1}^{i+1})F(k - k_s) \quad (3.6)$$

where the indexes i and $i + 1$ denote the latter and former controllers, $F(k - k_s) = e^{-(k-k_s)\tau}$ is a decaying exponential function, τ determines the time constant of bumpless transfer.

3.2.3 Anti windup and bumpless transfer

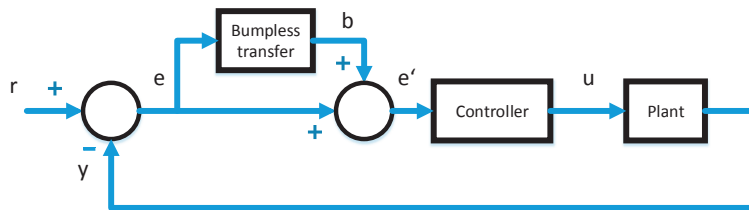


Figure 3.5 – Block diagram of the controller showing the bumpless transfer implementation.

Any saturation in the poloidal field coil currents results in a mismatch between the controller output and the system input. Thus, the feedback loop is broken, since changes in the controller output no longer affect the system. (In reality, the violation of any of the above-mentioned limits causes an immediate termination of the pulse rather than a saturation, but this does not affect the formalism discussed here.) Saturations can cause the integrator that is included in the controller to accumulate as it will continue to integrate a tracking error and produce

3.2. Plasma position and shape controller design.

increasing control signals which, due to the saturation, do not affect the plant output. The state and the control signal can continue to evolve, although the influence on the process is restricted because of saturation. The space representation of the controller $C_p(s)$ is given as

$$\begin{aligned}\dot{\vec{x}}_c &= F\vec{x}_c + G\vec{e} \\ \delta\vec{I}_{PF} &= C\vec{x}_c + D\vec{e}\end{aligned}\quad (3.7)$$

where x_c represents the state and F , G , C and D are the state space matrices, \vec{e} and $\delta\vec{I}_{PF}$ are the input and output of the controller.

A general state space controller can be formulated which avoids the windup problem; in this case, the control law is rewritten as indicated in figure 3.4. This can be expressed as follows:

$$\begin{aligned}\dot{\vec{x}}_c &= F\vec{x}_c + G\vec{e} + K(\delta\vec{I}_{PFsat} - C\vec{x}_c - D\vec{e}) \\ &= (F - KC)\vec{x}_c + (G - KD)\vec{e} + K\delta\vec{I}_{PF} \\ &= F_0\vec{x}_c + G_0\vec{e} + K\delta\vec{I}_{PFsat}\end{aligned}\quad (3.8)$$

where $F_0 = F - KC$ and $G_0 = G - KD$ and If the system of (3.8) is observable, the matrix K can always be chosen such that F_0 has stable eigenvalues (Aström and Wittenmark, 1997). This ensures that the state assumes a proper value when the controller output saturates and thus prevents the problem of windup. In the case of time varying controller design, not only the individual state space controllers are constructed with respect to each interpolated equilibria sampled at smaller time steps but also the corresponding matrix K is determined that stabilizes the eigenvalues for every F_0 and ensures anti windup design for each of the controllers.

The design of the generalised plasma position and shape controller relies on the TCV hybrid controller for vertical stability, thus only the differential control on the vertical position is retained and the proportional control of the plasma position is provided by the new controller. This discontinuity introduced by the switching between the position control of the TCV hybrid controller to the position control performed by the designed controller is avoided by developing a bumpless transfer mechanism shown in figure 3.5. Through the addition of a modification b to the error on each controller variable e ,

$$e' = e + b \quad (3.9)$$

where e' is the modified error to the controller. The modification b , providing a smooth transition between subsequent controllers, is defined as follows:

$$b = \begin{cases} -e & \forall t < t_s \\ e_{t_s}(L(s) - I) & \forall t \geq t_s \end{cases} \quad (3.10)$$

Chapter 3. Generalised plasma position and shape controller design

where e_{t_s} is the error between the controllers at the switching time t_s and $L(s)$ is a first order filter in the Laplace domain s , with time constant τ ,

$$L(s) = \frac{1}{\tau s + 1} \quad (3.11)$$

The formalism defined by (3.9) ensures that, before the activation, the controller artificially witnesses a zero error and tends smoothly to the active error according to the chosen time constant defined by (3.11).

3.2.4 Implementation with the TCV hybrid controller

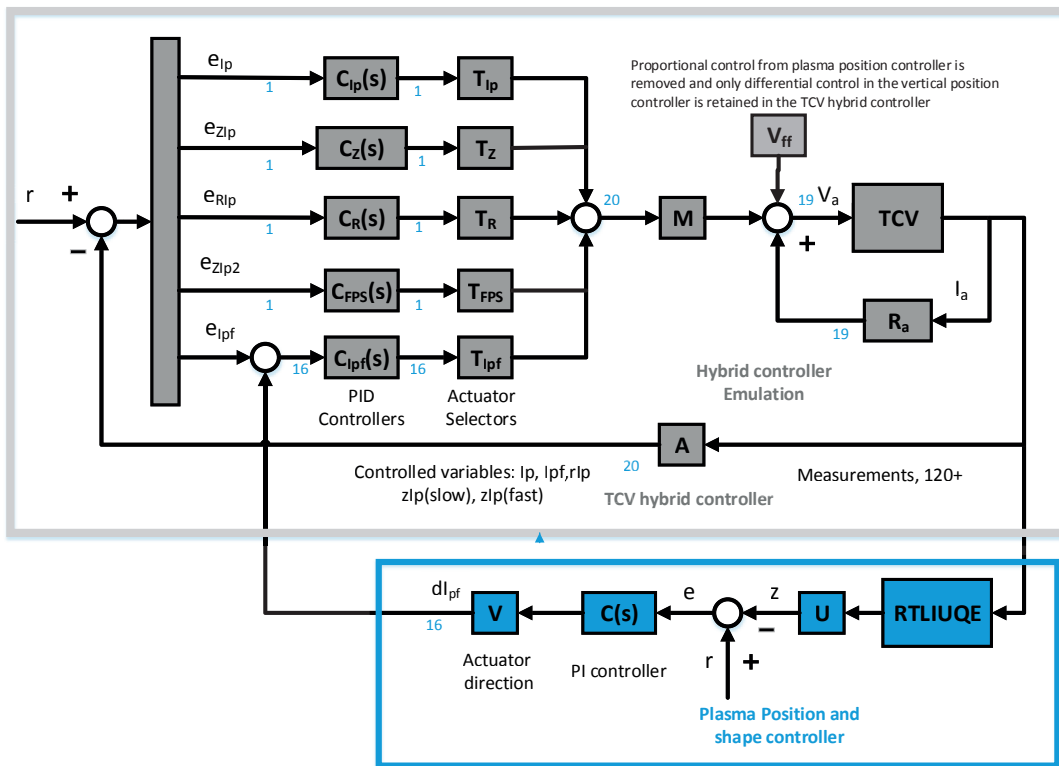


Figure 3.6 – Block diagram showing the implementation of the generalised plasma position and shape controller with the TCV hybrid controller.

Figure 3.6 shows a block diagram representation of the TCV hybrid controller with the generalised plasma position and shape controller. The simplified scheme of the TCV hybrid controller is shown in the grey box of figure 3.6. The measurements (magnetic flux loops, magnetic probes, FIR laser interferometer fringe counter, active coil current measurements, \vec{I}_a) from the TCV tokamak are processed by the A matrix, generating controlled variables, as linear combinations of the inputs signals. The set of controlled variables consists of the plasma current I_p , the poloidal field coil currents I_{pf} , the vertical position estimator zI_p and the radial

3.2. Plasma position and shape controller design.

position estimator. The controlled variables are then subtracted from the reference signals to yield the respective error signals. The error signals are fed to their respective controllers and actuators: $C_{Ip}(s)$ represents a proportional and integral controller and T_{Ip} selects the ohmic coils as an actuator for controlling the plasma current; $C_Z(s)$ represents a proportional and differential controller and T_Z selects a combination of the F poloidal field coils to control the plasma vertical position; $C_R(s)$ is a proportional controller and T_R selects a combination of the F poloidal field coils to control the radial position of the plasma; $C_{FPS}(s)$ is a differential controller and T_{FPS} selects the internal G coils to control the plasma vertical instability; $C_{Ipf}(s)$ is a proportional controller and T_{Ipf} selects the combination of poloidal field coils orthogonal to the coil combination providing vertical and radial control. The actuator control signals are then passed through the M matrix which is constructed with mutual inductance coefficients, i.e., performs the decoupling of the mutual inductances. The resistive compensation ($R_a \vec{I}_a$) and the feedforward voltages V_{ff} are added to the outputs of the M matrix to generate the input voltages V_a for the actuators.

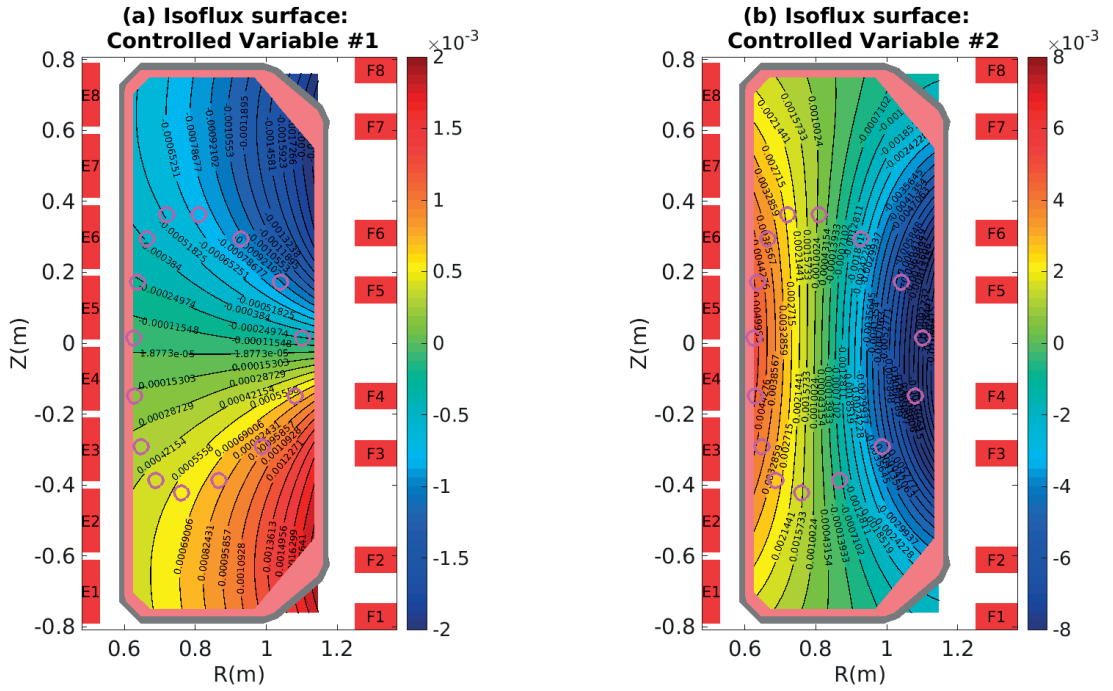


Figure 3.7 – Isoflux surfaces generated by the poloidal field coils $E1 - E8$ and $F1 - F8$ for a limiter plasma configuration for controlling the (a) first and (b) second controlled variable. The plasma boundary is denoted by the magenta circles.

The implementation of the generalised plasma position and shape controller with the TCV hybrid controller is shown in the blue box of figure 3.6 (Anand et al., 2016). The controller algorithm resides on the same real-time node as the TCV hybrid controller and functions on a cycle time of 0.1 ms. The controller formalism defined in the section 3.2 relies on the legacy analogue TCV hybrid controller for stabilizing the vertical position of the plasma (Hofmann and Jardin, 1990), that is only the differential control in the vertical control loop remains

Chapter 3. Generalised plasma position and shape controller design

in the TCV hybrid controller. To ensure a reliable radial and vertical position control of the plasma, an appropriate weighting is applied on the position estimators in the generalised plasma position and shape controller such that the control of the first two controlled variables corresponds to plasma position control. Thus, the controller formulation allows to use the plasma position estimators derived directly from the solution of the Grad-Shafranov equation for controlling the plasma position, unlike in the case of the TCV hybrid controller where the plasma position estimators are linear combinations of magnetic measurements only. The isoflux surfaces generated by the poloidal field coil directions corresponding to the first two controlled variable controlling the vertical and the radial plasma position, are shown in figure 3.7. The RTLIUQE provides the poloidal flux and the poloidal magnetic field at the control points. The pre-multiplier matrix U_g converts the RTLIUQE outputs to the controlled variables. The output of the post multiplier matrix V_g denotes the poloidal field coil currents requested by the controller. The requested poloidal field coil currents are added to the poloidal field coil current controller loop of the TCV hybrid controller. The poloidal field coil current controller loop fulfils the requested coil currents demanded by the new controller to have the desired control on the controlled variables.

3.3 Plasma Modelling

The verification of the controller performance and optimisation of the control parameters (proportional K_{ps} and integral gains K_{is} , weight matrix W_t and number of actively controlled variables \vec{z}) for the generalised plasma position and shape controller is performed with the help of a linearised plasma response model, the RZIP model (Coutlis et al., 1999). The RZIP model is also used to study the coupling between TCV hybrid controller and new controller. The model is constructed with physical laws and simplifying assumptions. A set of circuit equations is developed, based on the supposition that the plasma current distribution remains constant during any control action, but that its centroid can move vertically and radially and its integral, the total plasma current, can change. The plasma model is based on the linearisation assumption that small variations in the poloidal field coil voltages lead to small changes in the plasma current, poloidal field currents, vacuum vessel currents and plasma radial and vertical positions, about a given unperturbed equilibrium state.

The set of equations composing the model comprises the circuit equations for the poloidal field coils, the vessel currents and the plasma, in addition to the plasma radial and vertical force balance equations. All spatially dependent quantities are evaluated using the plasma current distribution derived by the LIUQE equilibrium code,

$$\langle A \rangle = \frac{\sum_i A(R_i, Z_i) J_\phi(R_i, Z_i)}{\sum_i J_\phi(R_i, Z_i)} \quad (3.12)$$

where A is any parameter of interest.

The circuit model representation of the structures (active and passive conductors) takes the

following form:

$$\vec{V}_a = M_{aa}\vec{I}_a + M_{av}\vec{I}_v + R_a\vec{I}_a + \frac{d}{dt}(M_{ap}I_p) \quad (3.13)$$

$$0 = M_{vv}\vec{I}_v + M_{va}\vec{I}_a + R_v\vec{I}_v + \frac{d}{dt}(M_{vp}I_p) \quad (3.14)$$

where M denotes a mutual inductance matrix, with indexes a , v , and p referring to "active conductor", "vessel" (passive conductor), and "plasma", respectively. R_a and R_v are the active and passive conductor resistance matrices, \vec{I}_a and \vec{I}_v are the vectors of currents in active and passive conductors, I_p is the plasma current and \vec{V}_a is the vector of voltages for active conductor.

The plasma current dynamic response is governed by a similar circuit equation, which treats the plasma as a single circuit consisting of a distributed array of conducting elements. The plasma response equation can be written in the form

$$0 = \frac{d}{dt}(M_{pa}\vec{I}_a) + \frac{d}{dt}(M_{pv}\vec{I}_v) + \frac{d}{dt}(L_p I_p) + R_p I_p \quad (3.15)$$

where L_p is the plasma self-inductance and R_p the plasma resistance matrix.

Next we tackle the time derivatives of the radial and vertical force balance equations, neglecting the plasma inertia. The radial force balance consists of two components: the Lorentz force acting on the plasma due to the vertical magnetic field and the hoop force generated by the plasma pressure in toroidal geometry.

$$\frac{d}{dt} \left(m_p \frac{d^2 R}{dt^2} \right) = \frac{d}{dt} \left(\frac{\mu_o I_p^2}{2} \Gamma + 2\pi R I_p B_z \right) = 0 \quad (3.16)$$

$$\frac{d}{dt} \left(m_p \frac{d^2 Z}{dt^2} \right) = \frac{d}{dt} (-2\pi R I_p B_r) = 0 \quad (3.17)$$

where m_p is the inertia of the plasma, R and Z represent the radial and vertical positions of the current centroid, B_r and B_z are the radial and vertical magnetic fields produced by the conductors, Γ is a function of the plasma self inductance, l_i , and plasma beta, β_p .

Linearisation of the set of equations around an equilibrium point, $\vec{I}_a = \vec{I}_{ao}(t) + \delta\vec{I}_a$, $\vec{I}_v = \vec{I}_{vo}(t) + \delta\vec{I}_v$, $I_p = I_{po}(t) + \delta I_p$, $\vec{V}_a = \vec{V}_{a0} + \delta\vec{V}_a$, $R = R_o + \delta R$, $Z = Z_o + \delta Z$ and $\Gamma = \Gamma_o(t) + \delta\Gamma$, and

Chapter 3. Generalised plasma position and shape controller design

defining M , R , $\vec{x}(t)$ and $\vec{u}(t)$ as follows,

$$M = \begin{pmatrix} M_{aa} & M_{av} & M_{apo} & \frac{\partial M_{ap}}{\partial R} & \frac{\partial M_{ap}}{\partial Z} \\ M_{va} & M_{vv} & M_{vp_o} & \frac{\partial M_{vp}}{\partial R} & \frac{\partial M_{vp}}{\partial Z} \\ M_{pa_o} & M_{pv_o} & L_{p_o} & M_{pR} & 0 \\ \frac{\partial M_{pa}}{\partial R} & \frac{\partial M_{pv}}{\partial R} & M_{Rp} & M_{RR} & M_{RZ} \\ \frac{\partial M_{pa}}{\partial Z} & \frac{\partial M_{pv}}{\partial Z} & 0 & M_{ZR} & M_{ZZ} \end{pmatrix}, R = \begin{pmatrix} R_a & 0 & 0 & 0 & 0 \\ 0 & R_{vv} & 0 & 0 & 0 \\ 0 & 0 & R_{p_o} & R_{pR} & 0 \\ R_{Ra} & R_{Rv} & R_{Rp} & R_{RR} & 0 \\ R_{Za} & R_{Zv} & 0 & 0 & 0 \end{pmatrix}, \quad (3.18)$$

$$\vec{x}(t) = \begin{pmatrix} \delta I_a \\ \delta I_v \\ \delta I_p \\ I_{p_o} \delta R \\ I_{p_o} \delta Z \end{pmatrix}, \vec{u}(t) = \begin{pmatrix} V_a \\ 0 \\ 0 \\ S_R \\ 0 \end{pmatrix}$$

where elements of the matrices M and R are defined in the appendix A.1.

The complete dynamic system including the conductors and plasma can be expressed in the state space form with \vec{u} as inputs and \vec{y} as outputs of the system

$$\begin{aligned} \dot{\vec{x}} &= A\vec{x} + B\vec{u} \\ \vec{y} &= C\vec{x} + D\vec{u} \end{aligned} \quad (3.19)$$

where the first equation is called the state equation with $A = -M^{-1}R$ and $B = M^{-1}$, respectively, and the second equation is called the output equation. The only positive eigenvalue of matrix A is the plasma vertical displacement event growth rate which is a specific characteristic of the plasma's vertical speed of response. For typical discharge shapes of TCV, the vertical growth rate is about $200 - 300 \text{ s}^{-1}$. \vec{y} represent a vector of the measurements consisting of the radial rI_p and vertical zI_p estimators of the TCV hybrid controller and the controlled variables \vec{z} of the generalised plasma position and shape controller. C is a matrix relating the measurement to the states of the system and D is a direct feedthrough matrix denoting the sensitivity of the measurements to the inputs and are represented as follows

$$C = \begin{pmatrix} C_{rI_p} \\ C_{zI_p} \\ C_z \end{pmatrix}, D = 0 \quad (3.20)$$

The matrices C_{rI_p} and C_{zI_p} converts the states to plasma position estimators of the TCV hybrid controller and matrix C_z converts the states into the controlled variables of the generalised plasma position and shape controller.

The loop for the reconstructed radial, rI_p and vertical, zI_p position estimators from the RZIP plasma model is closed with the position controller from the TCV hybrid controller described

in section 3.2.4. A stable closed loop step response is shown in figure 3.8(a) for the vertical position estimator for the TCV tokamak for a given proportional K_p and differential control K_d gains in the TCV hybrid controller.

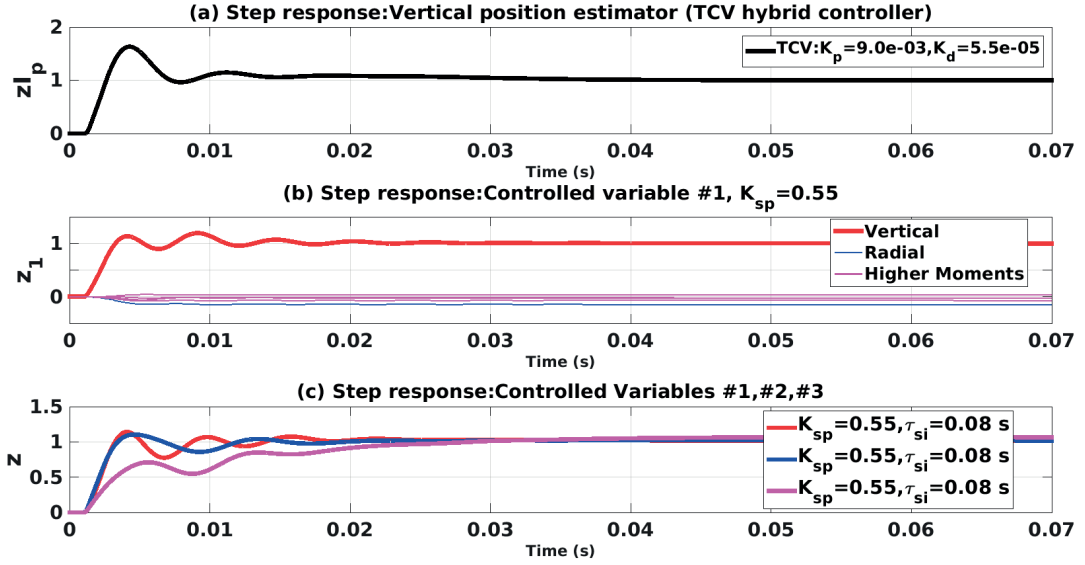


Figure 3.8 – Linearised plasma modelling simulation results for the TCV tokamak. (a) Step response of the vertical estimator for the TCV hybrid controller and (b) step response of the first controlled variable and its effect on the higher order controlled variables for the generalised plasma position and shape controller. (c) Step response of the controlled variables controlling the plasma position and shape.

A stable response with respect to a step reference on the first controlled variable of the generalised plasma position and shape controller derived from the RZIP plasma model is shown in figure 3.8(b) with only a proportional gain K_{sp} . For a given plasma current distribution and set of controller gains, the ratio between the open loop gain for the generalised plasma position and shape controller and that for the position controller within the TCV hybrid controller from the simulation is found to be 1.5. Thus, for the given case, the simulation predicts the use of either a lower differential or a lower proportional gain within generalised plasma position and shape controller in order to have a comparable response. In general, the modelling predicts that the differential gain in the TCV hybrid controller or the gains of the new controller are to be modified in order to obtain an adequate performance.

The RZIP simulation not only predicts the fact that a simple proportional control on the first controlled variable related to the vertical position of the plasma can provide a suitable controller performance, but also shows the coupling among the controlled variables in steady state. For the case of the static generalised plasma model P_g defined in section 3.2.1, since the compensator design is provided directly by the pseudo-inverse of the generalised plant P_g^+ , a perfect decoupling is guaranteed among the controlled variables. Figure 3.8(b) shows finite steady state offsets in the response of the remaining controlled variables with respect to a step

reference on the first controlled variable. A comparison between the step response on the first two controlled variables (related to the plasma position control) and a higher order controlled variable (related to the control of the plasma shape) for a fixed proportional K_{sp} and integral gain $K_{si} = 1/\tau_{si}$ is shown in figure 3.8(c). A slower dynamical response of the higher order controlled variable in comparison to the first two is observed for a fixed proportional and integral gain on the controlled variables, pointing towards higher gains on the the higher order controlled variables to improve the tracking performance of the plasma shape.

3.4 Experimental results

Dedicated experiments have been performed to test the generalised plasma position and shape controller during the TCV campaign in 2016-2017. The analysis of the experimental results is divided into two main sections, with each section comprising of application of the controller design on plasma scenarios including fixed as well as time varying plasma position and shape.

3.4.1 Limiter plasma configuration

Plasma configuration with fixed plasma shape and position

Limiter plasma discharges (54105 and 54111) involving fixed plasma position and shape in time were chosen to test the controller formalism with the aim of exploring the range of proportional and integral gain for controlling the plasma position. In the discharge 54105, the proportional gain of the first two controlled variable representing the control of the plasma position was scanned while setting the integral gain for all controlled variables to 0. Similarly, in the discharge 54111, the integral gain on the first two controlled variables was scanned with a fixed proportional gain in the controller.

Figure 3.9 illustrates the range of control parameters, i.e. proportional and integral gains, that provide stability in conjunction with the differential vertical controller of the TCV hybrid controller. Figures 3.9(a) and 3.9(b) show a median range of consistent proportional (0.55-0.85) and integral gains (0.02-0.2s) for a given limiter plasma configuration. Insufficient gains are usually identified experimentally by loss of control, excessive gains by oscillatory behaviour. (figures 3.9(c) and 3.9(d)). Figures 3.9(e) and 3.9(f) show the associated vertical position reference and measurement for the given discharges.

For validating the feature of the controller design of limiting the controlled variables to the set that is most easily controlled, while respecting the hardware limits on the poloidal field coil currents, a series of limiter plasma discharges with fixed plasma shape and position were performed for a given set of controller gains ($K_{sp} = 0.55, \tau_{si} = 0.2s$), every successive discharge including a larger set of actively controlled variables \vec{z} . Figure 3.10 explores the effective number of active controlled variables that are required to provide a suitable control of plasma

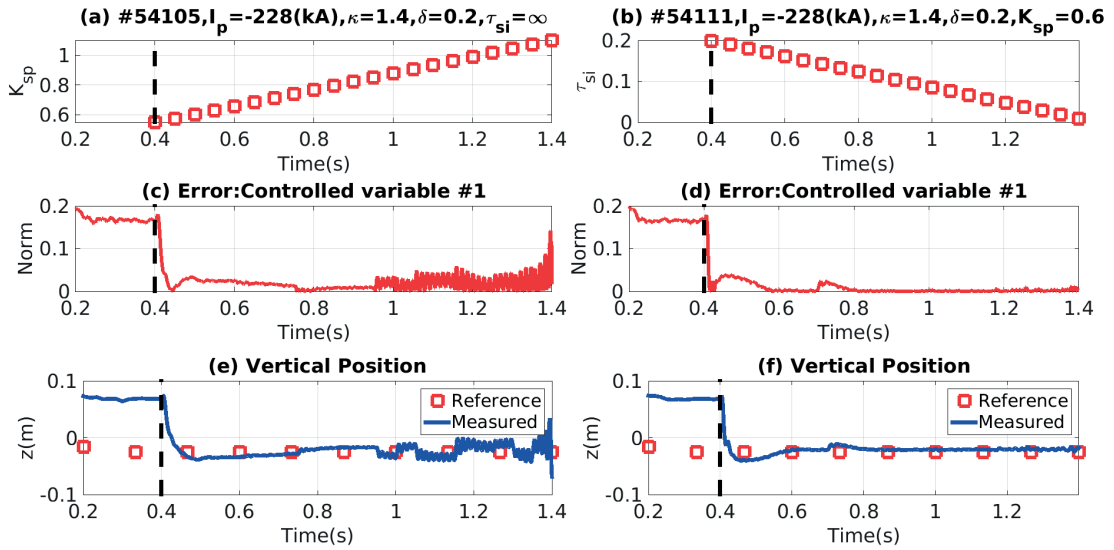


Figure 3.9 – Investigation of the effect of proportional and integral gains on the performance of the generalised plasma position and shape controller. (a) Proportional gain scan without integral gain and (b) integral gain scan with a fixed proportional gain for a limiter plasma configuration with fixed plasma shape and position. (c) and (d) Time evolution of the norm of the error on the first controlled variable related to the plasma vertical position. (e) and (f) Reference and the measurement of the vertical position of the plasma magnetic axis obtained from RTLIUQE. δ and κ represents the reference of the plasma triangularity and elongation from FBTE.

position and shape while limiting the demand on the poloidal field coil currents. Figures 3.10(c) and 3.10(d) show the norm of the normalised poloidal field coil currents requested by the controller and the norm of the errors on the full set of controlled variables as functions of the number of actively controlled variables. These plots demonstrate that controlling a subset (with high singular values) of variables is sufficient to provide satisfactory shape and position control, and conversely that there is little to gain in adding control channels that have small singular values - rather, this increases the danger that coil current limits are violated. Figure 3.11 shows the evolution of the magnitude of the singular values associated with each of the controlled variables for the limiter plasma discharge. The sharp decrease in the magnitude of the singular values implies that it is sufficient to control only a smaller subset of the controlled variables (8 in this case) corresponding to the dominant singular values. Figures 3.10(a) and 3.10(b) show the contour plots of the poloidal flux distribution and the last closed flux surface (LCFS), with the control points defining the plasma boundary, at time instants before and after the controller activation for the discharge 51437 with 8 actively controlled variables and fixed set of controller gains ($K_{sp} = 0.55, \tau_{si} = 0.2s$). They illustrate the enhancement in the plasma position and shape in comparison to the TCV hybrid controller for a given set of optimised control parameters and a fixed number of actively controlled variables.

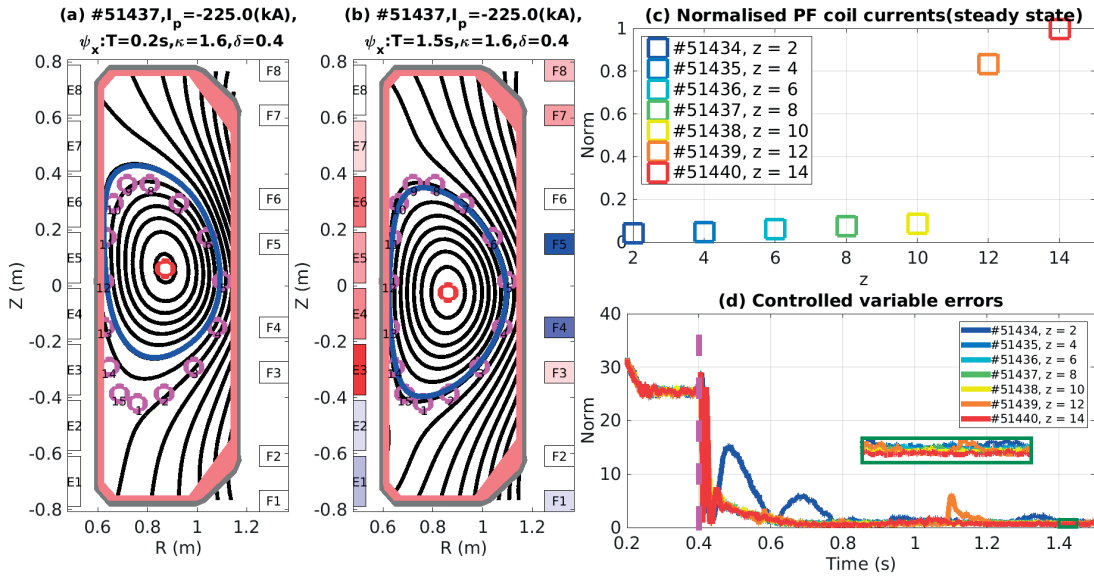


Figure 3.10 – Investigation of optimum number of actively controlled variables for plasma position and shape control for a limiter plasma configuration with a fixed set of controller gains ($K_{sp} = 0.55, \tau_{si} = 0.2$ s). (a) Poloidal flux map (black lines) ψ_x and (b) last closed flux surface (blue line) obtained from RTLIUQE before and after the controller activation with an optimum number of active controlled variables (8). (c) Norm of the normalised poloidal field coil currents requested by the controller at steady state and (d) norm of the error of all the controlled variables with time as a function of the actively controlled variables. The pre-programmed control points are given by the magenta circles. δ and κ represents the reference of the plasma triangularity and elongation from FBTE.

Plasma configuration with varying plasma shape and position

Two limiter plasma discharges were performed, one containing a scan of the plasma vertical position, followed by a scan in the plasma elongation (55141) and the other including a scan from negative to positive plasma triangularity (55144) to test the performance of the time varying version of the controller design with an optimised number of actively controlled variables (8) and controller gains (position ($K_{sp} = 0.55$ and $\tau_{si} = 0.1$ s) and shape control ($K_{sp} = 0.3$ and $\tau_{si} = 0.01$ s)).

Figure 3.12 shows the application of the controller to the complex plasma scenario involving sweeps of plasma position and elongation. The norm of the errors on the active controlled variables (figures 3.12(c)) are reduced rapidly at the time of the controller activation and are then kept close to zero, providing a satisfactory tracking of the plasma position (3.12(d)) and shape variables (elongation (figure 3.12(e)) and triangularity (figures 3.12(f))). A poor tracking of the plasma triangularity is obtained after 1.3 s, even though the norms of the errors on actively controlled variables are low. This could be linked to the non-existence of the controlled variable representing the control of plasma triangularity in the set of actively controlled variable. Figure 3.13 shows the evolution of the last closed flux surface at various

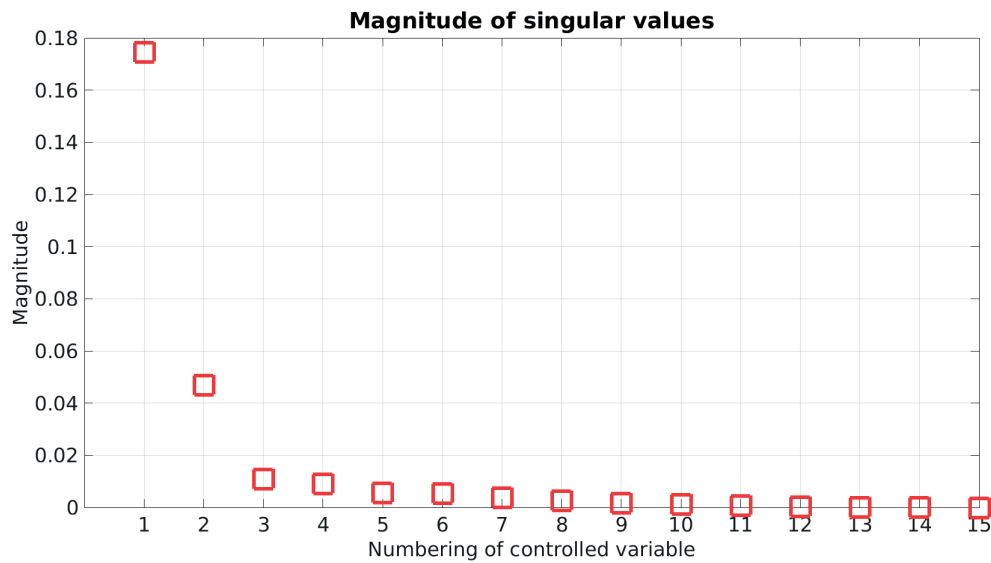


Figure 3.11 – Evolution of the magnitude of the singular values with respect to each controlled variable for the limiter plasma configuration.

time instances during the discharge.

Figure 3.14 shows the application of the controller to a scenario involving a scan of the plasma triangularity from a negative to a positive value. Upon controller activation, the norm of the errors on the actively controlled variables is reduced and adequate tracking of not only the plasma triangularity (figure 3.14(f)) but also of the plasma vertical position (figure 3.14(d)) and elongation (figure 3.14(e)) is obtained. The time evolution of the last closed flux surface during the discharge is shown in figure 3.15.

The perturbations observed in the norm (figures 3.12(c) and 3.14(c)) of the errors on the controlled variables are induced by step changes in the poloidal field coil currents resulting from a change in polarity or from switching of the controller algorithm to control a new equilibrium. However, the designed controller rejects the disturbances and forces the controlled variables to track the desired reference.

3.4.2 Divertor plasma configuration

Plasma configuration with fixed plasma shape and position

After successfully testing the controller design for fixed and time varying plasma position and shape for the limiter plasma configuration, the controller design was extended to divertor plasma configurations. Similar to the previously discussed procedure, a divertor discharge with fixed plasma shape and position was performed (55725). Figure 3.16 shows the successful application of the controller to a time invariant divertor plasma configuration with an optimised set of controlled variables (8) controlling simultaneously not only the plasma shape and

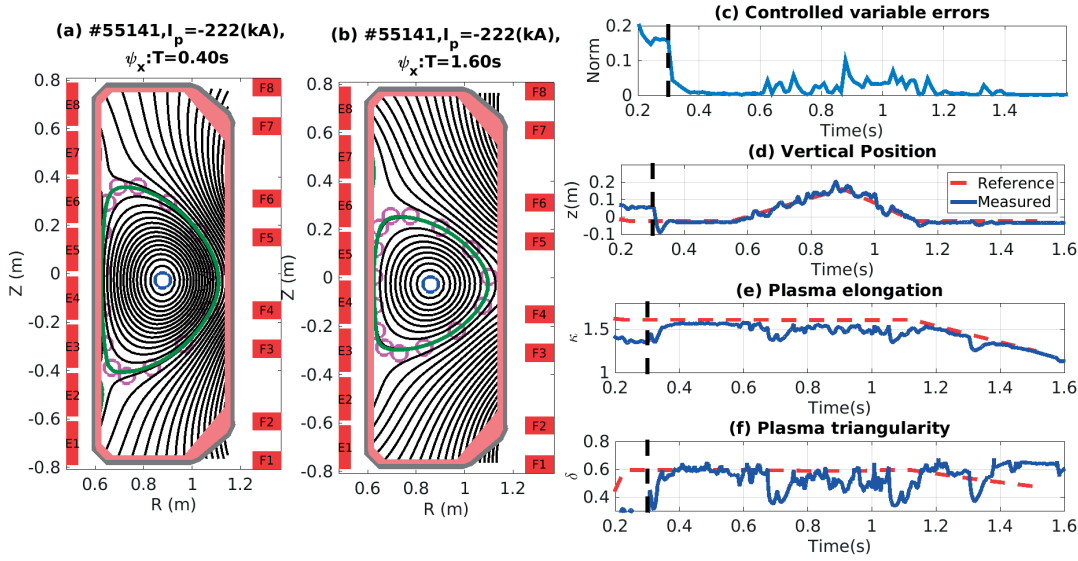


Figure 3.12 – Performance of the generalised plasma position and shape controller for limiter plasma configuration involving a scan of plasma vertical position and elongation with 8 actively controlled variables and fixed controller gains for position ($K_{sp} = 0.55$ and $\tau_{si} = 0.1s$) and shape control ($K_{sp} = 0.3$ and $\tau_{si} = 0.01s$). (a) Poloidal flux contour ψ_x (black lines) and (b) the last closed flux surface (green line) at different time instants of the controller operation obtained from RTLIUQE. (c) Time evolution of norm of the errors of the actively controlled variables. Reference and measurement of the plasma vertical position (d), elongation (e) and triangularity (f) obtained from FBTE and LIUQE. The pre-programmed plasma boundary is given by control points in magenta circles.

position but also the position of the divertor leg and the poloidal magnetic field at the X-point. The contour plots before and after the controller activation are shown in figures 3.16(a) and 3.16(b). Again, the controller activation results in the reduction of the norm of the errors on the actively controlled variable (figure 3.16(c)), and excellent and smooth tracking is achieved as shown by a comparison of the references with the measurements of the plasma position and shape variables, as shown in figure 3.16(d) and figures 3.16(e-f).

Plasma configuration with varying plasma shape and position

A complex divertor plasma discharge to test the time varying version of the algorithm in a divertor configuration was performed (55147) including sweeps in both the plasma and shape variables. Figure 3.17 illustrates the universality and flexibility of the controller using a divertor plasma configuration involving complex and simultaneous changes in the plasma position and shape during the plasma discharge. Figure 3.17 (c) shows the norm of the errors on the 8 actively controlled variables. The tracking performance of the controller with respect to the plasma position and shape variables is shown in figures 3.17(d) and 3.17(e-f). Figure 3.18 shows the evolution of the separatrix at various time instances for the plasma discharge.

3.4. Experimental results

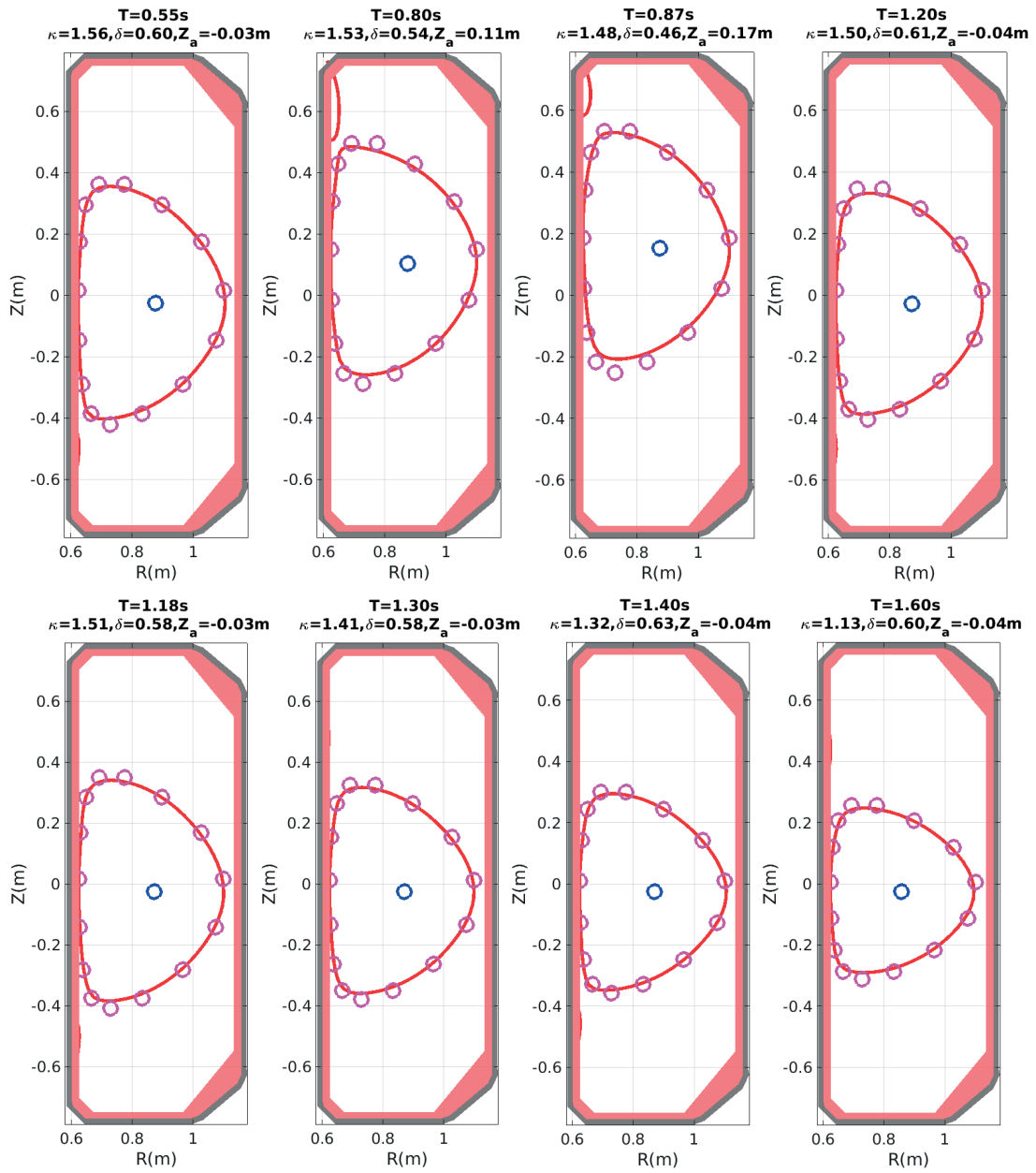


Figure 3.13 – Last closed flux surface (red line) and vertical position Z_a of the plasma magnetic axis (blue circle) obtained from RTLIUQE for the plasma discharge 55141, at various time instances. κ and δ represent the plasma elongation and triangularity obtained from LIUQE. The pre-programmed plasma boundary is denoted by magenta circles.

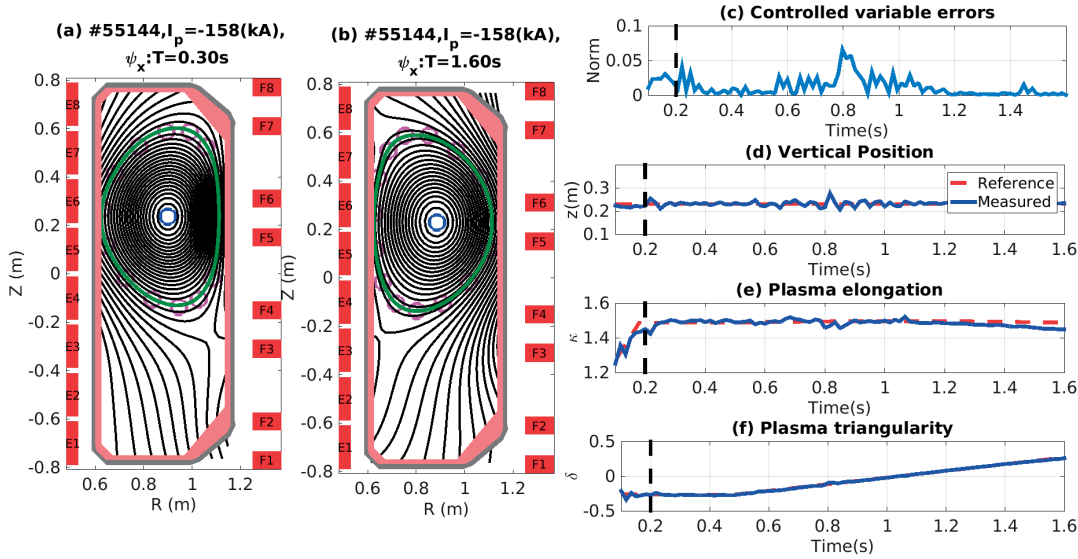


Figure 3.14 – Performance of the generalised plasma position and shape controller for a limiter plasma configuration involving a scan of the plasma triangularity with 8 actively controlled variables and fixed controller gains for position ($K_{sp} = 0.55$ and $\tau_{si} = 0.1s$) and shape control ($K_{sp} = 0.3$ and $\tau_{si} = 0.01s$). (a) Poloidal flux contour ψ_x (black lines) and (b) last closed flux surface (green line) at different time instants of the controller operation, obtained from RTLIUQE. (c) Time evolution of norm of the errors of the actively controlled variables. Reference and measurement of the plasma vertical position (d), elongation (e) and triangularity (f) obtained from FBTE and LIUQE. The pre-programmed plasma boundary is given by control points in magenta circles.

3.5 Summary and conclusions

A generalised plasma position and shape control algorithm, developed particularly for advanced plasma configurations, has been presented in this chapter. A linearised plasma model (RZIp), re-derived here in its entirety, is used to study the coupling between the TCV hybrid PID controller and the new generalised plasma position and shape controller. The model is also used to verify the performance of the control algorithm as well as to optimise the control parameters for the controlled variables. However, the control parameters (proportional and integral gains) obtained from RZIp plasma model do not apply to the experiments and manual tuning of the gains are required. A successful experimental implementation of the control algorithm has been demonstrated for both fixed and time varying plasma position and shape for limiter and divertor plasma discharges. The control design exhibits an improved performance with respect to the control of the plasma position and shape relative to the legacy TCV hybrid controller.

The generalised plasma position and shape controller has been successfully tested on various limiter and divertor plasma discharges involving complex changes in the position as well as and shape during the discharge. A suitable range of controller gains has been experimentally

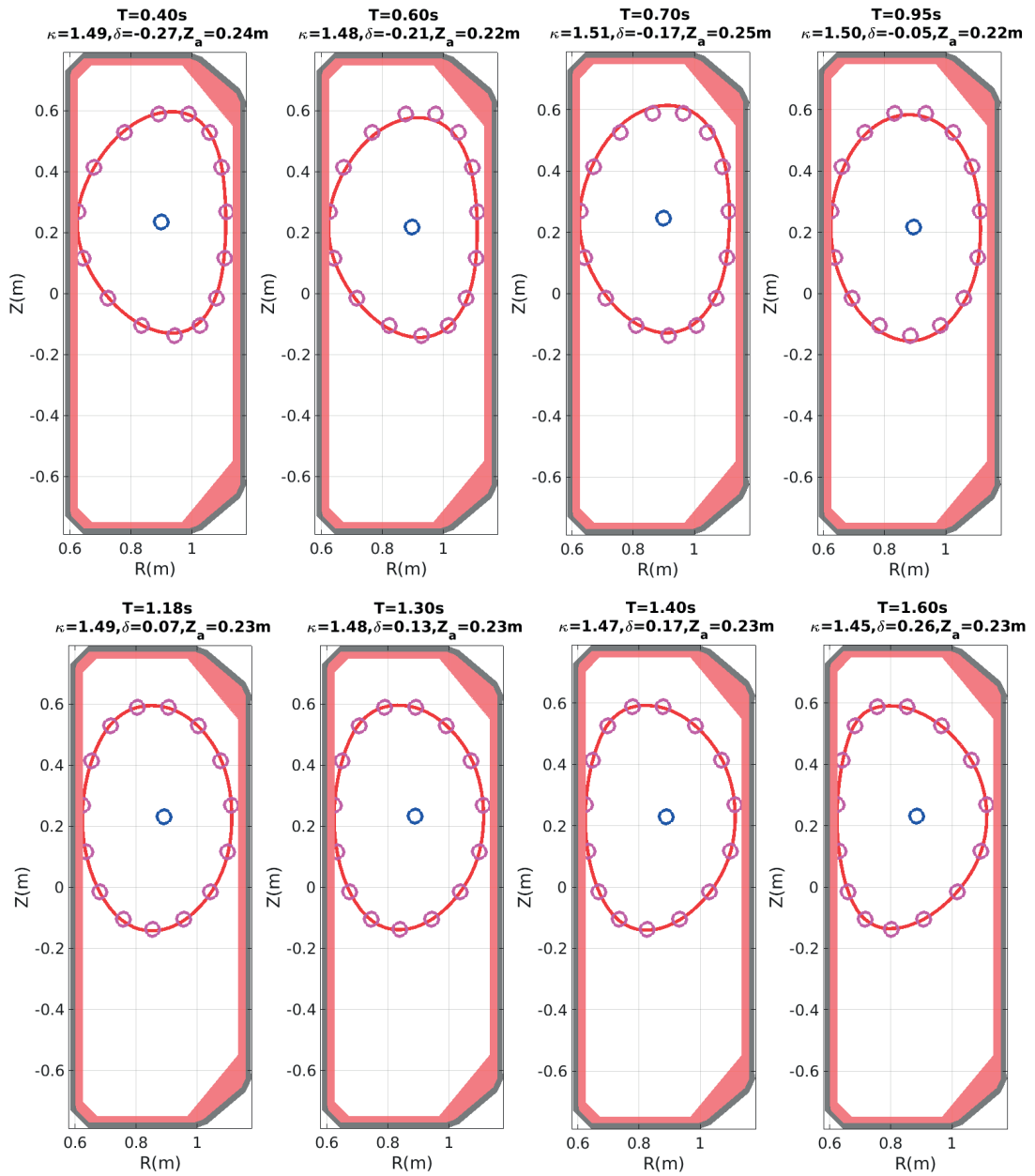


Figure 3.15 – Last closed flux surface (red line) and vertical position Z_a of the plasma magnetic axis (blue circle) obtained from RTLIUQE for the plasma discharge 55144, at various time instances. κ and δ represent the plasma elongation and triangularity obtained from LIUQE. The pre-programmed plasma boundary is denoted by magenta circles.

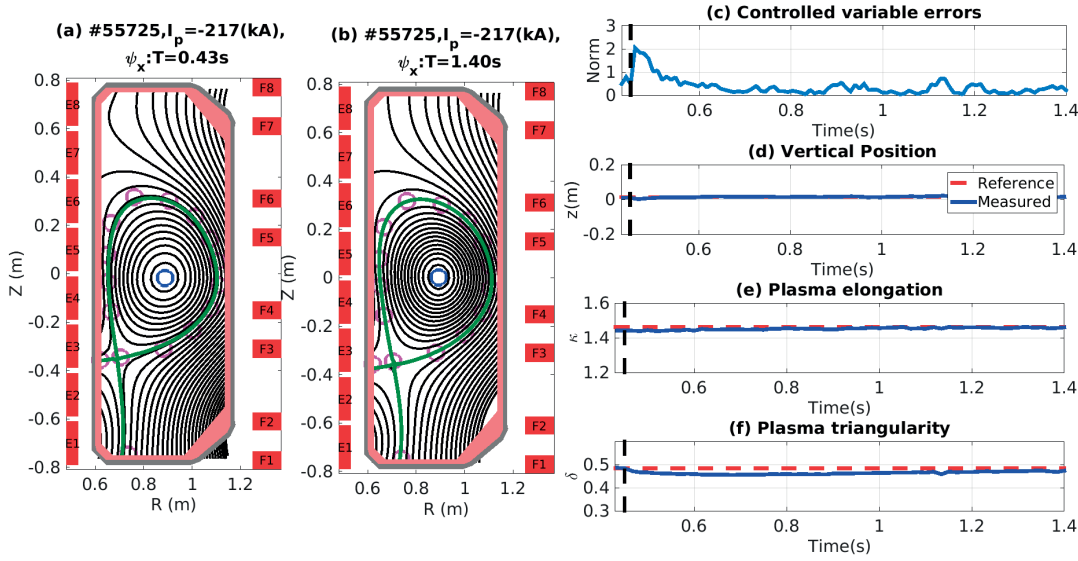


Figure 3.16 – Performance of the generalised plasma position and shape controller for controlling a time invariant divertor plasma configuration with optimised actively controlled variables (8) and controller gains for position ($K_{sp} = 0.55$ and $\tau_{si} = 0.1s$) and shape control ($K_{sp} = 0.85$ and $\tau_{si} = 0.05s$). (a) Poloidal flux contour ψ_x (black lines) and (b) last closed flux surface (green line) at different time instants of the controller operation, obtained from RTLIUQE. (c) Time evolution of norm of the errors of the actively controlled variables. Reference and measurement of the plasma vertical position (d), elongation (e) and triangularity (f) obtained from FBTE and LIUQE. The pre-programmed plasma boundary is given by control points in magenta circles.

found which provides good control of the plasma position without exciting instabilities, particularly the vertical instability. The controller can be optimised in an intuitive fashion, by promoting particular control variables through preferential weighting, while the singular-value decomposition formalism provides natural criteria for optimising the number of controlled parameters. Current limits in the poloidal field coils are respected by anti-windup techniques. A smooth behavior in time is ensured by the bumpless formalism.

In spite of considerable success in developing exotic plasma shapes without active control, future, more advanced developments in TCV, extending beyond the current empirical limits, are likely to depend on reliable shape control. The work described in this chapter aims to be the cornerstone of these developments.

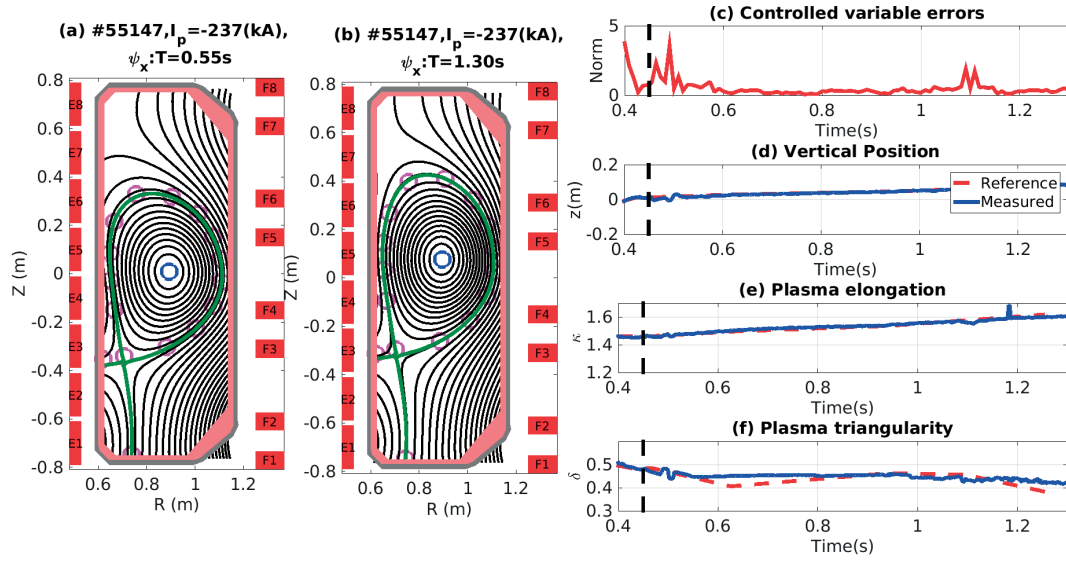


Figure 3.17 – Performance of the generalised plasma position and shape controller for controlling time varying divertor plasma configuration with optimised actively controlled variables (8) and controller gains for position ($K_{sp} = 0.55$ and $\tau_{si} = 0.1s$) and shape control ($K_{sp} = 0.3$ and $\tau_{si} = 0.01s$). (a) Poloidal flux contour ψ_x (black lines) and (b) last closed flux surface (green line) at different time instants of the controller operation, obtained from RTLIUQE. (c) Time evolution of norm of the errors of the actively controlled variables. Reference and measurement of the plasma vertical position (d), elongation (e) and triangularity (f) obtained from FBTE and LIUQE. The pre-programmed plasma boundary is given by control points in magenta circles.

Chapter 3. Generalised plasma position and shape controller design

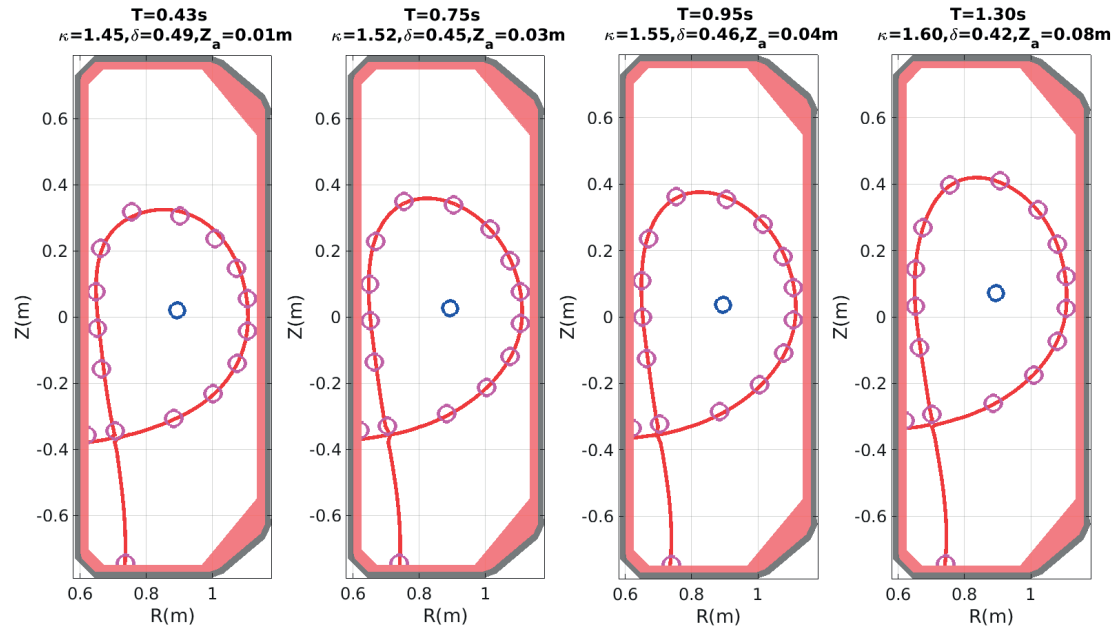


Figure 3.18 – Separatrix (red line) and vertical position Z_a of the plasma magnetic axis (blue circle) obtained from RTLIUQE for the plasma discharge 55725, at various time instances. κ and δ represent the plasma elongation and triangularity obtained from LIUQE. The pre-programmed plasma boundary is denoted by magenta circles.

4 Real time control of snowflake plasma configuration

This chapter discusses the experimental implementation of the plasma position and shape controller for the snowflake plasma configuration on the TCV tokamak. Experimental identification for a given set of optimised control parameters to enhance the performance of the controller is reported. A review with respect to the performance of the controller in comparison to the legacy TCV hybrid controller for a snowflake plasma discharge is discussed. A comparison at the level of the magnetic properties for snowflake plasma and different diagnostic data is examined with respect to the different control systems.

4.1 Introduction

The nested magnetic flux surfaces necessary for plasma confinement are obtained in a tokamak by the combination of fields produced by the external conductors and the plasma itself. The shape of the plasma is defined by the last closed flux surface. This is defined either by the intersection of the closed magnetic surfaces with a solid surface (limited plasma) or by a singularity in the magnetic field itself. The latter geometry, known as divertor configuration, has emerged as the eminent solution for managing power and particle exhaust and core impurity content. At the magnetic X-point, the poloidal field vanishes, and the topology allows energy and particle losses to be channeled primarily into the divertor region that is separated from the confined plasma region. The downside is the high power flux on the divertor plates, which can lead to overheating and destructive erosion. This is especially true during edge localised modes (ELMs) (Prater, 2004; Zohm, 1996; Connor, 1998; Takahashi et al., 2008; Zheng et al., 2008; Wingen et al., 2010) causing periodic, violent, and potentially highly damaging ejections of energy and particles onto the divertor surfaces (Eich et al., 2003; Kirk et al., 2006) which could severely limit the lifetime of the plasma-facing components (PFCs).

In the ITER $Q = 10$ scenario, the steady-state power that crosses the separatrix and enters into the scrape-off layer (SOL) is expected to be about 100 MW/m^2 . The distribution of the power has to be optimised such that the peak heat fluxes on the plasma facing components are below the maximum tolerable value of 10 MW/m^2 . The requirements for power handling

in ITER can be fulfilled provided 60 – 70 % of the power entering the SOL is exhausted through radiation in order to spread the power over a larger area (Pitts et al., 2009). Thus, steady-state power handling in future fusion reactors will only be possible with plasmas operated with an extremely high radiation fraction (Kotschenreuther et al., 2007; Zohm et al., 2013). Nevertheless, the heat flux onto the divertor targets is expected to increase significantly in a tokamak DEMO (Neilson et al., 2012). Approaches to cope with the heat fluxes expected in DEMO include the development of new materials that can withstand greater steady-state heat fluxes (Rieth et al., 2013), techniques and operating regimes that allow for a higher value of radiation loss (Kallenbach et al., 2013) and techniques to increase the wetted area (Ryutov, 2007). Alternative divertor concepts are being considered to control the heat loads on the divertor targets and are currently under intense investigation. Different solutions have been proposed to reduce the plasma-wall interaction in the divertor region by acting on the magnetic field topology (Ryutov, 2007; Ryutov et al., 2008; Kukushkin et al., 2005; Petrie et al., 1997; Valanju et al., 2009). One of these solutions is the so-called snowflake divertor (SF) (Piras et al., 2009).

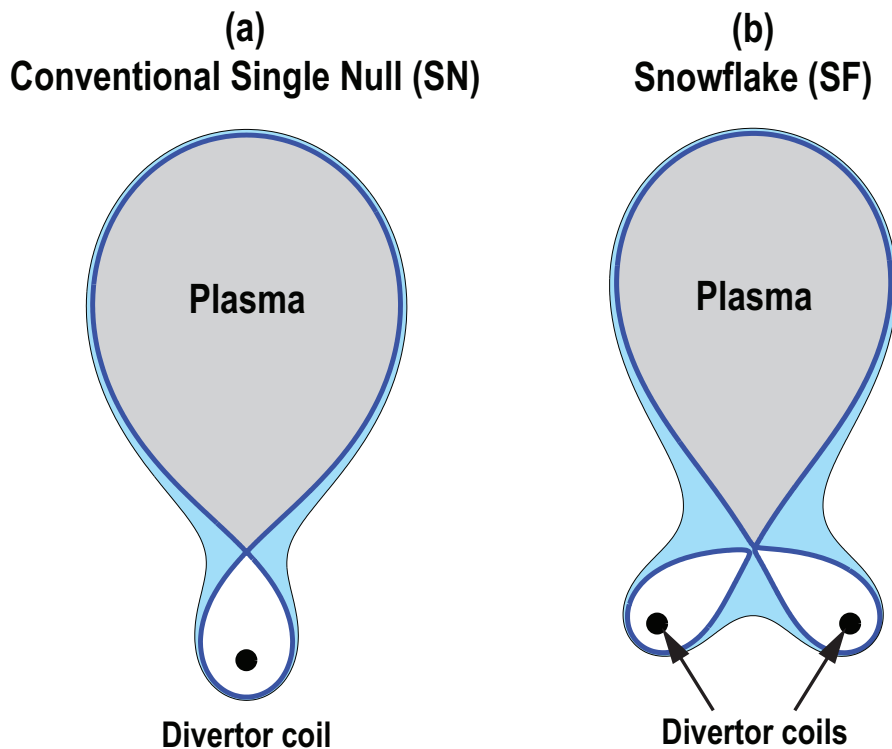


Figure 4.1 – Schematic representations of a (a) conventional single-null and (b) a snowflake divertor.

A conventional single-null (SN) divertor configuration is formed by cancelling the poloidal magnetic field B_θ at the null point, which can be achieved with a dedicated divertor coil as shown in figure 4.1(a). In the SF configuration, which requires additional divertor coils, the gradient of the poloidal field at the null-point also vanishes ($\nabla B_\theta = 0$), 4.1(b), thereby creating

a second order null-point.

In reality, an ideal SF configuration, figure 4.2(a), is only a single point in an operational domain and, in practice, a SF always possesses two neighbouring X-points separated by a finite distance. In such a configuration, the primary X-point determines the LCFS while the secondary X-point can be located either in the private flux region (PFR) of the primary separatrix, a case referred to as snowflake plus (SF+) 4.2 (b) or in the common flux region, a case referred to as snowflake minus (SF-) 4.2 (c). The proximity of any SF configuration to an exact SF can be characterised by a parameter σ , defined as the distance between the X-points, d_{xpt} , normalised with the plasma minor radius on the outboard midplane, a .

The different SF configurations can be characterised by two main parameters, σ and the angle θ , which is defined as the angle between a line connecting the two X-points and a line perpendicular to a line connecting the primary X-point and the magnetic axis (figure 4.3). As mentioned before, σ defines the proximity of the divertor configuration to an exact SF, whereas the θ parameter controls the transition between the SF+ and SF-. The range $60^\circ \lesssim \theta \lesssim 120^\circ$ corresponds to a SF+, while the range defined by $\theta \gtrsim 120^\circ$ or $\theta \lesssim 60^\circ$ denotes a SF- configuration. Due to the location of the secondary X-point with respect to the primary one, a SF- with $\theta \gtrsim 120^\circ$ is referred to as (high field side) HFS SF- whereas a SF- with $\theta \lesssim 60^\circ$ is referred to as (low field side) LFS SF-. The SF divertor configuration was first demonstrated experimentally in the TCV tokamak (Piras et al., 2009). The configuration has also now been obtained in the NSTX spherical torus (Soukhanovskii et al., 2012) and in the DIII-D tokamak (Soukhanovskii et al., 2015).

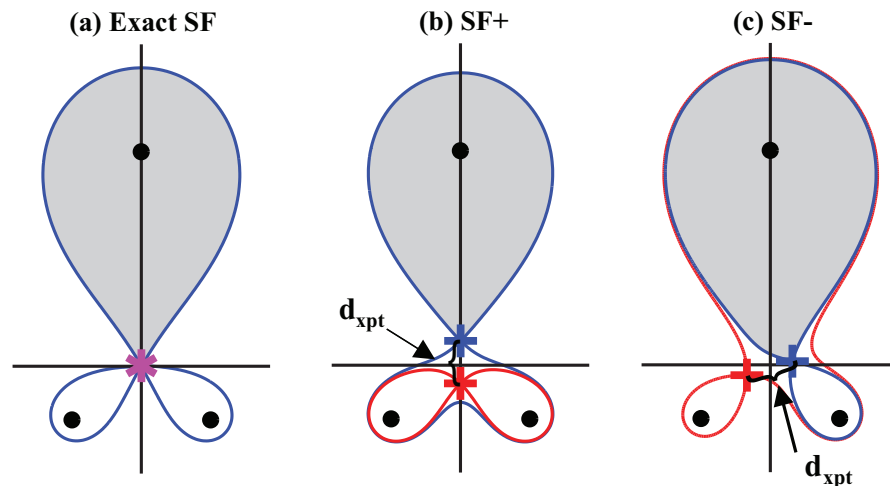


Figure 4.2 – Schematic of different SF configurations: (a) An exact SF, (b) a snowflake plus and (c) a snowflake minus configuration. The blue and red crosses represent the primary and secondary X-points, respectively, and the black circles represent the plasma magnetic axis and representative divertor coils.

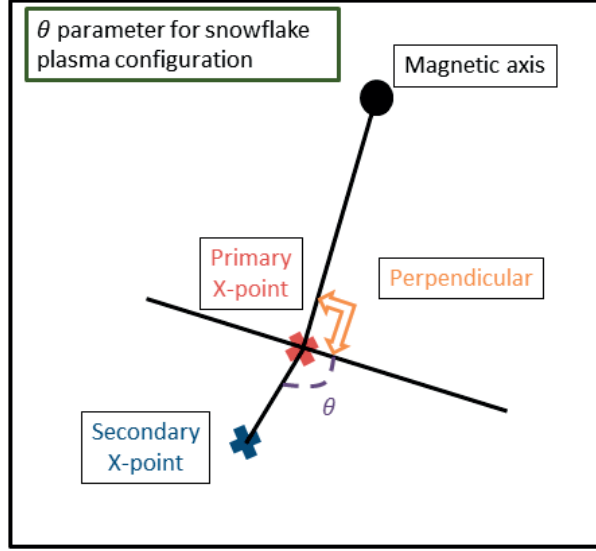


Figure 4.3 – Representation of the θ parameter for a snowflake plasma configuration.

4.1.1 Geometrical properties of snowflake plasma configuration

The small value of B_θ determines several geometric properties of the SF divertor that are perceived as advantageous with respect to reducing the peak and total heat flux to the wall. The flux expansion, the wetted area and the connection length are the most relevant geometrical quantities for a SF divertor.

The flux expansion

The variation of the distance $d\rho$ between a flux surface and the separatrix along the SOL is shown in figure 4.4. The distance $d\rho$ is shown here at three different locations: $d\rho_u$, at the outboard midplane (upstream), $d\rho_{npt}$, in the null-point region and $d\rho_t$, at the target.

The difference in poloidal magnetic flux between two adjacent flux surfaces, $d\psi$, can be expressed as $d\psi = |\vec{\nabla}\psi| d\rho$. Using the fact that $|\vec{\nabla}\psi| = R B_\theta$, B_θ being the poloidal magnetic field, yields $d\psi = R B_\theta d\rho$. The flux expansion is defined as the relative change in the distance $d\rho$ between two flux surfaces relative to the distance of a reference location in the SOL. The distance $d\rho$ at the upstream location is taken as the reference since radial fall-off lengths at the upstream location are largely determined by the core plasma parameters. As an example, the target flux expansion is given by

$$f_{\text{exp,t}} \equiv \frac{d\rho_t}{d\rho_u} = \frac{R_u B_{\theta,u}}{R_t B_{\theta,t}}, \quad (4.1)$$

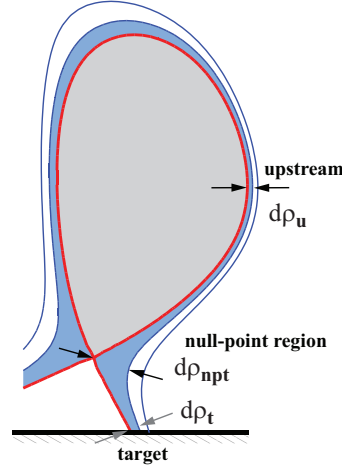


Figure 4.4 – Schematic drawing showing the distance $d\rho$ between two flux surfaces along the SOL.

where $B_{\theta,u}$ and $B_{\theta,t}$ are the magnitudes of the poloidal magnetic field at the upstream (R_u, Z_u) and target (R_t, Z_t) locations, respectively.

The wetted area

The exhaust performance of a tokamak device is determined also by the wetted area, A_w . It is the surface area of the divertor plate that is in contact with the plasma and is usually defined as an effective area such that $P_{\text{SOL}} = q_{t,\text{peak}} A_w$, where P_{SOL} is the power entering the SOL that arrives at the divertor target and $q_{t,\text{peak}}$ is the peak value of the heat flux perpendicular to the target surface. Neglecting the toroidal asymmetries, such as gaps between divertor tiles, and assuming an exponential heat flux profile in the SOL with a characteristic length, λ_{SOL} , yields (Umansky et al., 2010)

$$A_w = \frac{2\pi R_t}{\tan \alpha_t} \frac{B_{\theta,u}}{B_{\phi,u}} \lambda_{\text{SOL}} \quad (4.2)$$

where $B_{\phi,u}$ and $B_{\theta,u}$ are the magnitudes of the toroidal and poloidal field at the upstream location, R_t is the major radius of the divertor target and α is the grazing angle of the field lines with respect to the target surface.

The connection length

Another key parameter for determining the exhaust capabilities of a divertor is the connection length, $L_{||}$. The connection length is defined as the distance, along the magnetic field lines,

Chapter 4. Real time control of snowflake plasma configuration

between a target and the upstream location (outboard midplane),

$$L_{||}(\rho_u) \equiv \int_{\text{target}}^{\text{upstream}} ds_{||} = \int_{\text{target}}^{\text{upstream}} \frac{B(\rho_u, s_\theta)}{B_\theta(\rho_u, s_\theta)} ds_\theta. \quad (4.3)$$

where $ds_{||}$ is an infinitesimal displacement along the magnetic field line with ds_θ being its projection onto the poloidal plane. Figure 4.5 shows a schematic view of the typical trajectories of $ds_{||}$ and ds_θ .

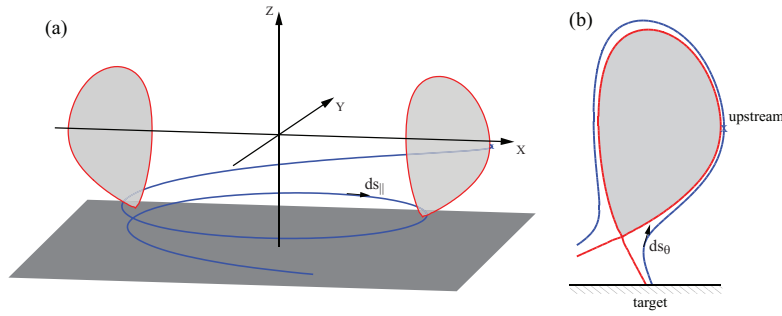


Figure 4.5 – Schematic showing the (a) trajectory along the magnetic field lines and (b) its projection into the poloidal plane.

The SF configuration enhances all the above mentioned geometrical properties. The flux expansion in the vicinity of a null-point is enhanced manifold, since the distance between the flux surfaces depends inversely on the magnitude of the poloidal field. An enhanced flux expansion at the target also corresponds to a larger wetted area. A second closely related property is the divertor volume, which increases approximately with the square of the distance between the flux surfaces. A larger divertor volume is usually associated with larger radiative losses and a greater energy transfer to non field-directed neutrals.

The SF plasma configuration is a strong candidate for solving the heat flux problem in future tokamak devices. The configuration not only aims at increasing the losses by radiation and neutrals but also provides an increase in the wetted area. Thus, an active and precise control of the magnetic configuration in order to regulate particle and heat flow is of utmost importance. Furthermore, the control algorithm should facilitate achieving various SF configurations and reduction in the peak heat flux without having an adverse effect to the core plasma. A real-time snowflake divertor detection algorithm and controller has been successfully implemented in the DIII-D tokamak (Kolemen et al., 2015). The generalised plasma position and shape controller developed in this thesis work includes the ability to provide control of advanced plasma configurations including the SF configuration. The ability of the controller design to simultaneously control the position, shape, divertor leg and X-points can be extended to various SF plasma configurations. The controller has the unique property of limiting the controlled variables to the set that is most easily controlled, while respecting the hardware

4.2. Controller optimisation of snowflake plasma configuration

limits on the poloidal field coil currents; this property can be utilised in particular to provide reliable control of SF equilibria with closely spaced X-points (i.e., the ‘exact’ snowflake, which remains largely unexplored).

4.2 Controller optimisation of snowflake plasma configuration

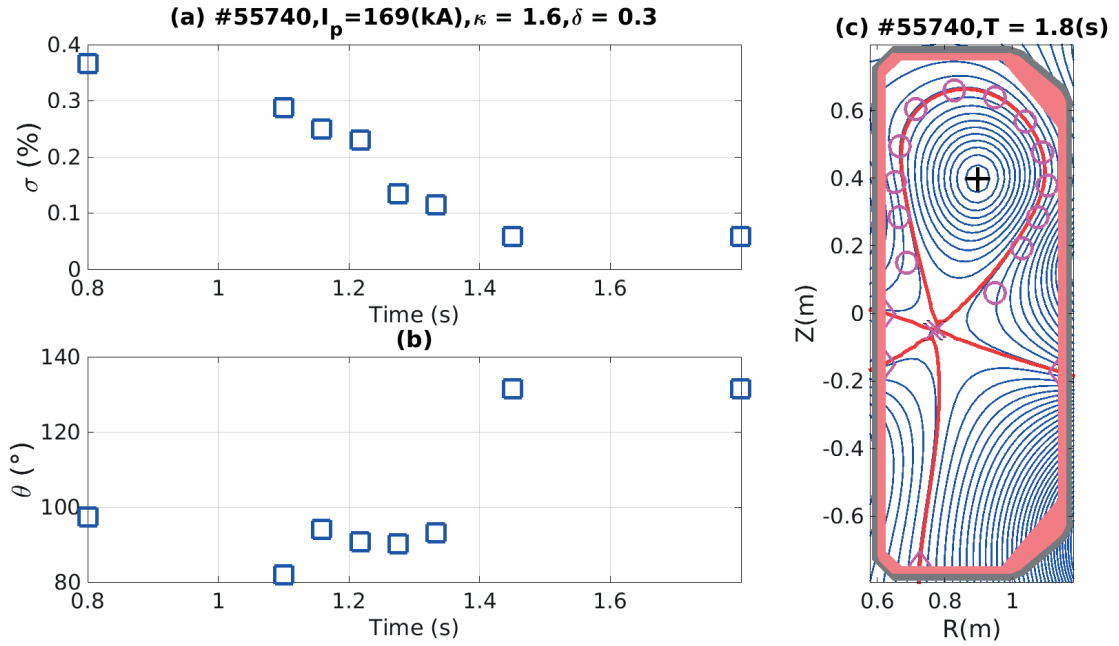


Figure 4.6 – References for (a) σ and (b) θ for a snowflake plasma configuration obtained from FBTE. The pre-programmed plasma boundary (magenta circles) and the location of the strike points (magenta diamonds) and the X-points (magenta crosses) in MGAMS. (c) Poloidal flux map (blue curves) and separatrix (red curves) and location of the magnetic axis (black cross) obtained from the free boundary equilibrium code (FBTE) at a given time instance.

The following section aims at optimising various control parameters of the generalised plasma position and shape controller for the SF plasma configuration. Figure 4.6 shows the formulation of the reference SF plasma configuration scenario to characterise the performance of the generalised plasma position and shape controller. A scenario consisting of a scan of the σ parameter for the snowflake plasma configuration was developed in MGAMS/FBTE (Hofmann, 1988; Hofmann et al., 1995), the suite of software tools used routinely on TCV to determine the poloidal coil currents and the feedback parameters for a given plasma configuration. The goal was to reach a virtually exact snowflake ($\sigma = 0$) at the end of the scan, and then hold this configuration in steady-state.

The two main parameters for improving the controller performance for the given reference scenario are as follows,

- Weight matrix, W_t that determines the level of importance of various meaningful plasma

estimators for a given plasma configuration.

- The number of actively controlled variables, \bar{z} , that determines the control of the meaningful plasma quantities.

The controller formulation allows for a rough off-line estimation of these parameters. The individual weighting with respect to each meaningful plasma quantities can be cross checked by investigating the isoflux surfaces generated by the columns of post multiplier matrix V_g . For e.g., in section 3.2.4, figure 3.7(a) and (b) shows the isoflux surfaces generated by the first two columns of the matrix V_g . Due to high weights on the vertical and radial position estimators, the first two controlled variables corresponds to plasma position control and the respective coil actuation provides a net radial and vertical magnetic field. Similarly, a choice on the number of actively controlled variables can be deduced by examining the magnitude of the singular values associated with each of the controlled variables and thus controlling only the dominant singular values.

In general, the SF plasma configuration requires optimum control of the poloidal field at the two closely spaced X-points. However, adequate control of the plasma position and shape and of the position of the strike points is also a requirement. The capability of simultaneously controlling the position, shape, divertor leg and the X-points requires a search for an optimised set of control parameters that not only supply adequate control of all the above mentioned plasma quantities but also minimises the requirements on the poloidal field coil currents. Due to the inherent design of the controller formalism, this requires a preferential weighting on the plasma position estimators in order to take over the proportional part of the position control provided by the hybrid controller of TCV, and to favour it along with the control of the plasma shape, of the position of the divertor legs and most importantly of the poloidal field at the two X-points so that these parameters appear in the higher order singular values.

4.2.1 Optimisation of the weight matrix

One of the main innovations introduced in the design of the generalised plasma position and control algorithm is its unique property of preferentially weighting different estimators. A good choice of weights on a subset of meaningful plasma estimators orients the singular value decomposition of the plant such that the chosen meaningful plasma estimators project naturally and diagonally on the output singular value subspace. In particular, the position control is ensured by the generalised plasma position and shape controller by weighting the vertical and radial position estimators of the plasma such that the first two controlled variables always correspond to vertical and radial control. The coil actuation corresponding to the set of these two controlled variables produces net radial and vertical magnetic fields on the plasma cross-section, respectively, to control the plasma position. Then, in a scenario with a given set of actively controlled variables, it is possible to choose a suitable weighting on the remaining estimators, e.g. the first moments of the plasma shape, the positions of the strike points and the poloidal magnetic field at the X-points, such that the remaining

4.2. Controller optimisation of snowflake plasma configuration

controlled variables correspond to the above mentioned plasma quantities. The option of analysing offline the isoflux surfaces actuated by the coil directions with respect to each controlled variable provides the opportunity of studying the effect of weighting different plasma estimators before implementation on a real plasma discharge.

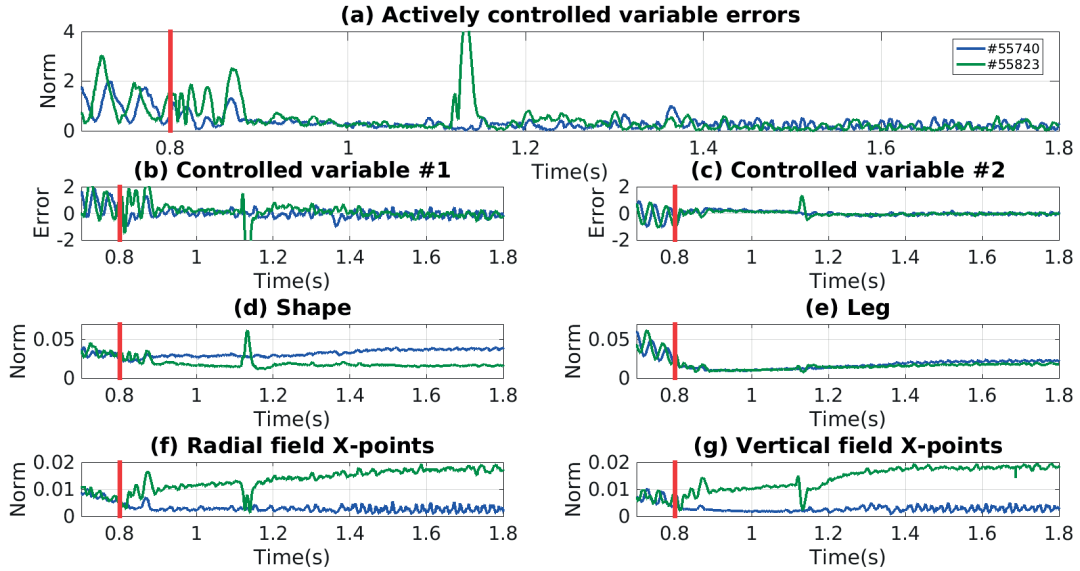


Figure 4.7 – Comparison of controller performance on a SF plasma configuration with (55740) and without (55823) preferential weighting for controlling the poloidal magnetic field at the X-points for an equal number of actively controller variables (8). (a) Time evolution of the norm of the errors on the actively controlled variables; error on the (b) first and the (c) second controlled variable related to the control of the plasma position; time dependence of the norm of the errors on variables closely related to, respectively (based on an inspection of the respective field maps), (d) plasma shape, (e) divertor leg estimator, (f) radial and (g) vertical magnetic field at the two X-points. The controller activation time is denoted by the red line.

In order to study the effect of the weighting on the plasma estimators for the SF plasma configuration, plasma discharges based on the reference formulated in figure 4.6 were performed. Figure 4.7 shows the comparison between a plasma discharge with a higher weighting associated with the poloidal magnetic field at the X-point estimator (55740), defined as the radial and vertical components of the poloidal magnetic field at the two X-points, and a plasma discharge without any preferential weighting on the various plasma estimators (55823). Figure 4.7(a) shows a reduction in the norms of the error on the active set of controlled variables with the activation of the controller in both discharges. An adequate performance of the controller with respect to the control of the position for the snowflake plasma configuration is observed in both discharges, figures 4.7(b) and 4.7(c), showing the reduction in the errors on the position controlled variables with the activation of the controller. A comparable performance was also observed between the two discharges with respect to the estimators of the positions of the four strike points; these are defined as differences between the poloidal flux at the strike point and at an X-point (the primary one for the primary strike points and the secondary one for

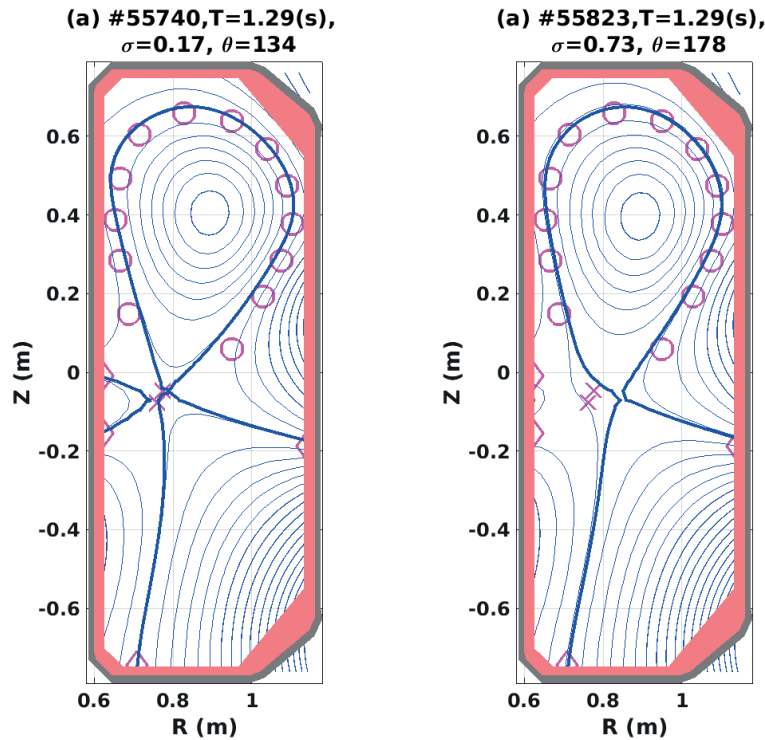


Figure 4.8 – Comparison of geometrical parameters, poloidal flux map contours (thin blue lines) and separatrix (thick blue line) for SF plasma discharges obtained from RTLIUQE (a) with (55740) and (b) without (55823) preferential weighting for controlling the poloidal magnetic field at the X-points at $T = 1.29$ s. The pre-programmed plasma boundary (magenta circles), the positions of the strike points (magenta diamonds) and the positions of the X-point (magenta crosses) are given by MGAMS.

the secondary strike points)(figure 4.7(e)). However, as expected a major difference in the discharges was associated with the control of the poloidal magnetic field at the X-points and of the plasma boundary position, defined by the difference between the poloidal flux at the primary X-point and the control points defining the remainder of plasma boundary. Both the radial and vertical components of the magnetic field at the two X-points are smaller in absolute value in discharge 55740, associated with enhanced weighting on these parameters, than in discharge 55823. (figures 4.7(f)) and 4.7(g)). Conversely, as also expected, a trade-off at the level of plasma shape control was observed, figure 4.7(d) showing a smaller norm on the shape estimator error for the discharge 55823. Figure 4.8 shows the poloidal flux contours for the two SF plasma discharges at a given time $T = 1.29$ s. The departure of the separatrix from the pre-programmed control points of the plasma boundary for the SF discharge 55740 clearly illustrates a degradation in the control of the plasma shape in comparison to discharge 55823. On the other hand, a smaller value of $\sigma = 0.13$ is obtained in discharge 55740. The disturbance in the norm of the errors on the actively controlled variables for the discharge 55823 in figure 4.7(a) is a result of the perturbation in the poloidal flux distribution introduced due to a step change in one of the poloidal field coil currents upon switching polarity.

4.2. Controller optimisation of snowflake plasma configuration

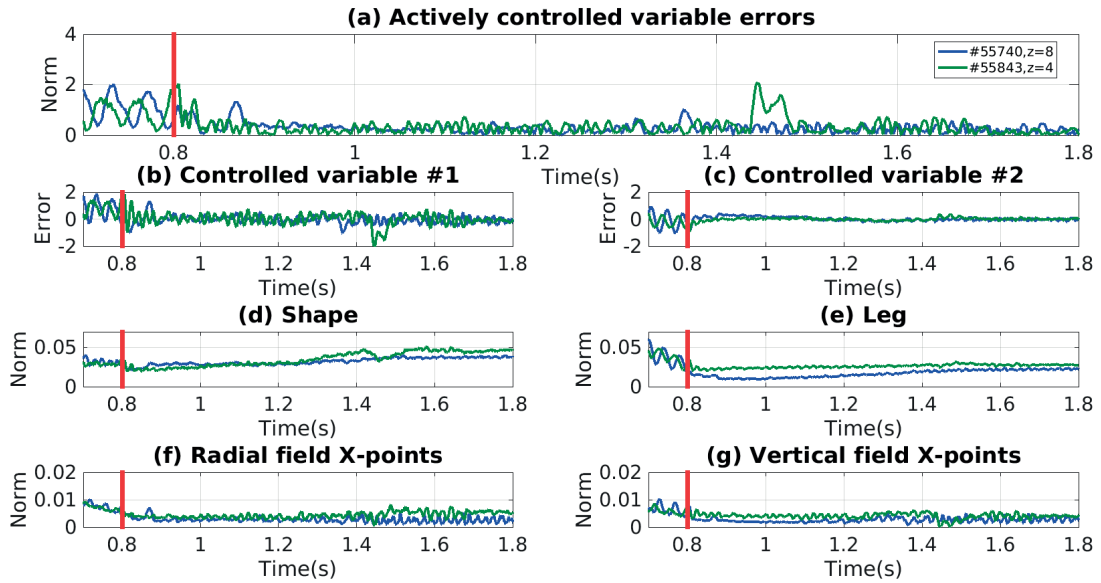


Figure 4.9 – Comparison of controller performance on a SF plasma configuration with 8 (55740) and 4 (55843) actively controlled variables with a fixed weighting for controlling the poloidal magnetic field at the X-points. (a) Time evolution of the norm of the errors on the actively controlled variables; error on the (b) first and the (c) second controlled variable related to the control of the plasma position; time dependence of the norm of the errors on variables closely related to, respectively (based on an inspection of the respective field maps), (d) plasma shape, (e) divertor leg estimator, (f) radial and (g) vertical magnetic field at the two X-points. The controller activation time is denoted by the red line.

4.2.2 Optimisation of the actively controlled variables

Section 4.2.1 illustrated the existence of a suitable weighting on the plasma estimator providing a good control on the poloidal magnetic field at the two X-points for a SF plasma configuration. However, the improved performance was at the expense of a degradation in the plasma shape. In principle, we dispose of additional degrees of freedom to improve the performance further; namely, with a fixed weighting on the poloidal magnetic field control at the X-points, a larger set of actively controlled variables can be chosen in order to improve the controller performance, at the expense of a higher demand on the poloidal field coil currents. A series of SF discharges were carried out in order to understand the effect of the number of actively controlled variables on the various plasma estimators and on the poloidal field coil currents, with the aim of finding an optimised variable set for good control of the X-points and plasma shape within the known limits on the poloidal field coil currents. The same weighting used for the X-point control in discharge 55740 (discussed in section 4.2.1) was kept throughout the scan.

The SF discharge 55829 with a larger set of actively controlled variables (11) resulted in a disruption after the controller activation. Inclusion of a larger set of controlled variables

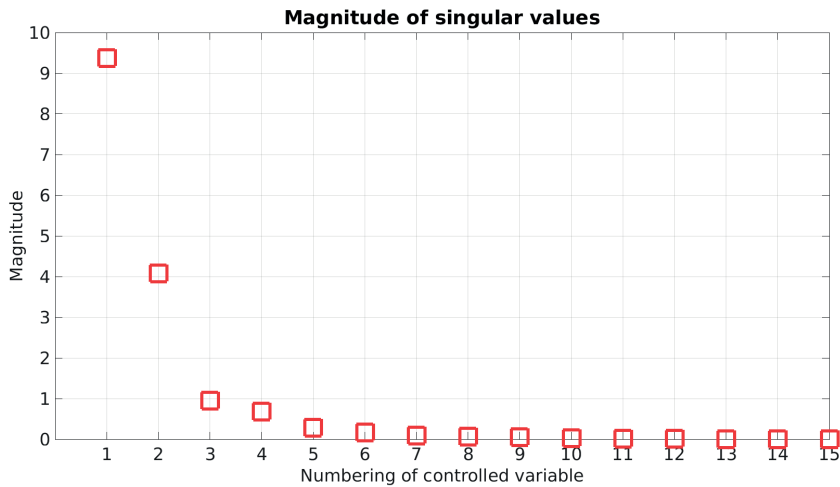


Figure 4.10 – Evolution of the magnitude of the singular values with respect to each controlled variable for the snowflake plasma configuration.

resulted in an over-demand on the coil currents and breach of one of the constraints imposed on the combination of poloidal field coil currents to limit mechanical stresses. As a result, the security system of the TCV tokamak stopped the plasma discharge. Thus, an increase in the set of the actively controlled variables to improve the simultaneous control of the plasma shape and poloidal field at the two X-points is not possible for the given reference plasma discharge. A SF plasma discharge (55843) with only 4 actively controlled variables was also performed for comparison, shown in figure 4.9 in comparison with the reference discharge 55740 with 8 variables. Figure 4.9(a) shows the reduction in the norm of the controlled variable errors after the controller activation. Adequate control on the position variables was obtained in both discharges (figures 4.9(b) and 4.9(c)). However, figures 4.9(d) and 4.9(e) illustrates a larger plasma shape and divertor leg errors for discharge 55843. In this discharge the control of the poloidal magnetic field at the two X-points is also poor (figures 4.9(e) and 4.9(f)).

Of course, the number of parameters that could be varied is very large: number of controlled variables, individual weights for each of them, individual proportional and integral gains, etc. Within the finite number of discharges that could be explored in the course of the present study, the optimum is represented by discharge 55740 with 8 controlled variables. Figure 4.10 shows the evolution of the magnitude of the singular values associated with each of the controlled variables for the SF plasma discharge 55740. The performance of the controller, in terms relevant to SF physics, is optimal as shown in Figure 4.11. Figure 4.11(a) shows the reduction in the norm of the actively controlled variables with the controller activation. Figures 4.11(b) and 4.11(c) show the comparison between the references and measurements of the σ and θ SF parameters. In general, the tracking of the σ parameter appears satisfactory. However, at steady state an average $\sigma = 0.2$ was obtained as compared to the pre-programmed reference $\sigma = 0.06$ in FBTE. Figure 4.11(c) reveals a rapid variation in the θ parameter after $T = 1.2$ s, corresponding to multiple transitions between the snowflake plus and snowflake

4.3. Comparison of the controller performance with respect to the TCV hybrid controller and implications for snowflake physics

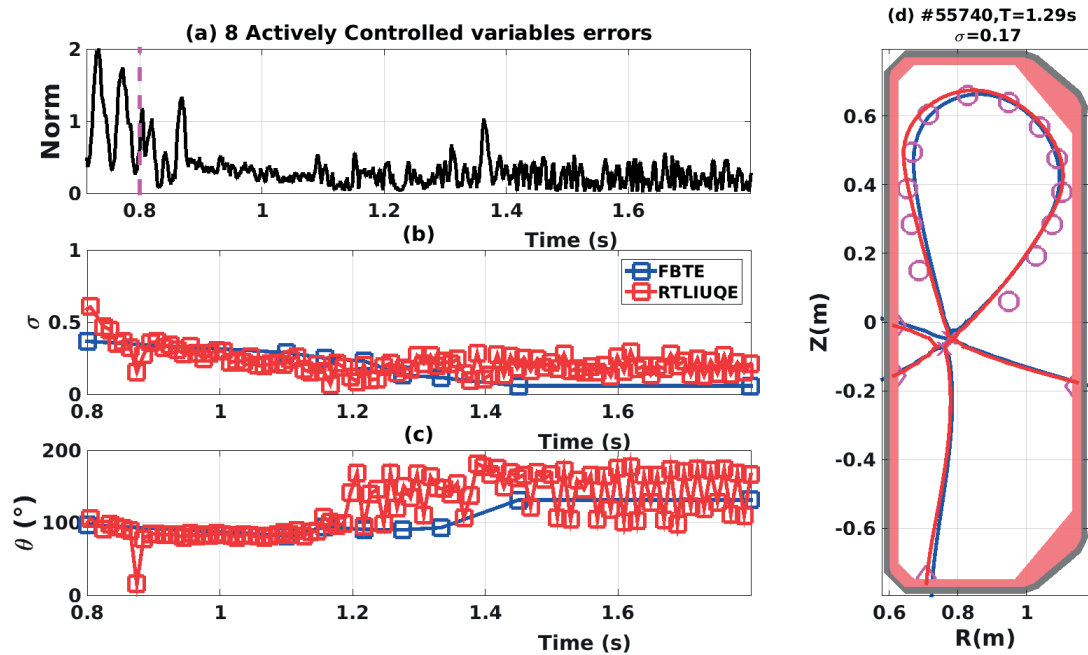


Figure 4.11 – Controller performance on a SF plasma configuration with 8 actively controlled variables and fixed preferential weighting for controlling the poloidal magnetic field at the X-points. (a) Time evolution of the norm of the actively controlled variable errors. (b) σ and (c) θ parameters obtained from FBTE and RTLIUQE. (d) Comparison between the separatrix obtained from FBTE and RTLIUQE at $T = 1.29$ s. The pre-programmed plasma boundary (magenta circles), the locations of the two X-points (magenta crosses) and the positions of the strike points (magenta diamonds) are given by MGAMS.

minus configurations, a common feature of SF plasma configurations at low σ (the two becoming of course degenerate at $\sigma = 0$). Figure 4.11(d) shows the difference between the separatrix obtained from FBTE and from the RTLIUQE reconstruction at a given time instance $T = 1.29$ s, again revealing adequate control with some departure towards the inner wall of the vessel.

4.3 Comparison of the controller performance with respect to the TCV hybrid controller and implications for snowflake physics

The aim of this section is to discuss the performance of the new generalised plasma position and shape controller vs. the TCV hybrid controller for the reference SF plasma configuration defined in figure 4.6. For the former we use discharge 55740 with optimised controller setup. The same reference was then repeated with the TCV hybrid controller emulated on the digital control system of the TCV tokamak (55463). The difference between the performance of the two controllers is evaluated with RTLIUQE and various plasma diagnostics present on the TCV tokamak. We focus in particular on various properties derived from the equilibrium solver

such as e.g. the geometrical parameters for the SF configuration, σ and θ , and the connection length $L_{||}$ in the vicinity of the X-point, as well as edge plasma measurements provided by Langmuir probes and visible and infrared cameras.

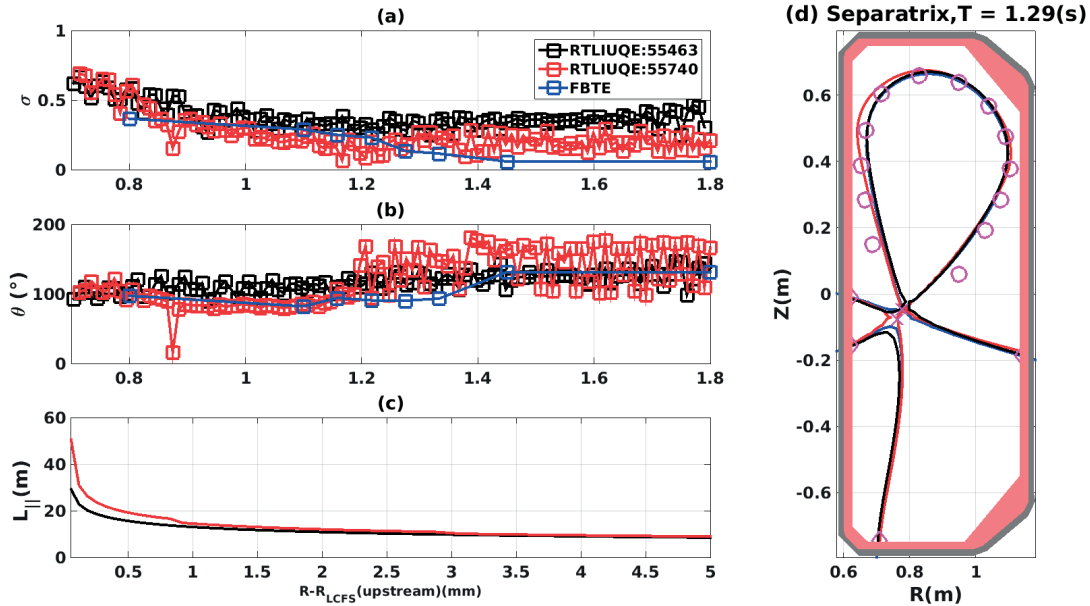


Figure 4.12 – Comparison of the performance of the TCV hybrid controller and the optimised generalised plasma position and shape controller on a SF plasma configuration. Time evolution of the geometrical parameters (a) σ and (b) θ ; (c) connection length $L_{||}$ as a function of the upstream distance of the flux surface from the LCFS at given time $T = 1.29$ s. (d) Difference between the separatrix obtained for the two plasma discharges from RTLIUQE at $T = 1.29$ s. On the right-hand side are shown the pre-programmed plasma boundary (magenta circles) and the locations of the two X-points (magenta crosses) and of the strike points (magenta diamonds) given by MGAMS.

Figure 4.12 shows a comparison of the equilibrium properties. Figure 4.12(a) shows the pre-programmed reference and the measurement of the σ parameter for the two discharges. The performance of the generalised plasma position and shape controller on this score is clearly better. The rapid transitions in the θ parameter with this controller, seen in figure 4.12(b), are primarily a result of the low value of σ reached in this case, as discussed earlier. Figure 4.12(c) illustrates the difference in the connection length $L_{||}$ between the two plasma discharges at a given time $T = 1.29$ s. A longer connection length is observed for the discharge performed with the generalised plasma position and shape controller, signifying the presence of a lower poloidal magnetic field distribution in the region of the two X-points, consistent with the proximity to an exact SF configuration. Figure 4.12(d) compares the shapes, and on this score the two controllers have comparable performance, each departing from the reference shape slightly at different locations. The shape evolution in time is displayed in figure 4.13. It is seen that after the activation of the advanced RT shape controller at $T = 0.8$ s, the shape evolves rapidly towards the desired reference, especially in the X-point region thanks to the

4.3. Comparison of the controller performance with respect to the TCV hybrid controller and implications for snowflake physics

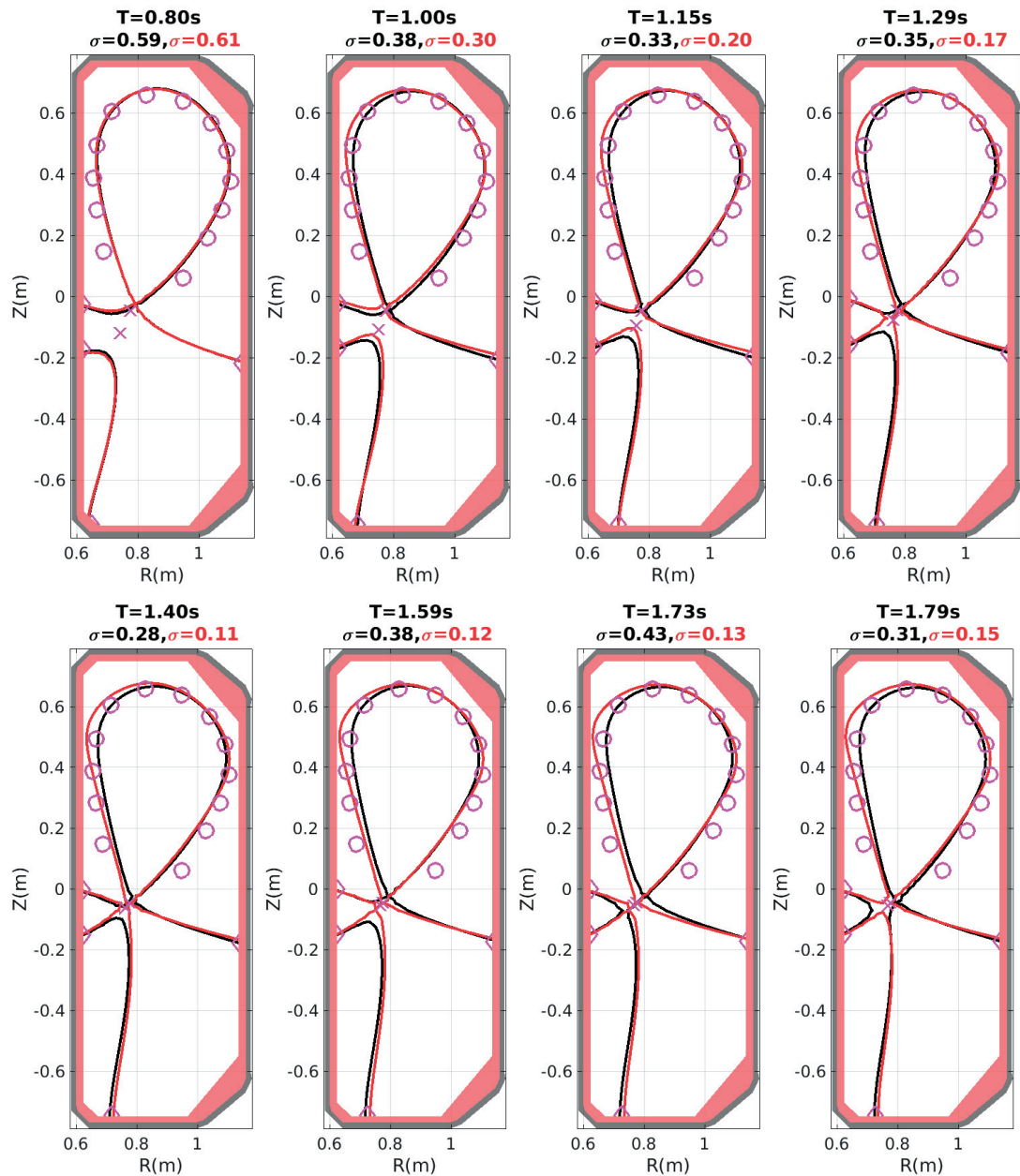


Figure 4.13 – Difference between the separatrix obtained from RTLIUQE for the two plasma discharges at various time instances during the discharge. The red separatrix denotes discharge 55740, while the black one represents 55463. The pre-programmed plasma boundary, strike points and X-points are denoted by magenta circles, magenta diamonds and magenta crosses, respectively.

preferential weighting. However, the control of the plasma shape deteriorates with time, with the boundary approaching the inner wall and ultimately coming in contact with it.

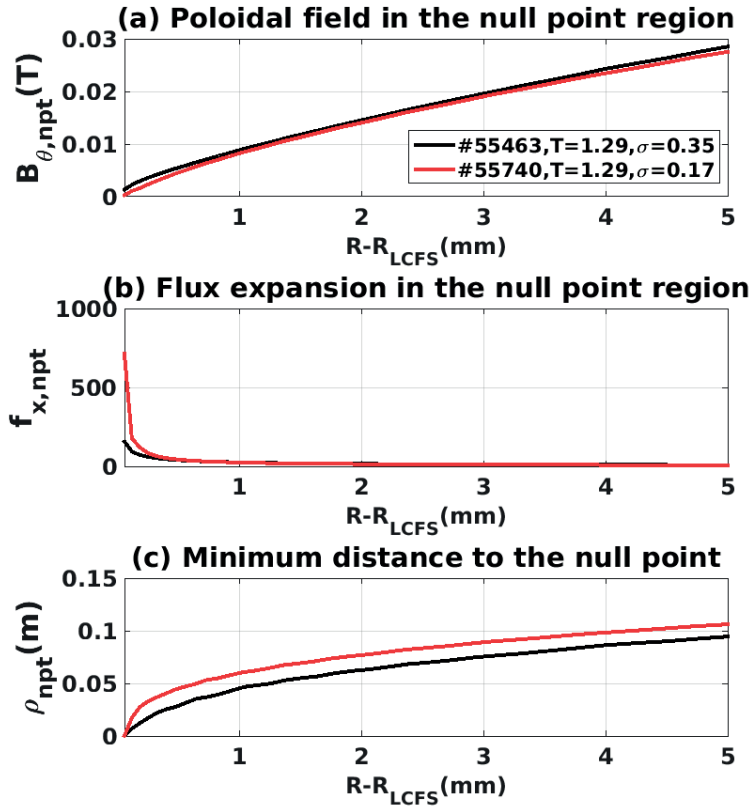


Figure 4.14 – Comparison of SF physics parameters between discharges controlled by the TCV hybrid controller and the optimised generalised plasma position and shape controller, respectively. (a) $B_{\theta, npt}$, poloidal field and (b) $f_{x, npt}$, flux expansion, in the vicinity of the null point, and (c) variation of ρ_{npt} , minimum distance of the field line to the X-point, as functions of upstream distance of the flux surface from the LCFS.

Figure 4.14 shows the comparison between various other field and flux-surface properties for the plasma discharges performed with different controllers. This confirms that discharge 55740, performed with the generalised plasma position and shape controller, displays all the favourable properties associated with the SF configuration, including a higher flux expansion, a lower poloidal magnetic field, and a larger divertor volume.

Two main diagnostics, the infrared camera and the Langmuir probes, were used in order to study the impact of the improved plasma performance provided by the controller design. The infrared camera provides information on the heat flux profile around the inner strike points (SP1 and SP2), and the Langmuir probes provides the ion flux at all four strike points (SPs). Figure 4.15 shows the comparison of the two plasma discharges with respect to the time evolution of the deposited power and the peak heat flux derived from the infrared diagnostic and the peak ion flux at all strike points from the Langmuir probes. The deposited power and

4.3. Comparison of the controller performance with respect to the TCV hybrid controller and implications for snowflake physics

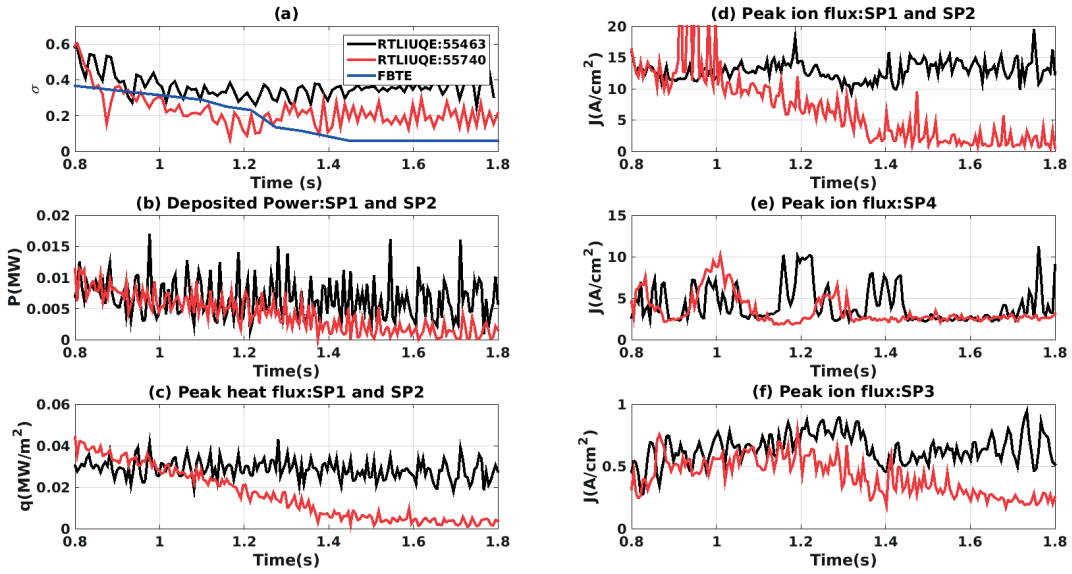


Figure 4.15 – Comparison of diagnostic data in SF configurations controlled with the TCV hybrid controller and the optimised generalised plasma position and shape controller, respectively. (a) Reference and measurement of the σ parameter obtained from FBTE and RTLIUQE for the plasma discharges. (b) Time evolution of the total deposited power and (c) peak value of heat flux deposited on SP1 and SP2, obtained from the infrared diagnostic. Time dependence of the peak value of the ion flux at the SP1 and SP2 (d), SP4 (e) and SP3 (f).

the peak heat flux at SP1 and SP2, as well as the ion particle flux, decrease during the scan to lower σ for the discharge 55740. This is in stark contrast with 55463 performed with the TCV hybrid controller in which these parameters remain approximately constant for the entire time range. This is consistent with the modest reduction in σ achieved with this controller. Indeed, the flux to SP3 and SP4 also remains approximately constant in this case. It is striking that the flux to all strike points except SP4 decreases sharply with time in discharge 55740. The truly large decrease towards the end of the discharge may well be related to the diminished distance of the plasma boundary from the inner wall in the upper part of the plasma, causing the SOL to shrink and the plasma to become effectively limited at the end of the discharge. The flux to SP4 would be largely unaffected by this as most of the flux reaching it is generated on the LFS and remains connected to SP4. However, a significant reduction is observed already between 0.8-1.3s, when the boundary has not yet touched the wall, indicating that there may be physics effects at play related to the proximity to the exact SF. Increased radiation from the divertor volume could be hypothesized to be contributing to the reduced flux. Unfortunately no bolometer measurements were available to confirm this in these discharges.

Figure 4.16(a) compares the heat flux profile obtained for the two plasma discharges at SP1 and SP2 at a fixed time during the plasma discharge $T = 1.29$ s. In both cases, the heat deposited at the secondary strike point SP2 is too low to resolve. However, a clear peaked heat flux profile evolution is observed in both discharges at SP1 (primary strike point). Peaked profiles are also

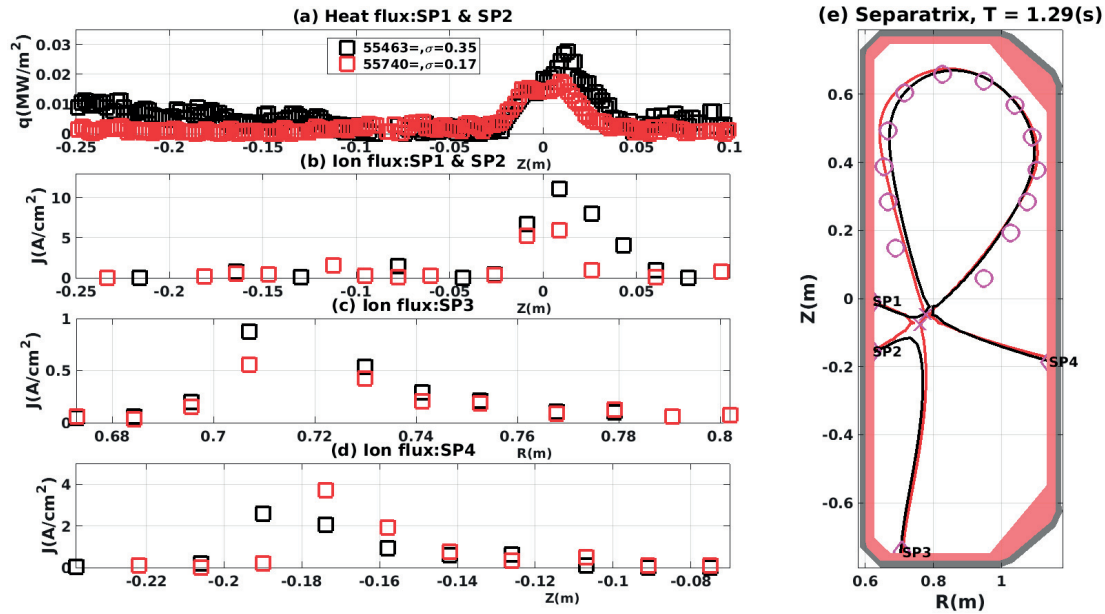


Figure 4.16 – Comparison of SF discharges controlled by the TCV hybrid controller and the advanced shape controller, respectively, at fixed time $T=1.29$ s, with respect to heat flux profile on SP1 and SP2 obtained from the infrared camera, and ion flux profile on (b) SP1 and SP2, (c) SP3 and (d) SP4 obtained from the Langmuir probes. The plasma shapes are shown in (d).

seen at SP3 and SP4 in both cases.

Figure 4.17 shows the comparison between equilibrium reconstruction and visible light emission obtained with an unfiltered, tangentially viewing camera after the controller activation ($T = 0.8$ s) for discharges 55463 and 55740. The majority of the emission in the plasma discharges is concentrated in the X-point region and the divertor legs. The emission is primarily the result of strong carbon radiation from the impurities generated at the graphite first wall. Unfortunately, the camera images between the two discharges cannot be compared since the exposure times of the camera were different, 2 ms in discharge 55740 and, $33\mu\text{s}$ in 55463. Nevertheless, the images obtained from the camera at various time instances during the discharge 55740 shows the presence of a hot spot near the inner wall, resulting in a finite amount of radiation. The closeness of the separatrix, together with the concentration of the visible radiation emission spectrum near the inner wall confirms that at least part of the reduction in the heat and particle flux during the discharge 55740 is due to the flux fraction deposited on the upper inner wall.

4.4 Summary and conclusions

The chapter provides an introduction to the problem of power exhaust in a DEMO tokamak and discusses the potential solutions to ameliorate it. It discusses in detail the application of

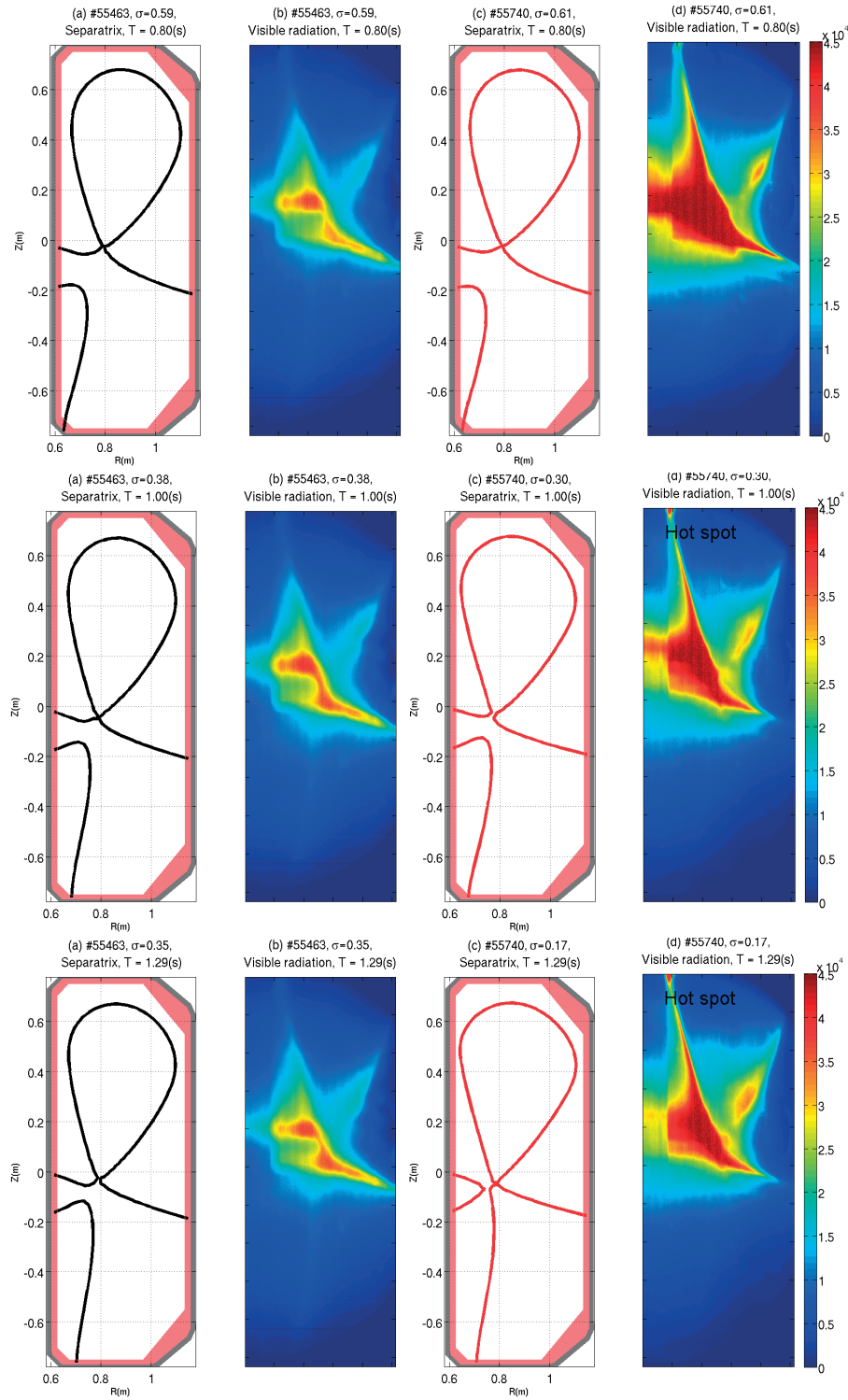


Figure 4.17 – Equilibrium reconstructions and images from the tangential visible CCD camera for the plasma discharges 55740 and 55463 at various time instances.

Chapter 4. Real time control of snowflake plasma configuration

the generalised plasma position and shape controller on a snowflake plasma configuration, a potential solution to reduce heat loads onto the material surfaces in diverted tokamak plasmas. The chapters reports on the experimental investigation of the optimised set of control parameters, primarily the weight matrix W_i concerning the control of poloidal magnetic field at the two nearby X-points and the optimal number of actively controlled variables, associated with the control of various plasma estimators and requirements on the poloidal field coil currents. It illustrates the improvement in SF plasma configuration with the application of the generalised plasma position and shape controller by enhancing the various geometrical properties for e.g., the connection length and flux expansion associated with SF divertors.

The result achieved on the snowflake control is only a partial success, partly because of the limited experimental time available. In particular, better control could conceivably be obtained on the overall shape even whilst retaining good control of the X-points, through a further optimisation of the free parameters. It certainly should be possible in particular to detach the plasma boundary from the wall. This unfortunate occurrence meant that the physics properties of the near-exact SF could not really be meaningfully studied. It is, however, highly encouraging that a low σ could be obtained and steadily maintained. Whether the value obtained is the ultimate limit for steady-state control or an even lower σ is possible remains an open question both from the control standpoint and the SF physics standpoint.

It must be stressed that equilibrium reconstruction is not immune to errors and is particularly difficult for a snowflake plasma in the X-point region. Ultimately, our knowledge of the configuration, and particularly the proximity to the "exact" SF, depends on the accuracy of the reconstruction. While other diagnostics (e.g., cameras) can provide additional information, the precision with which a reconstructed image can identify the X-points is also limited, and typically more limited than the magnetic equilibrium reconstruction itself. Indeed, running the LIUQE code in different modes and with different input parameters, for the plasmas studied here, has been shown to give considerably different results, as large as or larger than those discussed in this chapter between different discharges. The question of what could be improved or which version of the reconstruction can be trusted most is an open one and is outside the scope of this thesis. With respect to the work developed here, however, the internal consistency of the controller performance remains the crucial result - i.e., its ability to match the desired reference with a given observer, irrespective of its intrinsic accuracy.

5 Conclusions

Stable operation of tokamak plasmas at high performance requires several plasma control problems to be handled simultaneously. Moreover, the complex physics which governs the tokamak plasma evolution must be studied and understood to make correct choices in controller design. This mutual inter-dependence has informed this thesis, using control solutions as an experimental tool for physics studies, and using physics knowledge for developing new advanced control solutions. The thesis addresses two main issues: The design and testing of a generalised plasma position and shape controller and the application of the controller to improve plasma performance of an advanced plasma configuration, i.e., the snowflake divertor.

5.1 Generalised plasma position and shape controller

The plasma shape in a tokamak plays a particularly important role in the stability of global MHD modes and in heat and particle transport. Departures of the plasma parameters from the model values used in the pre-calculation, most notably in the plasma current profile, results in unwanted shape changes. Active plasma shape control thus becomes necessary when better accuracy is required. Exploring unconventional shapes and topologies, in view of possible alternative concepts for a reactor beyond ITER, remains part of the TCV mission. In current practice only the plasma elongation is controlled in real time, and only in selected scenarios. Developing a generalised plasma position shape controller for TCV would greatly facilitate these developments and open the way to studying the physics of these configurations. The shaping flexibility of a device such as ITER, by contrast, is extremely limited. Nevertheless, the controller design remains important there to ensure the accuracy of the boundary for optimal performance while maintaining the required clearance from the wall for device safety.

The work described in the thesis gives a detailed insight into the design of a generalised plasma position and shape controller for advanced plasma configurations on TCV tokamak. The formulation of the controller was made possible by the powerful and highly modular digital real time control system, by flexibility of actuators and diagnostics and by the deployment

of a real time Grad-Shafranov solver with a sub-ms cycle time. The thesis describes the utilisation of the SVD formalism, to limit the controlled parameters to the set that is most easily controlled, while respecting the hardware limits on the poloidal field coil currents. The thesis examines the coupling of the TCV hybrid controller with the generalised plasma position and shape controller with help of a linearised plasma model (RZIp). A comprehensive verification and optimisation of the new controller design based on the RZIp plasma model is also provided. The study also describes the implementation of the generalised plasma position and shape controller design with the TCV hybrid controller on the digital control system of the TCV tokamak. A report on the experimental identification and existence of a suitable range of controller gains, granting good control of the plasma position without exciting instabilities, particularly the vertical instability, is provided. Successful experimental implementation of the control algorithm for both fixed and time varying plasma position and shape for limiter and divertor plasma discharges is reported. In addition, an insight is given into various salient features of the controller design improving its performance, mainly the anti-windup formalism and the bumpless formalism.

5.2 Real time control of snowflake plasma configuration

In DEMO and in future fusion power plants, the severity of the power handling in the divertor will substantially increase since the fusion power and corresponding auxiliary heating power are predicted to be around 3 – 10 times larger than those in ITER. The snowflake is one of several divertor configurations that have emerged as alternative options to the conventional divertor configuration. The configuration not only aims at increasing the losses by radiation and neutrals but also provides an increase in the wetted area. Thus, an active and precise control of the magnetic configuration in order to regulate particle and heat flow is of utmost importance.

The thesis discusses the application of the generalised plasma position and shape controller to the snowflake plasma configuration in view of improving its performance in contrast to the TCV hybrid controller. The study illustrates the experimental identification of the optimised controller parameters to provide an efficient control of the poloidal magnetic field at the two closely spaced X-points. It reports a marked improvement in the performance with respect to the control of the poloidal magnetic field at the two X-points. However, the physics properties of the near-exact SF could not be meaningfully studied due to the intersection of the plasma boundary with the wall. Through further optimisation of the free parameters, a better control of overall shape even whilst retaining good control of the X-points is still likely.

A RZIp and Sign-bit controller

A.1 RZIP

Definition for the elements of the M and R matrices,

$$\begin{aligned}
 M_{pR} &= \frac{\partial L_p}{\partial R} + \frac{2\pi R_o B_{zo}}{I_{po}}, M_{Rp} = \frac{2\pi R_o B_{zo}}{I_{po}} + \mu_o \Gamma_o, \\
 M_{RR} &= \frac{\mu_o}{2} \frac{\partial \Gamma}{\partial R} + \frac{2\pi R_o}{I_{po}} \frac{\partial B_z}{\partial R} + \frac{2\pi B_{zo}}{I_{po}}, M_{ZZ} = -\frac{2\pi R_o}{I_{po}} \frac{\partial B_r}{\partial Z}, \\
 M_{ZR} &= -\frac{2\pi R_o}{I_{po}} \frac{\partial B_r}{\partial R}, M_{RZ} = \frac{2\pi R_o}{I_{po}} \frac{\partial B_z}{\partial Z}, \\
 R_{Rp} &= \frac{2\pi R_o}{I_{po}} \dot{B}_{zo} + \frac{\mu_o \Gamma_o \dot{I}_{po}}{I_{po}} + \mu_o \dot{\Gamma}_o, \\
 R_{RR} &= \frac{\mu_o}{2} \frac{\dot{I}_{po}}{I_{po}} \frac{\partial \Gamma}{\partial R} + \frac{2\pi \dot{B}_{zo}}{I_{po}}, \\
 R_{vR} = R_{Rv} &= \frac{\dot{I}_{po}}{I_{po}} \frac{\partial M_{vp}}{\partial R}, R_{aR} = R_{Ra} = \frac{\dot{I}_{po}}{I_{po}} \frac{\partial M_{ap}}{\partial R}, \\
 R_{vZ} = R_{Zv} &= \frac{\dot{I}_{po}}{I_{po}} \frac{\partial M_{vp}}{\partial Z}, R_{aZ} = R_{Za} = \frac{\dot{I}_{po}}{I_{po}} \frac{\partial M_{ap}}{\partial Z}, \\
 R_{pR} &= \frac{\partial R_p}{\partial R} + \frac{2\pi R_o \dot{B}_{zo}}{I_{po}} - \frac{2\pi R_o B_{zo}}{I_{po}^2} \dot{I}_{po}, \\
 S_R &= -\frac{\mu_o}{2} \frac{\partial \Gamma}{\partial l_i} (I_{po} \delta L_i) - \frac{\mu_o}{2} \frac{\partial \Gamma}{\partial \beta_p} (I_{po} \delta \beta_p) - \frac{\mu_o}{2} \frac{\partial \Gamma}{\partial l_i} (\dot{I}_{po} \delta L_i) - \frac{\mu_o}{2} \frac{\partial \Gamma}{\partial \beta_p} (\dot{I}_{po} \delta \beta_p)
 \end{aligned} \tag{A.1}$$

A.2 Sign-bit Controller

In order for the poloidal field coil to switch the current polarity, it is necessary to send to its power supply a digital signal, i.e., a sign bit of suitable polarity, magnitude and pulse width. Sign bits in TCV are pre-calculated in MGAMs (Hofmann and Jardin, 1990) based on the

Appendix A. RZIp and Sign-bit controller

feedforward PF coil current requests and sent as feedforward traces to the PF coil controllers. As the currents are based on FBTE calculations, which in turn are based on assumptions about the current profile - typically assumed to be Ohmic-like - substantial auxiliary heating can cause a significant departure from the predicted currents, in which case the pre-calculated sign bits may be inaccurate. If a current reaches zero and the relevant sign bit has not been issued, the coil current languishes at zero and the current evolution is different from the pre-programmed request. This problem is greatly exacerbated by the generalised plasma position and shape controller algorithm, which often requests coil currents that are very different from the pre-programmed ones. The sign-bit issue is an inherent hindrance to true real-time control, and its resolution was seen as an integral component of the shape controller development. The new, fully digital, distributed control system (SCD) presents an opportunity for the development of a sign bit controller based on the real time measurement of the poloidal field coil currents. An algorithm based on the following scheme has been developed in the Simulink block diagram environment and has been successfully tested experimentally. Two unique thresholds (Th_1 and Th_2 , $Th_1 > Th_2$) for the poloidal field coil currents are defined. Upon the crossing of the first threshold by the absolute value of a given poloidal field coil current, a sign-bit of opposite polarity is generated. When the poloidal field coil current crosses the second threshold (lower than the first one), a sign-bit of the same polarity as the previous sign-bit is generated. Further, when the poloidal field coil currents stays under the second threshold, alternating sign-bits separated by a predefined time interval are generated until the poloidal field coil current switches polarity.

Bibliography

- M. M. M. Al-Husari, B. Hendel, Jaimoukha I. M., Kasenally E. M., and Limebeer D. J. N. Vertical Stabilization of Tokamak Plasmas. In *30th IEEE Conference on Decision and Control*, Brighton (UK), 1991. URL <http://ieeexplore.ieee.org/stamp/stamp.jsp?arnumber=261545>.
- R. Albanese, E. Coccolese, and G. Rubinacci. Plasma modelling for the control of vertical instabilities in tokamaks. *Nuclear Fusion*, 29:1013, 1989.
- G. Ambrosino, M. Ariola, A. Pironti, J. B. Lister, and P. Vyas. A model based controller design approach for the TCV tokamak. In *IEEE International Conference on Control Applications*, number September, pages 202–206, 1998. ISBN 078034104X. URL <http://ieeexplore.ieee.org/document/728366/>.
- G. Ambrosino, M. Ariola, G. Tommasi, A. Pironti, F. Sartori, E. Joffrin, and F. Villone. Plasma srike-point sweeping on JET tokamak with the eXtreme shape controller. *IEEE Transactions on Plasma Science*, 36(3 PART 2):834–840, 2008. ISSN 00933813. doi: 10.1109/TPS.2008.922920.
- H. Anand, C. Galperti, S. Coda, B. Duval, F. Felici, T. Blanken, J.-M. Moret, O. Sauter, T. Goodman, and D. Kim. Distributed digital real-time control system for the TCV tokamak and its applications. In *Proceedings of the 26th IAEA Fusion Energy Conference, Kyoto, Japan*, pages 1–8, 2016.
- M. Ariola and A. Pironti. Plasma shape control for the JET tokamak: An optimal output regulation approach. *IEEE Control Systems Magazine*, 25(5):65–75, 2005. ISSN 02721708. doi: 10.1109/MCS.2005.1512796. URL <http://ieeexplore.ieee.org/document/1512796/>.
- M. Ariola and A. Pironti. *Magnetic Control of Tokamak Plasmas*. 2008. ISBN 978-1-84800-323-1.
- M. Ariola, G. Ambrosino, J.B. Lister, A. Pironti, F. Villone, and P. Vyas. Modern plasma controller tested on the TCV tokamak. *Fusion Technology*, 36(2):126–138, 1999. ISSN 07481896.
- J. Aström and B. Wittenmark. *Computer Controlled Systems*, volume 53. 1997. ISBN 9788578110796. doi: 10.1017/CBO9781107415324.004.
- Y. Camenen, A. Pochelon, R. Behn, A. Bottino, A. Bortolon, S. Coda, A. Karpushov, O. Sauter, G. Zhuang, and the TCV Team. Impact of plasma triangularity and collisionality on electron

Bibliography

- heat transport in TCV L-mode plasmas. *Nuclear Fusion*, 47(7):510–516, 2007. ISSN 0029-5515. doi: 10.1088/0029-5515/47/7/002. URL <http://stacks.iop.org/0029-5515/47/i=7/a=002?key=crossref.aaab988e9b17433e71f4553a1c7b4886>.
- S L Campbell and Carl D Meyer. *Generalized Inverses of Linear Transformations*, volume 56. 1979. ISBN 048666693X. doi: 10.1137/1.9780898719048. URL <http://www.amazon.fr/Generalized-Inverses-Linear-Transformations-Campbell/dp/048666693X>.
- M. S. Chu and M. Okabayashi. Stabilization of the external kink and the resistive wall mode. *Plasma Physics and Controlled Fusion*, 52:123001, 2010. ISSN 0741-3335. doi: 10.1088/0741-3335/52/12/123001. URL <http://stacks.iop.org/0741-3335/52/i=12/a=123001>.
- J. W. Connor. A review of models for ELMs. *Plasma Physics and Controlled Fusion*, 40(2):191, 1998. ISSN 0741-3335. doi: 10.1088/0741-3335/40/2/003. URL <http://iopscience.iop.org/0741-3335/40/2/003>{%}5Cn<http://iopscience.iop.org/0741-3335/40/2/003/pdf/0741-3335/40/2/003.pdf>.
- A. Coutlis, I. Bandyopadhyay, J. B. Lister, P. Vyas, R. Albanese, D. J. N. Limebeer, F. Villone, and J. P. Wainwright. Measurement of the open loop plasma equilibrium response in TCV. *Nuclear Fusion*, 39(5):663–683, 1999. ISSN 0029-5515. doi: 10.1088/0029-5515/39/5/307. URL <http://stacks.iop.org/0029-5515/39/i=5/a=307>.
- P. C. de Vries, M. F. Johnson, B. Alper, P. Buratti, T. C. Hender, H. R. Koslowski, and V. Riccardo. Survey of disruption causes at JET. *Nuclear Fusion*, 51(5):053018, 2011. ISSN 0029-5515. doi: 10.1088/0029-5515/51/5/053018. URL <http://stacks.iop.org/0029-5515/51/i=5/a=053018>.
- T. Eich, A. Herrmann, and J. Neuhauser. Nonaxisymmetric energy deposition pattern on ASDEX upgrade divertor target plates during type-I edge-localized modes. *Physical review letters*, 91(19):195003, 2003. ISSN 0031-9007. doi: 10.1103/PhysRevLett.91.195003. URL <http://link.aps.org/doi/10.1103/PhysRevLett.91.195003>.
- T. E. Evans, R. A. Moyer, J. G. Watkins, P. R. Thomas, T. H. Osborne, J. A. Boedo, M. E. Fenstermacher, K. H. Finken, R. J. Groebner, M. Groth, J. Harris, G. L. Jackson, R. J. La Haye, C. J. Lasnier, M. J. Schaffer, G. Wang, and L. Zeng. Suppression of large edge localized modes in high confinement DIII-D plasmas with a stochastic magnetic boundary. In *Journal of Nuclear Materials*, volume 337-339, pages 691–696, 2005. ISBN 0022-3115. doi: 10.1016/j.jnucmat.2004.10.062. URL <http://www.sciencedirect.com/science/article/pii/S0022311504008323>.
- J. R. Ferron. DEVELOPING ISOFLUX SHAPE CONTROL AND REAL TIME EQUILIBRIUM RECONSTRUCTION A plan to achieve accurate discharge control for all plasma conditions. pages 1–10, 2001.
- J. R. Ferron, M. L. Walker, L. L. Lao, H. E. John, D. A. Humphreys, and J. A. Leuer. Real time equilibrium reconstruction for tokamak discharge control. *Nuclear Fusion*, 38(7):1055–1066, 1998. ISSN 0029-5515. doi: 10.1088/0029-5515/38/7/308. URL <http://stacks.iop.org/0029-5515/38/i=7/a=308>.

- M. A. Firestone. Analysis of Modern Optimal Control Theory Applied to Plasma Position and Current Control in TFTR. *IEEE Transactions on Plasma Science*, 10(2):105–115, 1982. doi: 10.1109/TPS.1982.4316148. URL <http://ieeexplore.ieee.org/stamp/stamp.jsp?arnumber=4316148>.
- J. P. Freidberg. *Ideal Magnetohydrodynamics*. 1987. ISBN 0306425122. doi: 10.1063/1.2965499.
- J. P. Goedbloed and S. Poedts. *Principles of Magnetohydrodynamics*, volume 6. 2004. ISBN 9780511616945. doi: 10.1017/CBO9780511616945. URL http://books.google.co.uk/books/about/Principles_of_Magnetohydrodynamics.html?id=FvM6rMJob-cC&pgis=1{%}5Cnhttp://ebooks.cambridge.org/ref/id/CBO9780511616945.
- J. R. Gossner, P. Vyas, B. Kouvaritakis, and A. W. Morris. Application of cautious stable predictive control to vertical positioning in COMPASS-D tokamak. *IEEE Transactions on Control Systems Technology*, 7(5):580–587, 1999. ISSN 10636536. doi: 10.1109/87.784421.
- F. Hofmann. FBT - a free-boundary tokamak equilibrium code for highly elongated and shaped plasmas. *Computer Physics Communications*, 48(2):207–221, 1988. ISSN 00104655. doi: 10.1016/0010-4655(88)90041-0. URL [//www.sciencedirect.com/science/article/pii/0010465588900410](http://www.sciencedirect.com/science/article/pii/0010465588900410).
- F. Hofmann and S. C. Jardin. Plasma Shape And Position Control In Highly Elongated Tokamaks. *Nuclear Fusion*, 30:2013, 1990. ISSN 0029-5515. doi: 10.1088/0029-5515/30/10/003. URL <http://stacks.iop.org/0029-5515/30/i=10/a=003>.
- F. Hofmann and G. Tonetti. Tokamak equilibrium reconstruction using Faraday rotation measurements. *Nucl. Fusion*, 28, 1988a. ISSN 0029-5515. doi: 10.1088/0029-5515/28/10/014. URL <http://iopscience.iop.org/0029-5515/28/10/014>.
- F. Hofmann and G. Tonetti. Fast identification of plasma boundary and X-points in elongated tokamaks. *Nuclear Fusion*, 28(3):519–522, mar 1988b. ISSN 00295515. doi: 10.1088/0029-5515/28/3/015. URL <http://stacks.iop.org/0029-5515/28/i=3/a=015?key=crossref.59b80c614f2043fbd9bd234e5a94265d>.
- F. Hofmann, J. B. Lister, W. Anton, S. Barry, R. Behn, S. Bernel, G. Besson, F. Buhlmann, R. Chavan, M. Corboz, M. J. Dutch, B. P. Duval, D. Fasel, A. Favre, S. Franke, A. Heym, A. Hirt, C. Hollenstein, P. Isoz, B. Joye, X. Llobet, J. C. Magnin, B. Marletaz, P. Marmillod, Y. Martin, J. M. Mayor, J. M. Moret, C. Nieswand, P. J. Paris, A. Perez, Z. A. Pietrzyk, R. A. Pitts, A. Pochelon, R. Rage, O. Sauter, G. Tonetti, M. Q. Tran, F. Troyon, D. J. Ward, and H. Weisen. Creation and control of variably shaped plasmas in {TCV}. *Plasma Physics and Controlled Fusion*, 36(12B):B277, 1994. ISSN 0741-3335. doi: 10.1088/0741-3335/36/12b/023. URL <http://stacks.iop.org/0741-3335/36/i=12B/a=023>.
- F. Hofmann, M. J. Dutch, and J. M. Moret. Plasma Shape Control in TCV using MGAMS. In *22rd EPS Conference*, number vol. 19C, pages II–101, Bournemouth, 1995.

Bibliography

- F. Hofmann, O. Sauter, H. Reimerdes, I. Furno, and A. Pochelon. Experimental and Theoretical Stability Limits of Highly Elongated Tokamak Plasmas. *Physical Review Letters*, 81(14): 2918–2921, 1998. ISSN 0031-9007. doi: 10.1103/PhysRevLett.81.2918. URL <http://link.aps.org/doi/10.1103/PhysRevLett.81.2918>.
- D. A. Humphreys and I. H. Hutchinson. Axisymmetric magnetic control design in tokamaks using perturbed equilibrium plasma response modeling. *Fusion Technology*, 23:167–184, 1993. ISSN 07481896. URL http://www.osti.gov/energycitations/product.biblio.jsp?osti_id=6233755.
- S. C. Jardin and D. A. Larrabee. Feedback stabilization of rigid axisymmetric modes in tokamaks. *Nuclear Fusion*, 22:1095, 1982. URL <http://stacks.iop.org/0029-5515/22/i=8/a=011>.
- A. Kallenbach, M. Bernert, R. Dux, L. Casali, T. Eich, L. Giannone, A. Herrmann, R. McDermott, A. Mlynek, H. W. Müller, F. Reimold, J. Schweinzer, M. Sertoli, G. Tardini, W. Treutler, E. Viezzer, R. Wenninger, and M. Wischmeier. Impurity seeding for tokamak power exhaust: from present devices via ITER to DEMO. *Plasma Physics and Controlled Fusion*, 55(12):124041, 2013. ISSN 0741-3335. doi: 10.1088/0741-3335/55/12/124041. URL <http://iopscience.iop.org/0741-3335/55/12/124041/article/>.
- A. Kirk, B. Koch, R. Scannell, H. R. Wilson, G. Counsell, J. Dowling, A. Herrmann, R. Martin, and M. Walsh. Evolution of filament structures during edge-localized modes in the MAST tokamak. *Physical Review Letters*, 96(18), 2006. ISSN 00319007. doi: 10.1103/PhysRevLett.96.185001. URL <http://link.aps.org/doi/10.1103/PhysRevLett.96.185001>.
- E. Kolemen, S. L. Allen, B. D. Bray, M. E. Fenstermacher, D. A. Humphreys, A. W. Hyatt, C. J. Lasnier, A. W. Leonard, M. A. Makowski, A. G. McLean, R. Maingi, R. Nazikian, T. W. Petrie, V. A. Soukhanovskii, and E. A. Unterberg. Heat flux management via advanced magnetic divertor configurations and divertor detachment. *Journal of Nuclear Materials*, 463:1186–1190, 2015. ISSN 00223115. doi: 10.1016/j.jnucmat.2014.11.099. URL <http://dx.doi.org/10.1016/j.jnucmat.2014.11.099>.
- M. Kotschenreuther, P. M. Valanju, S. M. Mahajan, and J. C. Wiley. On heat loading, novel divertors, and fusion reactors. *Physics of Plasmas*, 14(7), 2007. ISSN 1070664X. doi: 10.1063/1.2739422. URL <http://dx.doi.org/10.1063/1.2739422>.
- A. S. Kukushkin, H. D. Pacher, V. Kotov, D. Reiter, D. Coster, and G. W. Pacher. Effect of neutral transport on ITER divertor performance. *Nuclear Fusion*, 45(7):608–616, 2005. ISSN 0029-5515. doi: 10.1088/0029-5515/45/7/008. URL <http://stacks.iop.org/0029-5515/45/i=7/a=008?key=crossref.acf4e3fbadb57d6d36567326d98e7bea>.
- L. L. Lao, H. St. John, R. D. Stambaugh, A. G. Kellman, and W. Pfeiffer. Reconstruction of current profile parameters and plasma shapes in tokamaks. *Nuclear Fusion*, 25(11):1611–1622, 1985. ISSN 0029-5515. doi: 10.1088/0029-5515/25/11/007. URL <http://stacks.iop.org/0029-5515/25/i=11/a=007?key=crossref.382b4e7e430c8741af0f7248e9a56c09>.

- L. L. Lao, Y. Kamada, T. Oikawa, L. R. Baylor, K. H. Burrell, V. S. Chan, M. S. Chance, M. S. Chu, J. R. Ferron, T. Fukuda, T. Hatae, A. Isayama, G.J. Jackson, A.W. Leonard, M. A. Makowski, J. Manickam, M. Murakami, M. Okabayashi, T. H. Osborne, P. B. Snyder, E. J. Strait, S. Takeji, T. Takizuka, T. S. Taylor, A. D. Turnbull, K. Tsuchiya, and M. R. Wade. Dependence of edge stability on plasma shape and local pressure gradients in the DIII-D and JT-60U tokamaks. *Nuclear Fusion*, 41(3):295–300, 2001. ISSN 00295515. doi: 10.1088/0029-5515/41/3/306. URL <http://stacks.iop.org/0029-5515/41/i=3/a=306>.
- E. A. Lazarus, J. B. Lister, and G. H. Neilson. Control of the vertical instability in tokamaks CONTROL OF THE VERTICAL INSTABILITY IN TOKAMAKS. *Nuclear Fusion*, 30:111, 1990a. URL <http://stacks.iop.org/0029-5515/30/i=1/a=010>.
- E.a A. Lazarus, J. B. Lister, and G. H. Neilson. Control of the Vertical Instability in Tokamak. *Nf*, 1(30):111, 1990b. ISSN 1009-0630. doi: 10.1088/1009-0630/11/3/03. URL <http://stacks.iop.org/1009-0630/11/i=3/a=03>.
- H. B. Le, F. Felici, J. I. Paley, B. P. Duval, J. M. Moret, S. Coda, O. Sauter, D. Fasel, and P. Marmillod. Distributed digital real-time control system for TCV tokamak. *Fusion Engineering and Design*, 89(3):155–164, 2014. ISSN 09203796. doi: 10.1016/j.fusengdes.2013.11.001. URL <http://www.sciencedirect.com/science/article/pii/S0920379613006996>.
- M. Lennholm, D. Campbell, F. Milani, S. Puppini, F. Sartori, and B. Tubbing. Plasma vertical stabilisation at JET using adaptive gain adjustment. In *Symposium on Fusion Engineering*, volume 1, 1998.
- A. W. Leonard, R. J. Groebner, T. H. Osborne, and P. B. Snyder. Influence of global beta, shape, and rotation on the H-mode pedestal structure in DIII-D. *Physics of Plasmas*, 15(5), 2008. ISSN 1070664X. doi: 10.1063/1.2894214. URL <http://dx.doi.org/10.1063/1.2894214>.
- A. N. Martynov, J. P. Graves, and O. Sauter. The stability of the ideal internal kink mode in realistic tokamak geometry. *Plasma Physics and Controlled Fusion*, 47(10):1743–1762, 2005. ISSN 0741-3335. doi: 10.1088/0741-3335/47/10/009. URL <http://stacks.iop.org/0741-3335/47/i=10/a=009?key=crossref.ec75ac820a25668fa3c13d0c72398d52>.
- J. M. Moret, S. Franke, H. Weisen, M. Anton, R. Behn, B. Duval, F. Hofmann, B. Joye, Y. Martin, C. Nieswand, Z. Pietrzyk, and W. van Toledo. Influence of Plasma Shape on Transport in the TCV Tokamak. *Physical Review Letters*, 79(11):2057–2060, 1997. ISSN 0031-9007. doi: 10.1103/PhysRevLett.79.2057. URL <http://link.aps.org/doi/10.1103/PhysRevLett.79.2057>.
- J. M. Moret, F. Buhlmann, D. Fasel, F. Hofmann, and G. Tonetti. Magnetic measurements on the TCV Tokamak. *Citation: Review of Scientific Instruments Tokamak Advanced Research Rev. Sci. Instrum. Rev. Sci. Instrum*, 69(70):2333–10, 1998. ISSN 0034-6748, 1089-7623. doi: 10.1063/1.1149281. URL <http://dx.doi.org/10.1063/1.1148940>{%}5Cn<http://scitation.aip.org/content/aip/journal/rsi/69/6?ver=pdfcov>.

Bibliography

- J. M. Moret, B. P. Duval, H. B. Le, S. Coda, F. Felici, and H. Reimerdes. Tokamak equilibrium reconstruction code LIUQE and its real time implementation. *Fusion Engineering and Design*, 91:1–15, 2015. ISSN 09203796. doi: 10.1016/j.fusengdes.2014.09.019. URL [//www.sciencedirect.com/science/article/pii/S0920379614005973](http://www.sciencedirect.com/science/article/pii/S0920379614005973).
- S. Moriyama, K. Nakamura, Y. Nakamura, and S. Itoh. Analysis of Optimal Feedback Control of Vertical Plasma Position in a Tokamak System. *Japanese Journal of Applied Physics*, 24(7): 849–855, 1985.
- G. H. H. Neilson, G. Federici, J. Li, D. Maisonnier, and R. Wolf. Summary of the International Workshop on Magnetic Fusion Energy (MFE) Roadmapping in the ITER Era; 7–10 September 2011, Princeton, NJ, USA. *Nuclear Fusion*, 52(4):047001, 2012. ISSN 0029-5515. doi: 10.1088/0029-5515/52/4/047001. URL <http://stacks.iop.org/0029-5515/52/i=4/a=047001?key=crossref.b606128ba1453c9ad55f5b1acb347b09>.
- J. I. Paley, S. Coda, and the TCV Team. Real time control of the plasma current and elongation in tokamaks using ECRH actuators. *Plasma Physics and Controlled Fusion*, 49(10):1735–1746, 2007. ISSN 0741-3335. doi: 10.1088/0741-3335/49/10/010. URL <http://stacks.iop.org/0741-3335/49/i=10/a=010>.
- J. I. Paley, S. Coda, B. Duval, F. Felici, and J. M. Moret. Architecture and commissioning of the TCV distributed feedback control system. In *Conference Record - 2010 17th IEEE-NPSS Real Time Conference, RT10*, 2010. ISBN 9781424471096. doi: 10.1109/RTC.2010.5750487.
- T. W. Petrie, R. Maingi, and S. L. Allen. Partially detached radiative divertor with active divertor pumping. *Nuclear Fusion*, 37(5):643, 1997. ISSN 0029-5515. doi: 10.1088/0029-5515/37/5/I07. URL <http://iopscience.iop.org/0029-5515/37/5/I07>.
- F. Piras, S. Coda, I. Furno, J-M M. Moret, R. A. Pitts, O. Sauter, B. Tal, G. Turri, A. Bencze, B. P. Duval, F. Felici, A. Pochelon, and C. Zucca. Snowflake divertor plasmas on TCV. *Plasma Physics and Controlled Fusion*, 51(5):055009, 2009. ISSN 0741-3335. doi: 10.1088/0741-3335/51/5/055009. URL <http://stacks.iop.org/0741-3335/51/i=5/a=055009?key=crossref.a281e046d21242eba91cedfc60587859>.
- F. Piras, J. M. Moret, and J. X. Rossel. Measurement of the magnetic field errors on TCV. *Fusion Engineering and Design*, 85(5):739–744, 2010. ISSN 09203796. doi: 10.1016/j.fusengdes.2010.04.049. URL <http://www.sciencedirect.com/science/article/pii/S0920379610001900>.
- R. A. Pitts, A. Kukushkin, A. Loarte, A. Martin, M. Merola, C. E. Kessel, V. Komarov, and M. Shimada. Status and physics basis of the ITER divertor. *Physica Scripta*, T138: 014001, 2009. ISSN 0031-8949. doi: 10.1088/0031-8949/2009/T138/014001. URL <http://stacks.iop.org/1402-4896/2009/i=T138/a=014001>.
- A. Pochelon, T. P. P. Goodman, M. Henderson, C. Angioni, R. Behn, S. Coda, J. M. Mayor, J. Mlynar, C. Nieswand, P. J. J. Paris, A. Perez, R. A. A. Pitts, F. Hofmann, J.-P. Hogge, N. Kirneva, A. A. Martynov, J. M. Moret, Z. A. Pietrzyk, F. Porcelli, H. Reimerdes, J. Rommers, E. Rossi,

- O. Sauter, M. Q. Tran, H. Weisen, S. Alberti, S. Barry, P. Blanchard, P. Bosshard, R. Chavan, B. P. Duval, Y. V. Esipchuck, D. Fasel, A. Favre, S. Franke, I. Furno, P. Gorgerat, P. F. Isoz, B. Joye, J. B. Lister, X. Llobet, J. C. Magnin, P. Mandrin, A. Manini, B. Marlétaz, P. Marmillod, Y. Martin, J. M. Mayor, J. Mlynar, C. Nieswand, P. J. J. Paris, A. Perez, R. A. A. Pitts, K. A. Razumova, A. Refke, E. Scavino, A. Sushkov, G. Tonetti, F. Troyon, W. V. Toledo, and P. Vyas. Energy confinement and MHD activity in shaped TCV plasmas with localized electron cyclotron heating. *Nuclear Fusion*, 39(11Y):1807–1818, nov 1999. ISSN 0029-5515. doi: 10.1088/0029-5515/39/11Y/321. URL <http://stacks.iop.org/0029-5515/39/i=11Y/a=321?key=crossref.5e7d6e5badb2bd58a36c0b6226eb444b>.
- R. Prater. Heating and current drive by electron cyclotron waves. In *Physics of Plasmas*, volume 11, pages 2349–2376, 2004. ISBN 1070-664X. doi: 10.1063/1.1690762. URL <http://dx.doi.org/10.1063/1.1690762>.
- H. Reimerdes, A. Pochelon, O. Sauter, T. P. Goodman, M. A. Henderson, and A. Martynov. Effect of triangular and elongated plasma shape on the sawtooth stability. *Plasma Physics and Controlled Fusion*, 42(6):629, 2000. ISSN 0741-3335. doi: 10.1088/0741-3335/42/6/302. URL <http://iopscience.iop.org/0741-3335/42/6/302/pdf/0741-3335/42/6/302.pdf>.
- H. Reimerdes, J. Harrison, P. Innocente, B. Lipschultz, M. Spolare, C. Theiler, and C. Tsui. TCV Experiments towards the Development of a Plasma Exhaust Solution. In *26th IAEA Fusion Energy Conference - IAEA CN-234 Contribution*, pages 1–8, 2016. URL <https://conferences.iaea.org/indico/event/98/session/36/contribution/908.pdf>.
- M. Rieth, S. L. Dudarev, S. M. Gonzalez De Vicente, J. Aktaa, T. Ahlgren, S. Antusch, D. E. J. Armstrong, M. Balden, N. Baluc, M. F. Barthe, W. W. Basuki, M. Battabyal, C. S. Becquart, D. Blagoeva, H. Boldyryeva, J. Brinkmann, M. Celino, L. Ciupinski, J. B. Correia, A. De Backer, C. Domain, E. Gaganidze, C. Garca-Rosales, J. Gibson, M. R. Gilbert, S. Giusepponi, B. Gludovatz, H. Greuner, K. Heinola, T. Hesch, A. Hoffmann, N. Holstein, F. Koch, W. Krauss, H. Li, S. Lindig, J. Linke, Ch Linsmeier, P. Lopez-Ruiz, H. Maier, J. Matejicek, T. P. Mishra, M. Muhammed, A. Muoz, M. Muzyk, K. Nordlund, D. Nguyen-Manh, J. Opschoor, N. Ordás, T. Palacios, G. Pintsuk, R. Pippan, J. Reiser, J. Riesch, S. G. Roberts, L. Romaner, M. Rosinski, M. Sanchez, W. Schulmeyer, H. Traxler, A. Ureña, J. G. Van Der Laan, L. Veleva, S. Wahlberg, M. Walter, T. Weber, T. Weitkamp, S. Wurster, M. A. Yar, J. H. You, and A. Zivelonghi. Recent progress in research on tungsten materials for nuclear fusion applications in Europe, 2013. ISSN 00223115. URL <http://www.sciencedirect.com/science/article/pii/S0022311512004278>.
- D. D. Ryutov. Geometrical properties of a "snowflake" divertor. *Physics of Plasmas*, 14(6), 2007. ISSN 1070664X. doi: 10.1063/1.2738399. URL <http://dx.doi.org/10.1063/1.2738399>.
- D. D. Ryutov, R. H. Cohen, T. D. Rognlien, and M. V. Umansky. The magnetic field structure of a

Bibliography

- snowflake divertor. *Physics of Plasmas*, 15(9), 2008. ISSN 1070664X. doi: 10.1063/1.2967900. URL <http://dx.doi.org/10.1063/1.2967900>.
- F. Sartori, A. Cenedese, and F. Milani. JET real-time object-oriented code for plasma boundary reconstruction. *Fusion Engineering and Design*, 66-68:735–739, 2003. ISSN 09203796. doi: 10.1016/S0920-3796(03)00290-4.
- O. Sauter, R. J. La Haye, Z. Chang, D. A. Gates, Y. Kamada, H. Zohm, A. Bondeson, D. Bouchers, J. D. Callen, M. S. Chu, T. A. Gianakon, O. Gruber, R. W. Harvey, C. C. Hegna, L. L. Lao, D. A. Monticello, F. Perkins, A. Pletzer, A. H. Reiman, M. Rosenbluth, E. J. Strait, T. S. Taylor, A. D. Turnbull, F. Waelbroeck, J. C. Wesley, H. R. Wilson, and R. Yoshino. Beta limits in long-pulse tokamak discharges. *Physics of Plasmas*, 4(5):1654–1664, 1997. ISSN 1070664X. doi: 10.1063/1.872270.
- O Sauter, E Westerhof, M L Mayoral, B Alper, P a Belo, R J Buttery, a Gondhalekar, T Hellsten, T C Hender, D F Howell, T Johnson, P Lamalle, M J Mantsinen, F Milani, M F F Nave, F Nguyen, a L Pecquet, S D Pinches, S Podda, and J Rapp. Control of neoclassical tearing modes by sawtooth control. *Physical review letters*, 88(10):105001, 2002. ISSN 0031-9007. doi: 10.1103/PhysRevLett.88.105001.
- S. Skogestad and I. Postlethwaite. *Multivariable feedback control: analysis and design*. 2005. ISBN 9780470011676.
- V. A. Soukhanovskii, R. E. Bell, A. Diallo, S. Gerhardt, S. Kaye, E. Kolemen, B. P. Leblanc, A. G. McLean, J. E. Menard, S. F. Paul, M. Podesta, R. Raman, T. D. Rognlien, A. L. Roquemore, D. D. Ryutov, F. Scotti, M. V. Umansky, D. Battaglia, M. G. Bell, D. A. Gates, R. Kaita, R. Maingi, D. Mueller, and S. A. Sabbagh. Snowflake divertor configuration studies in National Spherical Torus Experiment. *Physics of Plasmas*, 19(8), 2012. ISSN 1070664X. doi: 10.1063/1.4737117. URL <http://dx.doi.org/10.1063/1.4737117>.
- V. A. Soukhanovskii, S. L. Allen, M. E. Fenstermacher, D. N. Hill, C. J. Lasnier, M. A. Makowski, A. G. Mclean, W. H. Meyer, E. Kolemen, R. J. Groebner, A. W. Hyatt, A. W. Leonard, T. H. Osborne, and T. W. Petrie. Radiative snowflake divertor studies in DIII-D. *Journal of Nuclear Materials*, 463:1191–1195, 2015. ISSN 00223115. doi: 10.1016/j.jnucmat.2014.12.052. URL <http://www.sciencedirect.com/science/article/pii/S0022311514009945>.
- W. Suttrop, T. Eich, J. C. Fuchs, S. Günter, A. Janzer, A. Herrmann, A. Kallenbach, P. T. Lang, T. Lunt, M. Maraschek, R. M. McDermott, A. Mlynek, T. Pütterich, M. Rott, T. Vierle, E. Wolfrum, Q. Yu, I. Zammuto, and H. Zohm. First observation of edge localized modes mitigation with resonant and nonresonant magnetic perturbations in ASDEX upgrade. *Physical Review Letters*, 106(22), 2011. ISSN 00319007. doi: 10.1103/PhysRevLett.106.225004. URL <http://link.aps.org/doi/10.1103/PhysRevLett.106.225004>.
- H. Takahashi, E. D. Fredrickson, and M. J. Schaffer. Scrape-off-layer current model for filament structure observed during edge-localized modes in the DIII-D tokamak. *Physical Review*

- Letters*, 100(20), 2008. ISSN 00319007. doi: 10.1103/PhysRevLett.100.205001. URL <http://link.aps.org/doi/10.1103/PhysRevLett.100.205001>.
- C. Theiler, B. Lipschultz, J. Harrison, B. Labit, H. Reimerdes, C. Tsui, J. A. Boedo, B. P. Duval, S. Elmore, P. Innocente, U. Kruezi, T. Lunt, R. Maurizio, F. Nespoli, U. Sheikh, K. Verhaegh, and N. Vianello. Results from recent detachment experiments in alternative divertor configurations on TCV. *Nuclear Fusion*, pages Submitted 1–15, 2017.
- F. Troyon, R. Gruber, H. Saurenmann, S. Semenzato, and S. Succi. MHD-Limits to Plasma Confinement. *Plasma Physics and Controlled Fusion*, 26(1A):209–215, 1984. ISSN 0741-3335. doi: 10.1088/0741-3335/26/1A/319. URL <http://stacks.iop.org/0741-3335/26/i=1A/a=319?key=crossref.cae719754c2ff814c52af095f5977ea4>.
- M. V. Umansky, T. D. Rognlien, D. D. Ryutov, and P. B. Snyder. Edge plasma in snowflake divertor. *Contributions to Plasma Physics*, 50(3-5):350–355, 2010. ISSN 08631042. doi: 10.1002/ctpp.201010057.
- P. M. Valanju, M. Kotschenreuther, S. M. Mahajan, and J. Canik. Super-X divertors and high power density fusion devices. In *Physics of Plasmas*, volume 16, 2009. ISBN 1070-664X. doi: 10.1063/1.3110984. URL <http://dx.doi.org/10.1063/1.3110984>.
- M. L. Walker, D. A. Humphreys, J. A. Leuer, and J. R. Ferron. Development of Multivariable Control Techniques for Use with the DIII-D Plasma Control System. Technical Report GA-A23151, San Diego (CA), 1999.
- D. J. Ward and F. Hofmann. Active feedback stabilization of axisymmetric modes in highly elongated tokamak plasmas. *Nuclear Fusion*, 34(3):401, 1994. ISSN 0029-5515. doi: 10.1088/0029-5515/34/3/I08. URL <http://iopscience.iop.org/article/10.1088/0029-5515/34/3/I08/pdf>.
- A. Wingen, T. E. Evans, C. J. Lasnier, and K. H. Spatschek. Numerical modeling of edge-localized-mode filaments on divertor plates based on thermoelectric currents. *Physical Review Letters*, 104(17), 2010. ISSN 00319007. doi: 10.1103/PhysRevLett.104.175001.
- L. J. Zheng, H. Takahashi, and E. D. Fredrickson. Edge-localized modes explained as the amplification of scrape-off-layer current coupling. *Physical Review Letters*, 100(11), 2008. ISSN 00319007. doi: 10.1103/PhysRevLett.100.115001. URL <http://link.aps.org/doi/10.1103/PhysRevLett.100.115001>.
- H. Zohm. Edge localized modes (ELMs). *Plasma Physics and Controlled Fusion*, 38(2):105–128, 1996. ISSN 0741-3335. doi: 10.1088/0741-3335/38/2/001. URL <http://stacks.iop.org/0741-3335/38/i=2/a=001>.
- H. Zohm, C. Angioni, E. Fable, G. Federici, G. Gantenbein, T. Hartmann, K. Lackner, E. Poli, L. Porte, O. Sauter, G. Tardini, D. Ward, and M. Wischmeier. On the physics guidelines for a tokamak DEMO. *Nuclear Fusion*, 53(7):073019, 2013. ISSN 0029-5515. doi: 10.

Bibliography

1088/0029-5515/53/7/073019. URL <http://stacks.iop.org/0029-5515/53/i=7/a=073019?key=crossref.d677fdddde2bd2d5b912411cf42615a6>.

Acknowledgements

The final and the most important step of a thesis is reached when it comes to the acknowledgements. Although I am glad that it is all over now, I have to say that the last five years was the most enjoyable time I ever had and it is my pleasure to thank the many people who contributed to the quality of the work and of my time at SPC.

The long list of people commences with Dr. Stefano Coda who supervised my work. His advice and enthusiasm guided me through the thesis and boosted my motivation when it was in the danger of decline. I have always appreciated the warm welcome I received every time I called into his office with questions. Independent of the time of the day and his own workload, he never turned down a question and took the time to explain and introduce me into the complexity of the tokamak operations. During the work I have benefited from many discussions with him and gained a sense of aptitude for solving and approaching physics problems. I am grateful that you let me a lot of freedom and responsibility in my work but also paid attention that I stayed on track. Although you have great responsibility and a large of amount of work at SPC you were always there when I needed advice. I was, and will always be impressed by your broad and deep knowledge in the field and your passion for your work. Thank you for being so patient, and helping me improve! Supervisors like you are hard to find, and I'm eternally grateful that you were my supervisor. Your guidance and support has been amazing! Thank you for helping me improve.

I cannot stress enough my sincere gratitude to Dr. Federico Felici who was my unofficial co-supervisor. His constant help and support really guided me during the Ph.D. His collaboration and support has made invaluable contribution to my project. Most of the fundamental ideas with respect to the project have emerged from his brilliant mind. His constant supervision, involvement and views have made a tremendous contribution to my work. He has been there for me during the entire length of project and helped me to learn control theory and Matlab. I had so much fun learning with you. The email exchanges and discussions were very insightful and interactive, so thank you. You have been a great teacher.

A big thank you to Dr. Cristian Galperti for all his help and support for the digital control system. His passion and dedication toward his work is truly outstanding. He has played an instrumental role in my project. The long and interesting discussion have improved the quality of my project. His attitude of sharing knowledge and aptitude of having open discussion have

Acknowledgements

truly helped me in progressing and formulating my work. The project would have been incomplete without your collaboration.

I would also like to thank Dr. Jean-Marc Moret for all his help and support with respect to my project and with RTLIUQE. Thank you for giving me the time for discussing my project and helping me find various solutions for my problems.

A big thanks to Dr. Holger Reimerdes and Dr. Benoit Labit for helping me to understand the fundamentals of the snowflake plasma configuration. I am also grateful to Dr. Laurie Porte, Dr. Jonathan Graves, Dr. Basil Duval, Dr. Joan Decker, Dr. Tim Goodman. and Dr. Olivier Sauter, although they have not been directly involved in my project but they all motivated and guided me in my tough times.

Thanks to Edith and Roxane for the help with administrative stuff, and in particular thanks to Thushi for always kindly reminding me, every month, that I had forgotten to do the time sheets.

My old office mates Josef, Gustavo and Falk helped me a lot during the start of my Ph.D., they all provided me with a lot of help whenever I had any problems. I am also grateful to my current office mates Jeremy, Dahye, Zhouji, Matteo, Hugo, Rogerio and Roberto. Thank you guys and gal, you all have been awesome and I would definitely miss the Wednesday apero which seemed to happen almost everyday. I would also like to thank Joyeeta, Federico, Samuel, Claudio, Emmanuel, Stephane and Gabreili. Thanks to the whole group of Ph.Ds and Post doc (especially Antoine and Umar) at SPC; you made the lab life so much easier and we had so much fun together! I'm glad that I could find so many good friends among you.

The acknowledgement would not be complete without mentioning my parents who supported me throughout the countless years of school and university. I have always been very grateful for their encouragement, although it often meant to be far away from home. Thanks a lot.

Lastly, I would like to thank Isha my girlfriend/wife, she has been my rock during the hard times, thank you for taking care of me. I owe and dedicate my Ph.D. to you.

Lausanne, 20 April 2017

H. A.

Himank ANAND

PERSONAL DATA

PLACE AND DATE OF BIRTH: India | 04 May 1987
CURRENT ADDRESS: Chemin de Fontadel 31, Prilly-1008, Switzerland
PHONE: +41 789 493 184
EMAIL: himank.anand@epfl.ch or himank_anand@yahoo.co.in

WORK EXPERIENCE

<i>Current</i>	PhD student, SWISS PLASMA CENTER, ÉCOLE POLYTECHNIQUE FÉDÉRALE DE LAUSANNE, Switzerland.
APRIL 2012	<i>“Exploration of candidate fusion reactor regimes by real time control of tokamak plasma shape control”</i> Development of real time plasma shape and position controller using real time equilibrium reconstruction code for advanced plasma configurations.
APRIL 2010	Master thesis at EUROPEAN ORGANIZATION FOR NUCLEAR RESEARCH, Switzerland. <i>“Study of TGEMs and RETGEMs detectors for ALICE upgrade”</i> Development and characterization of TGEMs and RETGEMs detectors for ALICE upgrade

EDUCATION

AUGUST 2011 | Master in NUCLEAR SCIENCE, **University of Delhi**, India.
AUGUST 2010 | Master in NUCLEAR PLANT DESIGN, **ENSTA ParisTech**, France.
AUGUST 2008 | Bachelors in PHYSICS, **St. Stephen’s College**, India.

CONFERENCES AND TALKS

EPS 2013	“Development of plasma shape control using real-time equilibrium reconstruction on TCV” (Poster).
EPS 2014	“First experimental results of plasma shape control using real time equilibrium reconstruction in TCV” (Poster).
APS 2015	“Plasma shape and position controller design for advanced plasma configurations in TCV” (Poster).
IAEA 2016	“Distributed digital real-time control system for the TCV tokamak and its applications” (Poster).
TALK 2015	“Plasma shape and position controller design for advanced plasma configurations in TCV”, at Princeton Plasma Physics Laboratory and General Atomics, USA.

PAPERS AS FIRST AUTHOR

- 2016 | “Distributed digital real-time control system for the TCV tokamak and its applications”, (2016) , accepted in *Nuclear fusion*.
- 2016 | “A novel plasma position and shape controller for advanced configuration development on the TCV tokamak”, (2016) , submitted in *Nuclear fusion*.
- 2016 | “Distributed digital real-time control system for the TCV tokamak and its applications”, IAEA. Conf. Abstr. (2016), EX/P8-32.
- 2015 | “Plasma shape and position controller design for advanced plasma configurations in TCV”, APS. Conf. Abstr. **60** (2015), GP-12.00140.
- 2014 | “First experimental results of plasma shape control using real time equilibrium reconstruction in TCV”, Europhys. Conf. Abstr. **38F** (2014), (P-5.069).
- 2013 | “Development of plasma shape control using real-time equilibrium reconstruction on TCV”, Europhys. Conf. Abstr. **37D** (2013), (P-2.157).

AWARDS

- JUNE 2014 | Poster prize, 41st European Physical Society Conference on plasma physics.
- AUGUST 2011 | First position in Masters in Nuclear Science.
- AUGUST 2010 | First position in Masters in Nuclear Plant Design.

